AN ULTRASONIC METHOD FOR AIRCRAFT WAKE VORTEX DETECTION

by

Rebecca J. Rodenhiser

A Thesis

Submitted to the Faculty

of the

WORCESTER POLYTECHNIC INSTITUTE

In partial fulfillment of the requirements for the

Degree of Master of Science

in

Mechanical Engineering

August 30th, 2005

Approved:

_____

Professor William W. Durgin, Co-Advisor

_____

Professor Hamid Johari, Co-Advisor

_____

Professor David Olinger, Thesis Committee

_____

Professor Mark Richman, Graduate Committee Representative

Abstract

This thesis documents the experimental proof of concept study for an ultrasonic method of wake vortex detection. A new acoustic technique is utilized to measure the circulation produced in the wake of lift-generating aircraft. Ultrasonic signals are transmitted in a path around the wake vortex, and are used to determine the average in-line velocity component along the acoustic path. It is shown herein that this velocity component is directly proportional to the net circulation value within the acoustic path. This is the first study to take this methodology and implement it in a realistic airport setting.

This project included constructing a prototype and conducting field tests to prove the validity of this technology in a realistic environment setting. During field tests an acoustic path enclosed the vorticity shed behind one wing of a Piper PA-28 aircraft. Fourteen initial test flights were conducted in calm atmospheric conditions, and results show circulation values measured are comparable in magnitude and direction to expected circulations generated by the Piper PA-28 aircraft. Additional testing in various atmospheric conditions revealed the scope of practice for such a measurement technology. This study demonstrates the validity of the acoustic method in detecting aircraft wake vortices. Future investigations and applications utilizing this technique are discussed within.

Acknowledgements

I would like to thank my advisors, Professors William Durgin and Hamid Johari, for their tremendous guidance and support throughout this project. I would like to thank Professors David Olinger and Mark Richman for serving on this thesis committee. I would also like to thank Brad Miller and Ken Stafford for their vital assistance with field testing.

I would like to thank Tanner-Hiller airport, and specifically Airport Manager Robert Burchard. His consideration in allowing us to utilize the airfield and his patience and assistance during field testing is greatly appreciated. I would also like to thank Manchester Airport, particularly Michael Farren, Scott Malafronte, and Scott Brown, for allowing me on the airfield to collect aircraft noise data.

I would like to thank Barbara Edilberti, Barbara Fuhrman, Pam St. Louis, Nancy Hickman and Gail Hayes for their support and friendship. I would also like to thank Steve Derosier and Bill Weir for their assistance. I would like to thank my husband, Keith, for his unconditional support throughout this project.

I would like to dedicate this work to the memory of Robert Taylor. His support was instrumental in getting this project off the ground, and I am deeply saddened that he is not here today to see the accomplishments of a project to which he contributed so greatly. This project would not have been possible without his knowledge and friendship.

Table of Contents

Table of Figures

List of Tables

Nomenclature

A	Amplitude of the transmitted ultrasonic pulse
a	Speed of sound
a_p	Propagation speed of sound
I_f	Interval frequency of transmitted ultrasonic pulses
N	Number of cycles in the transmitted ultrasonic pulse
f	Frequency of ultrasonic signal
u_ℓ	Velocity in-line with path ℓ
L	Acoustic path length
P	Air density
V	Flight speed of aircraft
b’	Length of aircraft wing
γ	Adiabatic constant
R	Ideal gas constant
ω	Vorticity
t	Time
$t_{(+)}$	Time of acoustic pulse propagation in clockwise direction
$t_{(-)}$	Time of acoustic pulse propagation in counter-clockwise direction
R	Cross-correlation function
H	Hilbert transform
E	Hilbert transform envelope function
M	Mach number
Γ	Circulation

1 Introduction

Aircraft wake vortices pose a significant safety hazard for all air traffic. Vortices shed in the wake of large aircraft often contain intense velocities that can cause structural damage and even rolling of other aircraft that may encounter them. The fluid dynamic development of these flow structures is well understood as a result of numerous experimental tests and numerical simulations. The greatest hazard from wake vortices is most likely to occur in the vicinity of an airport, where aircraft share common flight paths and are in close proximity. Prediction of the exact location and velocities of wake vortices at any given time is highly desirable, yet difficult as they are affected by many factors such as atmospheric turbulence, local winds, and proximity to the ground. Previous field trials have attempted to detect wake vortices in an airport environment, with varying degrees of success.

1.1 Background on Wake Vortex

Wake vortices have been studied since the early part of the 20th century, and the basic aerodynamics of wake vortices and their development downstream of the wing has been widely published in aerodynamic textbooks (Anderson, 1984; Shevell, 1989; Fox and McDonald, 1985). All lift-generating airfoils result in a bound circulation that occurs along the cross-section of the wing, the magnitude of which can be described by the Kutta-Joukowski theorem (Anderson, 1984).

Ludwig Prandtl is credited with the first analysis of lift distribution along a finite wing and the resulting trailing vortices. The circulation around the cross section of the wing is shed in the form of a trailing vortex tube at the edge of the wing, or wing tip.

These wing tip vortices occur at both wings, and rotate in opposite directions (Anderson, 1984). These vortices were quickly observed to play a major role in induced drag and induced angle of attack of the aircraft, and understanding their development and existence is instrumental in understanding fundamentals of flight.

For rectangular, elliptical or segmented wing shapes, a vortex sheet is shed behind the entire length of the wing which rolls up into a single large vortex further downstream. Knowing the initial load placed on the wing and the geometric measurements of the aircraft, the circulation can be theoretically calculated in the tip vortex. (Anderson, 1984; Brown, 1973; Gerz and Holfzapel, 1999; Ozger et. al, 2001).

Understanding the behavior of these wake vortices is highly important given the safety threat they pose to other aircraft. Numerous observational studies and numerical simulations have been conducted to better understand the motion and decay of these vortices. If unaffected by any outside forces, the vortices are observed to induce a downward motion on each other. The pair will descend in the atmosphere as they decay due to viscous forces, until they dissipate entirely or interact with an object or are affected by some outside force (Corjon and Poinsot, 1996).

Early studies by Brown (1973) produce relationships between the maximum rotational velocities associated with the trailing wake vortex and aircraft flight speeds. Brown continues his analysis in understanding the growth of the turbulent core of these vortices, essential to the vortex decay rate. More recent experimental studies gather observational data to gain an understanding of the rate of decay of these vortices from large aircraft (Sarpkaya, 1998). Brown and Sarpkaya conclude that wake vortices do have a turbulent core and the turbulent decay of kinetic energy overwhelms any

dissipation effects from molecular diffusion, yet the exact turbulent structure of the core is not well understood.

Behavior of wake vortices is widely shown to be altered by proximity to the ground (Burnham and Hallock, 1998; Hamilton and Proctor, 2000; Corjon and Poinsot, 1996) as well as by various atmospheric conditions (Holfzapel et. al, 2000, Fresch and Zinner, 2004). A numerical simulation by Corjon and Poinsot (1996) finds that ground proximity and resulting viscous flow produce a secondary pair of vortices that induce the original wake vortices to move upward; experimental studies confirm a formation of secondary vortices as a result of proximity to the ground (Burnham and Hallcok, 1998). Proximity to the ground has also been shown in numerical simulations to produce lateral separation of the vortex pair (Hamilton and Proctor, 2000; Corjon and Poinsot, 1996).

Numerical studies have been conducted to determine the effect of the convective atmospheric boundary layer on wake vortices. The large eddy simulation study of Holfzapel et. al (2000) shows that the vertical velocity fluctuations of a classic convective boundary layer (CBL) results in deformation of the vortices, and the significant turbulence of the CBL erodes the wake vortices very rapidly. Recent studies have focused on classifying the meteorological conditions into categories, and determining the effect that each meteorological category has on the decay and transport of vortices (Frech and Zinner, 2004).

All of the above mentioned behaviors of wake vortices are summarized by the Federal Aviation Administration (FAA) in their Aeronautical Information Manual. The FAA warns pilots that wake vortices from preceding aircraft can sink in atmosphere at rates of several hundred feet per minute. They also indicate that when vortices are in

proximity to the ground with no prevailing wind, they will separate laterally with a ground speed of 2 or 3 knots. Ambient prevailing winds across a runway at the speed of 3 knots will result in the upwind vortex remaining stationary on the runway, posing a significant hazard to following aircraft (FAA AIM, 2005).

1.2 Safety Concerns of Wake Vortices

The safety concern of the wake vortex to other aircraft began in the early 1970's as very large and heavy commercial aircraft became common. Larger, heavier aircraft produce stronger vortices, and therefore are a greater hazard to following aircraft, particularly small aircraft. The National Transportation Safety Board (NTSB) cites wake vortices as the cause of over 51 accidents and incidents from 1983-1993 (Boluriaan and Morris, 2001). The NTSB database shows for the next 10 year period, from 1994-2003, that wake vortices are cited as the primary cause of 39 accidents and incidents, many of which occurred to small aircraft encountering the wake vortex of a preceding larger aircraft.

As a result, the FAA imposed mandatory minimum separation distances between aircraft to reduce the safety hazard due to wake vortices. These separation distances are based on the estimated time that a wake vortex will exist and pose a hazard to other aircraft. The FAA regulations are extremely comprehensive and are dependent upon factors such preceding and following aircraft size, shared runway or cross-runway orientation, and landing versus departure. Table 1 summarizes the basic separation interval that must be maintained between aircraft. In general, a four to six nautical mile separation must be observed for landing aircraft, and this same spacing equates to two to three minutes spacing between departing aircraft (FAA AIM, 2005). While this mandate

is an effective method of reducing the hazard posed by wake vortices, it also limits airport capacity.

Following Aircraft		Lead Aircraft		
Class	Weight (lbs)	Small	Large	Heavy
Small	< 41,000	2.5	5	6
Large	41,000 - 255,000	2.5	4	5
Heavy	> 255,000	2.5	4	4

Table 1.1 – FAA mandated separation distances, in nautical miles (nm).

An aircraft that encounters a wake vortex is subject to experience rolling, rapid, descent, or sudden changes in pitch. The aircraft's ability to compensate for the forces induced by wake vortices depends upon the aircraft's wing span and responsiveness. There is a severe risk of aircraft damage and loss of control of the aircraft, particularly for small aircraft that encounter a vortex.

1.3 Wake Vortex Detection

It is recognized that an effective method of wake vortex detection in the vicinity of airports is needed in order to aid air traffic controllers in avoiding aircraft encounters. Real-time detection of wake vortices would result in the ability to create appropriate aircraft spacing based on actual duration of these vortices, instead of using the estimated values that are currently in place. As previous research shows, wake vortex dissipation can be enhanced by a variety of factors, and circulation may reduce to harmless levels well before the mandatory separation distance has expired. Vortices can also be advected out of the flight path by local winds, leaving a safe runway available for air traffic. A 1991 study revealed that there is a significant financial impact of reducing separation distances based on simulations conducted for five major US airports (Baart et. al, 1991).

In a 2000 application of that study it is revealed that the financial implications of reducing the current separation distances by an average of 30 seconds would result in net savings of five billion US dollars annually for the airline industry (Rubin et. al, 2000).

Detection of wake vortices at airports has been attempted by numerous methods. Attempts have been made to observe actual wake vortices using radar (Shariff and Wray, 2002), Lidar (Hinton et. al, 1999), and a radio acoustic sounding system (RASS) (Boluriaan and Morris, 2001; Rubin et. al, 2000). An operational study by Rubin et. al (2000) showed a RASS utilized as a vortex sensor was able to detect wake vortices from aircraft of all sizes in real time, and during all weather conditions. However RASS technology is susceptible to ground clutter interference, and is unable to determine the vortex circulation direction.

The National Aeronautics and Space Administration (NASA) is working toward a comprehensive wake vortex detection method that incorporates local atmospheric conditions, actual circulation data, and numerical modeling to produce a wake vortex strength and location prediction tool (Hinton, 2001; O'Conner and Rutishauser, 2001; Hinton et. al, 1999). This NASA project title AVOSS – Aircraft VOrtex Spacing System – has conducted field trials at Dallas/ Fort Worth Airport. The detection portion of the AVOSS system utilizes a pulsed LIDAR system. Recent documentation indicates the LIDAR was unable to measure vortex strength and position in all weather conditions, and current research continues to focus on improving this technology (Rutishauser et. al, 2003).

Within the past few years a technology known as SOCRATES has been utilized in field studies to track and measure the presence of wake vortices. SOCRATES, an

acronym for Sensor for Optically Characterizing Remote Atmospheric Turbulence Emanating Sound, and is a technology that measures the infrasound emitted from the vortex structures in the 200-300 Hz frequency range (Flight Safety Technology, 2004). This technology has had some success in field trials, yet researchers indicate that further understanding is needed before this technology can be used practically as a real-time vortex detection system (Rudis, Wang and Daskalakis, 2001).

The present study utilizes a new acoustic method for circulation detection for use in measuring wake vortex circulations from aircraft during low pass flights over an airfield. This methodology differs significantly from all previous field trials of wake vortex detection. The goal is of this study is to use the theory developed in the following section to detect the circulation values of a wake vortex pair behind an actual aircraft. This is the first attempt to test the viability of this methodology in a realistic airport environment.

2 Theory

The theory developed for using ultrasound to make circulation measurements was first published three decades ago. The application of this methodology has grown over the past few decades with the evolution of more advanced transducer and data logging technology. This technology has been used in commercial flow meters with great success. The application of this technology to measure trailing vortices was first developed by Johari & Durgin (2000; Desabrais and Johari, 2000), who successfully measured circulation in the wake of model airfoils in a wind tunnel, and have patented the technology as a method of detecting real wake vortices in a realistic outdoor airport environment. In this chapter we examine the development of the theory for using acoustic signals to measure circulation, and discuss several environmental factors that must also be considered when applying this technique to an airport environment.

2.1 Circulation Measurements Using Ultrasound

The use of ultrasound in circulation detection was first achieved by Schmidt (1975). The technique utilizes acoustic pulses transmitted in a closed path around a vortex to measure the integral velocity component of the fluid in the direction of pulse transmission. The average velocity is calculated from time measurements of the acoustic pulses traversing both directions around the closed path. The magnitude of the difference between the propagation times of opposite traveling acoustic pulses indicates the magnitude of the vortex circulation contained within the path, and the sign indicates the direction of vortex rotation. This technique is advantageous due to the fact that it is non-invasive to the flow field, and does not require measurements of any other variables in

the flow field, including the speed of sound. Variations of this technique, including methods of detecting circulation using a straight transmission path through a vertical flow are discussed in more recent literature (Johari & Durgin, 1998).

The theory of the acoustic method of vortex detection is based upon two basic principles. The first is that the sum of all vorticity contained within an enclosed path is equal to the line integral of the velocity along the closed path. The second is that the time it takes the ultrasonic pulse to travel around a path is defined as the integral of the inverse propagation speed of sound in a fluid. These two principles can be written as equations (2.1) and (2.2) respectively.

$$\Gamma = \oint \vec{u}_l \cdot d\vec{\ell} = \int_{closed\_path} u_\ell d\ell \tag{2.1}$$

$$t = \oint \frac{1}{a_p} d\ell \tag{2.2}$$

The propagation speed of the ultrasonic pulse is the sum of the speed of sound and the velocity component along the pulse transmission path, as shown in equation (2.3).

$$a_p = a + u_\ell \tag{2.3}$$

The ultrasonic signal is transmitted in both directions along the path enclosing the circulation, and the time of this transmission is recorded. Discriminating the two directions of transmission will be done so with (+) and (-) subscripts, indicating the pulse

traveling clockwise or counter clockwise around the closed path. Combining equations (2.2) and (2.3) give us the following equations for the time of transmission:

$$t_{(+)} = \oint \frac{1}{a + u_\ell} d\ell \tag{2.4}$$

$$t_{(-)} = \oint \frac{1}{a - u_\ell} d\ell \tag{2.5}$$

$$\Delta t = t_{(-)} - t_{(+)} = \oint \left(\frac{1}{a - u_\ell} - \frac{1}{a + u_\ell} \right) d\ell \tag{2.6}$$

The difference of these signal transmission times is written above in equation 2.6, and can be simplified to:

$$\Delta t = 2 \oint \frac{u_\ell}{a^2 - u_\ell^2} d\ell \tag{2.7}$$

$$\Delta t = \frac{2}{a^2} \oint \frac{u_\ell}{1 - \left(u_\ell / a\right)^2} d\ell \tag{2.8}$$

If we are measuring circulations that contain local fluid velocities that are much less than the speed of sound, further simplifications can be made. Based on this assumption, we can make the simplification of $[1-(u_\ell/a)^2] \approx 1$, and therefore simplify equation (2.8) to:

$$\Delta t = \frac{2}{a^2} \oint u_\ell d\ell \tag{2.9}$$

By substituting equation (2.1) into equation (2.9), we get a relationship between the time difference in pulse transmission and the circulation contained within the path:

$$\Delta t = \frac{2}{a^2}\Gamma \tag{2.10}$$

Further simplification can occur by substituting the speed of sound rewritten in terms of the path length and signal transmission time, as in equation (2.11), yielding equation (2.12).

$$a = \frac{2L}{t_{(-)} + t_{(+)}} = \frac{2L}{\sum t} \tag{2.11}$$

$$\Gamma = 2(\Delta t)\left(\frac{L}{\sum t}\right)^2 \tag{2.12}$$

Equation (2.12) shows us that by measuring the time transmission of the ultrasonic signal in both directions ($t_{(-)}$,$t_{(+)}$) along a path of known length (L) we can determine the magnitude and direction of the net circulation (Γ) contained within this path. This equation is advantageous due to the fact that it accounts for fluctuations in the speed of sound that will occur over time, therefore making it unnecessary to track fluctuations in the variables that affect speed of sound such as temperature, humidity, and pressure.

2.2 Circulation Measurements Applied to Aircraft Wake Vortices

This acoustic method for measuring circulation can be applied to aircraft wake vortices by creating an acoustic path that encloses one or more of these trailing vortices. This method of flow detection has been used in prior studies of wake circulation measurements in wind tunnel experiments. It has been found to accurately detect the circulation in the wake of a NACA 0012 airfoil, when compared to theoretical circulation values determined by the Kutta-Joukowski theorem (Desabrais, 1997; Desabrais and Johari, 2000).

This ultrasonic method has been patented in the US, patent #6062076, by Johari and Durgin (Johari and Durgin, 2000). This patent outlines the application of this technique for wake vortex detection at an airport, and shows examples of expected data values gathered from this technique. A variety of acoustic paths are discussed, each with expected data results. In addition this patent introduces the idea of instituting a no-slip condition for the path length along the ground, which assumes the velocity along this path length is zero. This allows the signal transmission to occur over a shorter distance, yet still utilize the closed path acoustic signal transmission theory.

One example of apparatus setup from the patent is shown below. Figure 2.1 depicts the setup of aircraft measurement equipment at an airport. With an aircraft taking off through the acoustic path, its trailing wake vortices will originate within the path.

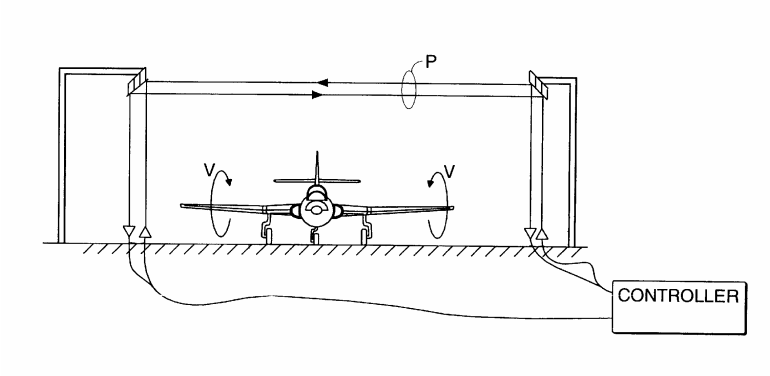

Figure 2.1 – Aircraft circulation measurement apparatus from Johari & Durgin patent

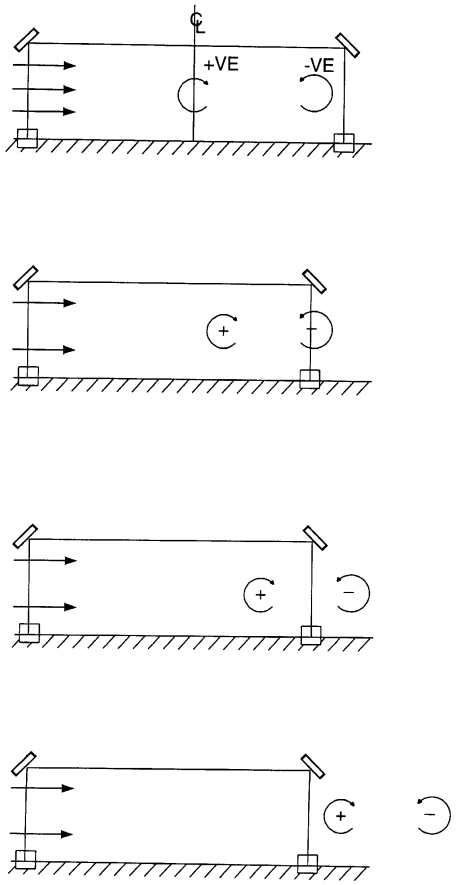

Figure 2.2 – Four step scenario of vortex pair on runway with a cross wind

Figure 2.2 shows a four step scenario depicting a wake vortex pair shed on a runway. In this scenario there is a slight cross breeze on the runway blowing the vortex pair off the runway. In the first image, the vortices are both of approximately equal strength and are both within the ultrasonic signal path, and therefore the net circulation is expected to be zero. As the vortex pair is blown by the wind, one vortex will be blown out of the measured area while one is still within the measured area, as shown in the third image. At this point, the measurement system should see a high degree of circulation contained within the sample area until that second vortex is also blown out of the area, depicted in the last frame.

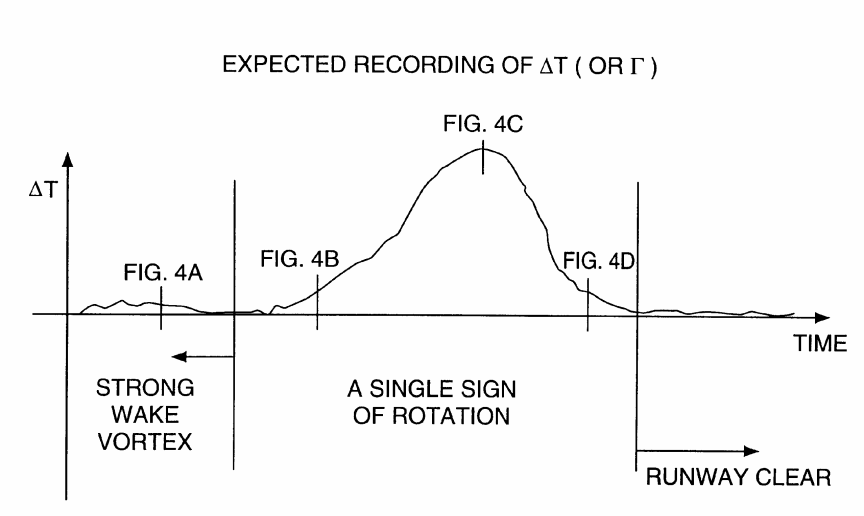

Figure 2.3 – Values of circulation expected from Figure 2.2 scenario

Figure 2.3 shows the expected circulation data gathered during such a scenario. The initial circulation contained within the sample area would be zero, and then a peak would occur when one vortex of the pair had moved outside the sample area. Once the second vortex had moved off the runway, the circulation values would be nil again.

2.3 Acoustic Measurement Technique Applied to Outdoor Experiments

Utilizing this theory in an outdoor setting requires some assumptions to be made regarding ultrasonic signal transmission in the atmosphere. First, we are assuming that atmospheric variables (such as temperature, humidity, pressure, ambient winds, and turbulence) remain constant during the short time it takes to complete signal transmission in opposite directions around the path. It is an important distinction that these variables do not have to be constant along the path, but must remain relatively steady at any given location over the course of approximately one second it takes to transmit the pulse in opposite directions.

Acoustic signals propagating through a fluid become attenuated by that fluid, and the amount of attenuations per unit length of transmission is a function of humidity, temperature, and pressure of the fluid, and frequency of the acoustic signal. Calculations of atmospheric attenuation of the sound signal must be performed to ensure that signal is detectable above ambient noise at the end of the transmission path. Therefore, we must also understand the ambient noise levels in the atmosphere at an airport. Significant research has been conducted on ambient airport noise in the audible frequency spectrum, due to concerns over the past few decades of noise pollution in the vicinity of airports. However, there is no known data as to the ambient noise at airports in the ultrasonic frequency range (20 – 100 kHz).

In addition, an ambient circulation value may exist, the strength of which is dependent upon air movement, either by winds or convective currents. The sensitivity of the system in detecting small circulations will be limited by the ambient circulation during any given day of measurements. Very little natural fluctuations of circulation are

expected with extremely low wind shear and convection. However, in windy or gusty conditions or afternoons with an abundance of solar heating and consequent convection, greater natural variations are expected.

In moving the experiment from the wind tunnel to an actual airport environment we also must ensure that all assumptions made are still valid. We assume in our theoretical development that the average local in-line fluid velocity is much less than the speed of sound ($[1-(u_\ell/a)^2] \approx 1$). If we define this further, stating the local fluid velocity must be one order of magnitude smaller than the speed of sound, we can find the limits of application of this theory. Our wake vortex contains two distinct regions, the vortex core and the vortex outer region, with the boundary between the two regions occurring at the radius of maximum rotational velocity. Vortical flows such as these are often modeled using two simplified flow regimes. The ideal vortex model can be used to approximate the flow outside the vortex core region (Panton, 1996). The flow contained inside the vortex core region is dominated by viscous forces, and can be approximated by a decreasing linear relationship between rotational velocity and radius when approaching the center of rotation.

To find the limits of application of this theory, we must adhere to a maximum average velocity in-line with acoustic transmission that does not exceed ~30 m/s (which is one order of magnitude less than the average speed of sound, 330 m/s). Experimental data gathered in a 1998 field studies measured the velocities associated with wake vortices from large aircraft (Sarpkaya, 1998). In this study, the largest velocity measured from test aircraft (DC-10 and B-757) did not exceed 20 m/s at the edge of the vortex core. It is therefore appropriate to assume that for commercial aircraft of all sizes the average

velocity along the acoustic path will remain well below 30 m/s, and the theory used in this measurement technique is valid.

This analysis also leads us to determining a Mach number for the wake vortex flow. As state above, the maximum velocity value of a wake vortex generated by a large aircraft is on the order of 20 m/s. Given an average speed of sound of 330 m/s, this yields a Mach number, $M = u/a$, of 0.06. Mach numbers significantly less than 0.3 indicate incompressible flow assumptions are valid (Panton, 1996).

3 Research Methodology

This project consists of creating the first ever full-scale prototype of the ultrasonic wake vortex detection measurement system. This prototype was comprised of multiple components to transmit and receive acoustic signals and process the data to extract the circulation values within the acoustic path. This chapter discusses the equipment used and setup configuration for this prototype, as well as signal processing methodology.

3.1 Experimental Setup

Field tests were conducted using the basic principles outlined in the Johari & Durgin patent, with the Piper Cherokee PA-28 aircraft producing the wake vortices. A triangular acoustic path was used in this study, with the goal of measuring the trailing vortex produced by one of the Cherokee's wings. This path shape differs from the one shown in Figure 2.1, yet is an alternate setup listed in the original patent. Initial trials were conducted in a calm environment, and later trials conducted in a cross-wind environment.

The rectangular path described in the Johari & Durgin patent surrounds both vortices shed from the aircraft. This path is best used when there is a cross wind present, which will blow the vortices out of the enclosed path one at a time. When this occurs, the expected measured circulation values will be the same as displayed in Figure 2.3. If there is no cross wind present, the vortices may remain within the enclosed path until they dissipate to undetectable levels, in which case no circulation value will be measured by the apparatus.

The triangular path, shown in Figure 3.1, is established by mounting one reflector atop a 30 foot tower and another reflector positioned just above ground height 80 feet away, and is chosen for the benefits it provides over the rectangular shaped path. The triangular path was easier to setup, since it requires just one tower. This configuration requires the test aircraft to pass near a single tower rather than through two towers, making it significantly safer. In addition, both vortices are not entirely contained within the closed path initially, and therefore circulation values should be detectable from the very first measurement. This is advantageous when there is little or no cross wind present, as vortices will still be detected by the system. The test plane was flown approximately 15 feet above ground and positioned such that one wingtip passed within or near the closed path, and the other remained outside the region. The goal was to capture a single vortex within the path, yielding detection of the maximum amount of circulation.

Figure 3.1 – Image of equipment setup showing direction of signal transmission

The signals originated from two transducers at the bottom of the tower, positioned to transmit the ultrasonic signal in opposite directions, and transmitting in an alternating fashion. A 5-cycle sine wave packet, at a frequency of 57 kHz and output power of approximately 130 decibels is transmitted around the path, alternating in direction, and detected at the beginning and end of the path by microphones at the base of the tower. Figure 3.2 shows an example of signal signatures received by the microphones, and the resulting indication of $t_{(+)}$ or $t_{(-)}$ values, depending upon the direction the signal was sent. The image is not to scale.

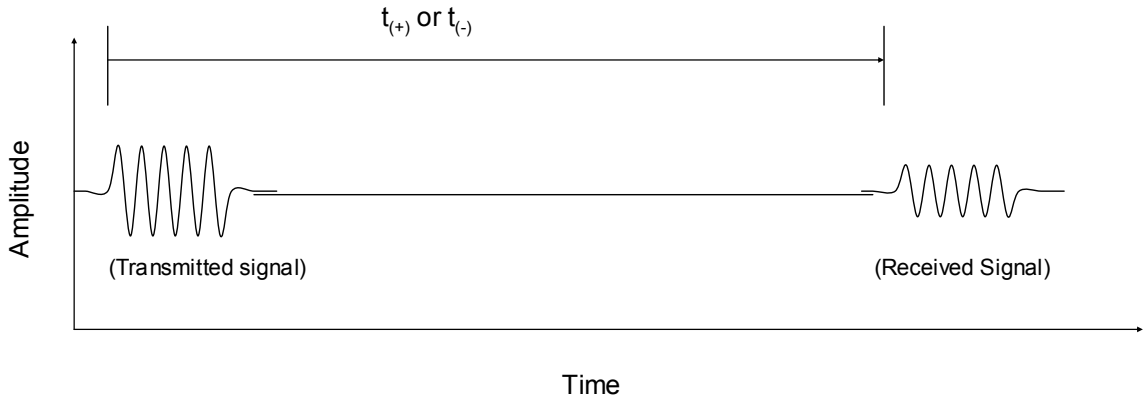

Figure 3.2 – Schematic of signals received from microphones, and corresponding indications of t values.

The ultrasonic signal is monitored using microphones and collected through a data acquisition system sampling at 285 kHz, controlled by a laptop computer using Lab View Software. The signals detected at the beginning and end of the path are filtered, processed and analyzed to determine the travel time of the acoustic pulse around the path. The travel times were then compared for successive pulses to determine the difference in travel time. These time values were converted to circulation intensity values using Equation (2.12). The interval of pulse transmission was 0.75 seconds, resulting in a

sampling frequency of 1.33 Hz over an approximately 2 minute sampling period. An attempt was made to capture 30 seconds of data prior to aircraft fly-by for each trial.

3.2 Equipment

The detection of wake vortices using ultrasonic pulses requires the basic equipment setup outlined in the block diagram in Figure 3.3. A signal generator outputs our acoustic signal, which is amplified and transmitted by two transducers. Microphones detect the signal at the beginning and end of the acoustic path, and feed the data into a data acquisition system, which then stores on a laptop computer. This section outlines the details of the equipment in the following order: transducers, microphones, data acquisition, and other hardware.

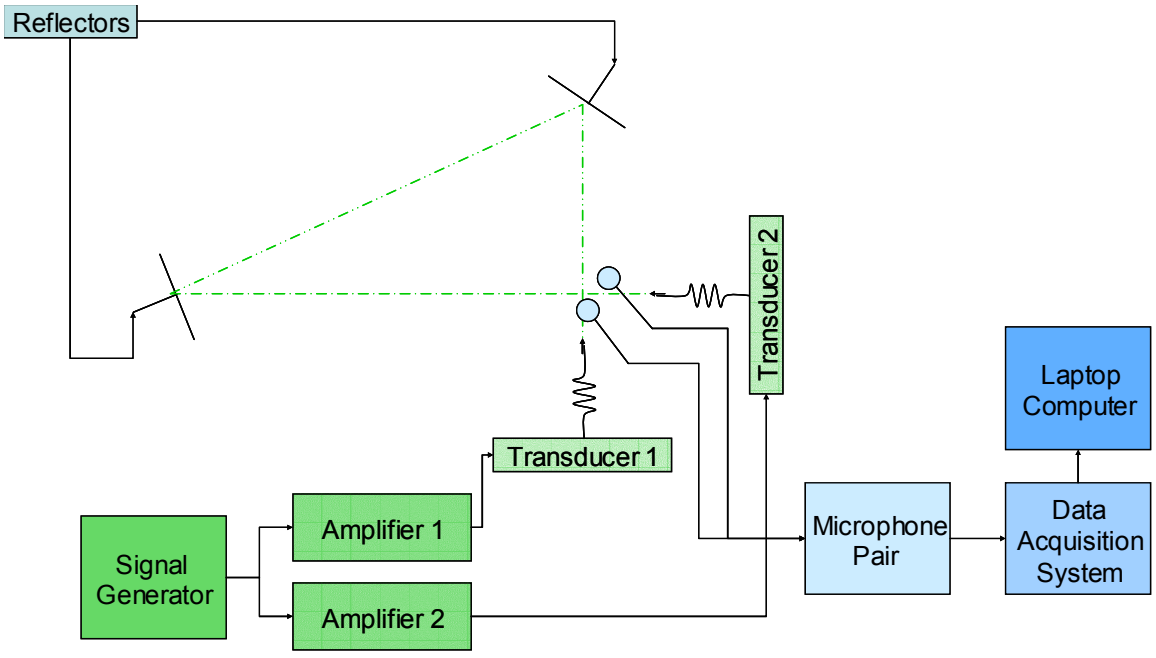

Figure 3.3 – Block diagram of equipment setup used in field testing

The ultrasonic transducers used in this experiment are a film-based piezoelectric array produced by Holosonics, Inc. The transducer is a hexagon shape with a width of 18

inches and was purchased with the Holosonics amplifier. The equipment supplied by Holosonics was modified slightly from a typical model, in that the amplifier functions solely as an amplifier without any signal manipulation which the standard Holosonics model provides. A key feature of these transducers is the output strength and the directionality. The maximum power output is approximately 130 dB. The array transducer is also practically unidirectional in its output. The manufacturer states the total beam spread is less than 3 degrees. Figure 3.4 shows these transducers in position at the base of the tower.

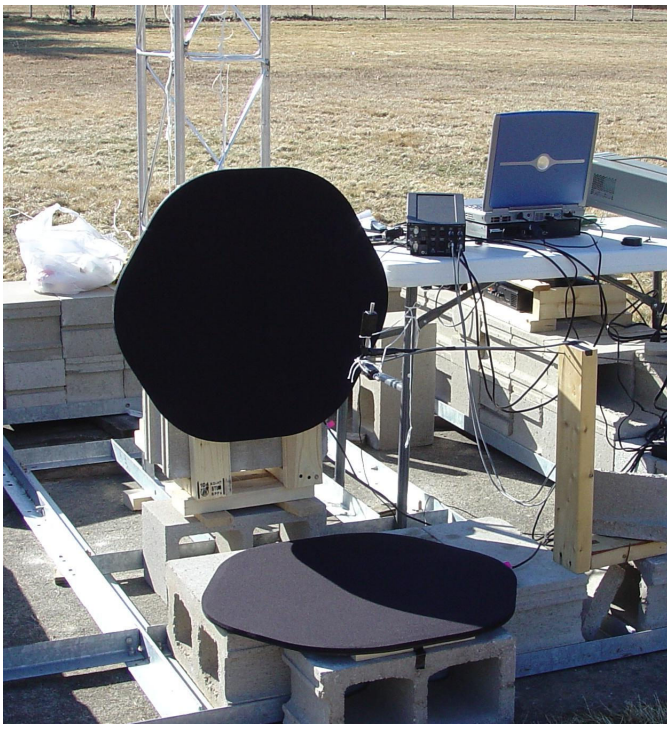

Figure 3.4 – Ultrasonic transducers positioned at the base of tower

Two microphones are placed in the transmission path, and received the signals at the beginning and end of the designated path. The microphones and conditioning amplifiers used were from Bruel and Kjaer, model numbers 1290A and 2690, respectively. The microphone setup consists of a microphone and conditioning

preamplifier, and a conditioning amplifier unit with instantaneous signal display capabilities. These microphones were selected for their large frequency range and low inherent noise, which are 4 – 100,000 Hz and 28 dB respectively. The conditioning preamplifier has a range of gain settings as well, with 1 V/Pa corresponding to zero gain. The gain setting was 316 mV/Pa for trials one through fourteen.

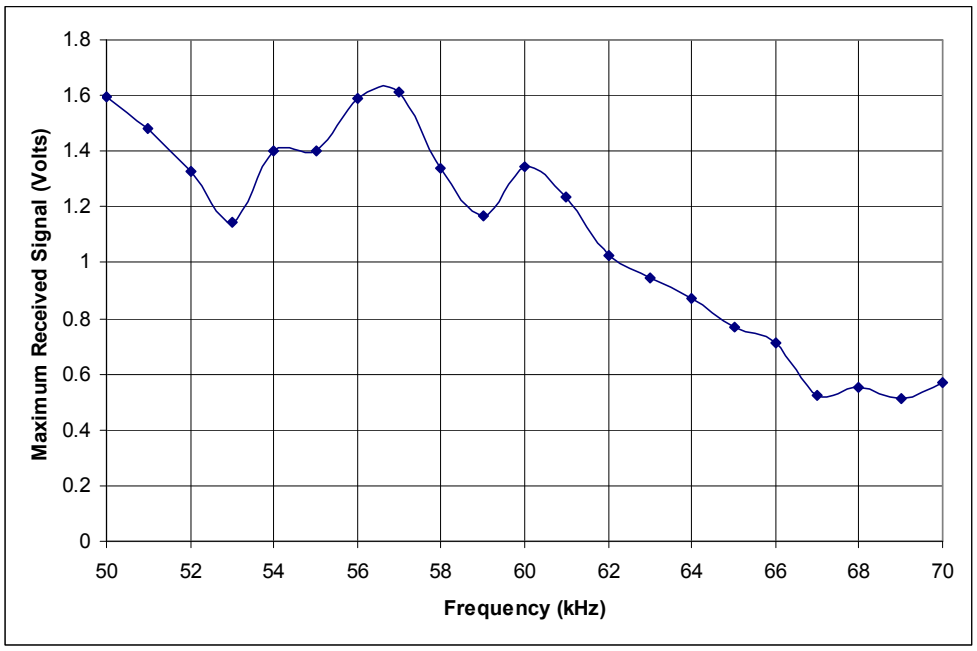

Figure 3.5 – Received signal strength vs. frequency of transducers and microphones

The transducer manufacturer stated the optimal output frequency of the transducers is 64 kHz, and the output frequency range fell within a fairly narrow window around that point. Laboratory testing revealed the transducer and microphone pair had an optimal frequency of 57 kHz. This varies from the transducers stated manufacturer optimal frequency most likely due to the fact that the microphone frequency response is not constant in this frequency range. Figure 3.5 shows a graph of the received signal vs. transmitted frequency used to determine the combined optimal frequency of the transducers and microphones.

The signal received by the microphones was fed into a data acquisition system, DAQ-Pad 6070E with fire-wire, from National Instruments. This data acquisition system has a maximum sample rate of 1.25 kHz over 16 input channels, and two output channels. Input channels can receive signals up to +/- 5 Volts (V) with zero gain, but are capable of receiving a maximum voltage of +/- 10V. It has a 12-bit TTL resolution and the precision at the input range of +/- 5V is 2.44 mV. Sampling in this experiment occurred at 285 kHz, with input channels set to +/- 5 Volts.

Other equipment included a signal generator, tower, acoustic reflectors, and laptop computer. The acoustic signals are generated with a Hewlett Packard Aligent 3314A signal generator. This signal generator was set to transmit packets (N = 5 cycles) of sine wave at the desired frequency (f = 57 kHz), amplitude (A = 3.25 Volts), and interval frequency (I_f = 1.33 Hz). The signals are sent through a manual switch which was operated to alternate transmission of pulse packets between the two amplifiers.

The acoustic reflectors were 3 foot square sheets of aluminum, set in precise locations using a transit, level, and plumb lines, so as to reflect the signal transmitted from both transducers around a closed path. The towers used to support the aerial reflector were Novalynx 30-foot aluminum towers, model # 190-611, with a customized portable base. Aluminum mounting arm and reflector support system was also custom made for this application at WPI.

Acquired data were stored and analyzed using National Instruments Lab View software, version 7.0. Separate programs were written by this author for data collection and data analysis. The end result of signal processing is calculation of a series of delta-t

values as a function of time, which were correlated into circulation values as a function of time.

3.3 Signal Processing

Each experiment trial resulted in the generation of a single database file (.dbf) that contained the data from continuous sampling of two DAQ channels (one for each microphone) during entire trial. Using a second Lab View program, these original data files were broken into segments and converted into Lab View measurement files (.lvm). Each Lab View measurement file segment contained the transmitted and received signal.

Using a third program, each of these file segments were filtered with a high-pass Butterworth filter set to 20 kHz. Segments of 100 samples surrounding the transmitted and received pulses were removed from the overall segment, normalized to amplitude of 1, and cross-correlated, *R*, by Lab View using equation 3.1. The index value between the two 100-sample segments, combined with the maximum correlation index was used to determine the overall separation between the two pulses, and thus determine the travel time. Figures 3.6 and 3.7 depict schematics of the signal processing procedure.

$$R(t) = x(t) \otimes y(t) = \int_{-\infty}^{\infty} x(\tau) y(t+\tau) d\tau \tag{3.1}$$

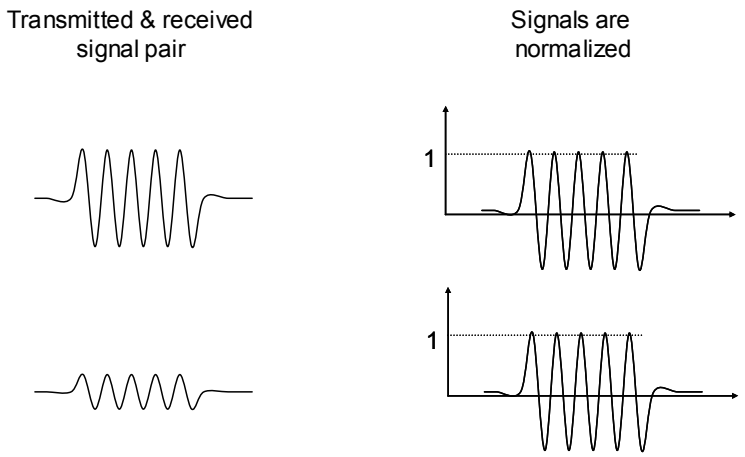

Figure 3.6 – Schematic of signals received by microphones, and normalizations.

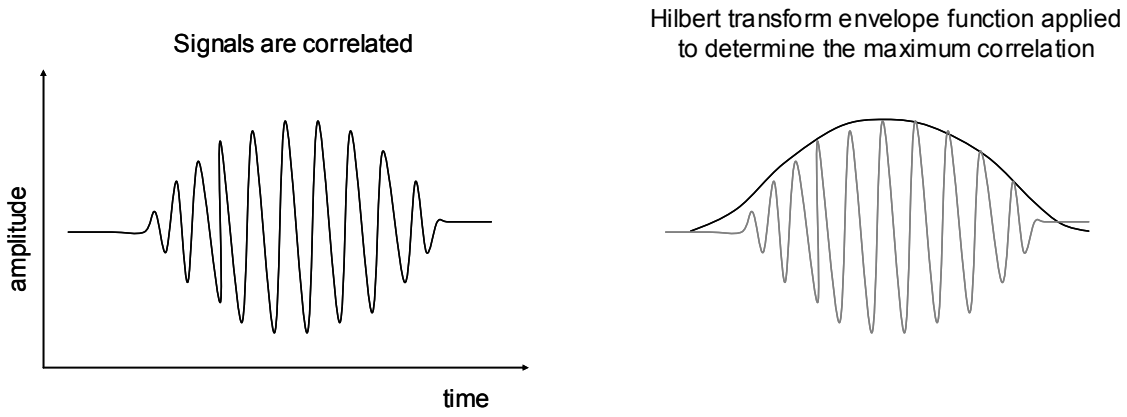

Figure 3.7 – Schematic of signal correlation function and Hilbert envelope function.

To precisely determine the maximum value of correlation, an envelope function of the correlation was calculated using the Hilbert transform. The Hilbert envelope function, *E*, shown in Equation 3.2, is a commonly used technique for determining the maximum of an oscillating function (Long, et. al, 1992; Andrade and Messina, 2005). It displays the total energy curve as a function of time, and utilizes the Hilbert Transform, H. The Hilbert transform is calculated using Lab View, and is defined in equation 3.3, with *x(t)* representing the function to be transformed. This maximum correlation index is combined with the elapsed time between the two 100 sample segments to determine the

total time it took that single pulse to traverse the path. The exact same procedure was done on the pulse traveling in the opposite direction; these time values are recorded as $t_{(+)}$ and $t_{(-)}$, defined in section 2.1. For each successive pulse pair, the propagation times are compared to determine the delta-time for the signal pair.

$$E = \left[R^2(t) + \left[\mathrm{H}\{R(t)\}\right]^2\right]^{1/2} \tag{3.2}$$

$$\mathrm{H}\{x(t)\} = \frac{-1}{\pi}\int_{-\infty}^{\infty}\frac{x(\tau)}{t-\tau}\,d\tau \tag{3.3}$$

Each signal pair was processed similarly with the end result being a series of delta-t values as a function of time for the duration of the sample. The delta-t values were converted to circulation values using Equation 2.12. All Lab View programs front panel and block diagram can be found in Appendix I.

There is an inherent error present within this measuring system due to sampling and correlation technique. The data acquisition system introduces an error of magnitude 1/(sample rate), which is 1/(285000 Hz) = 3.5 microseconds. The cross correlation technique should yield an error no greater than one cycle, which is 1/(57000 Hz) = 18 microseconds. The peak detection technique using the Hilbert Envelope function should introduce an error no greater than one-half a cycle, or 9 microseconds. The total error, ε_{total}, from all three sources can be determined using a standard error in sum formula, Equation 3.4, which is calculated to be 20 microseconds.

$$\varepsilon_{\text{total}} = \sqrt{\varepsilon_1^2 + \varepsilon_2^2 + \varepsilon_3^2} \tag{3.4}$$

A total error of 20 microseconds is present for each time calculation, yet circulations are based on time difference values. For the time difference value, the total error from both time samples can be determined using the same method, and is found to be 28 microseconds. This results in an overall error in circulation measurements of $\pm$ 1.5 m^2/s for all data points.

4 Results

Data were first collected during two testing dates, chosen for their ideal atmospheric conditions. This chapter includes results from these initial tests which show this technology is able to detect the wake vortices generated from the Piper PA-32 aircraft. A second trial was conducted in non-ideal atmospheric conditions, a hot sunny day with afternoon convection, to test the systems performance. Extensive analysis has been conducted of these trials, and analysis methodologies and results are shown in this chapter as well. In addition, various other data were collected to show variations in ambient atmospheric circulation levels, ambient noise levels, and noise emissions in the ultrasonic frequency range from various aircraft.

4.1 Ideal Atmospheric Conditions

Three flight paths were used during the fourteen trial flights conducted on two testing days: Path A was with the plane closest to the tower with one wing and body of plane within our observed area, path B was with the plane farther from tower with just the wing tip within the observed area, and path C was with entire plane outside the observed area. The expected motion of the vortices shed from the plane in the calm air is downward due to the motion they induce on each other, and to separate laterally due to interaction with the ground. Figure 4.1 shows the schematics of these three flight paths.

Despite pilot attempts to place the aircraft precisely in the designated path, variations of path did occur. During certain flights the plane was witnessed to be shifted horizontally or vertically by several feet of ideal placement. These variations will result in a variation of vortex track and timing of entry and exit of measurement area, but will

not affect the vortex traveling into our measurement area. Detection of a peak vortex circulation value within the measurement area may be offset due to flight variations, but should be observed in all cases. Variations in aircraft placement will result in variations in the duration the vortex remains within our measurement area, and therefore variations in the decay rate may be observed.

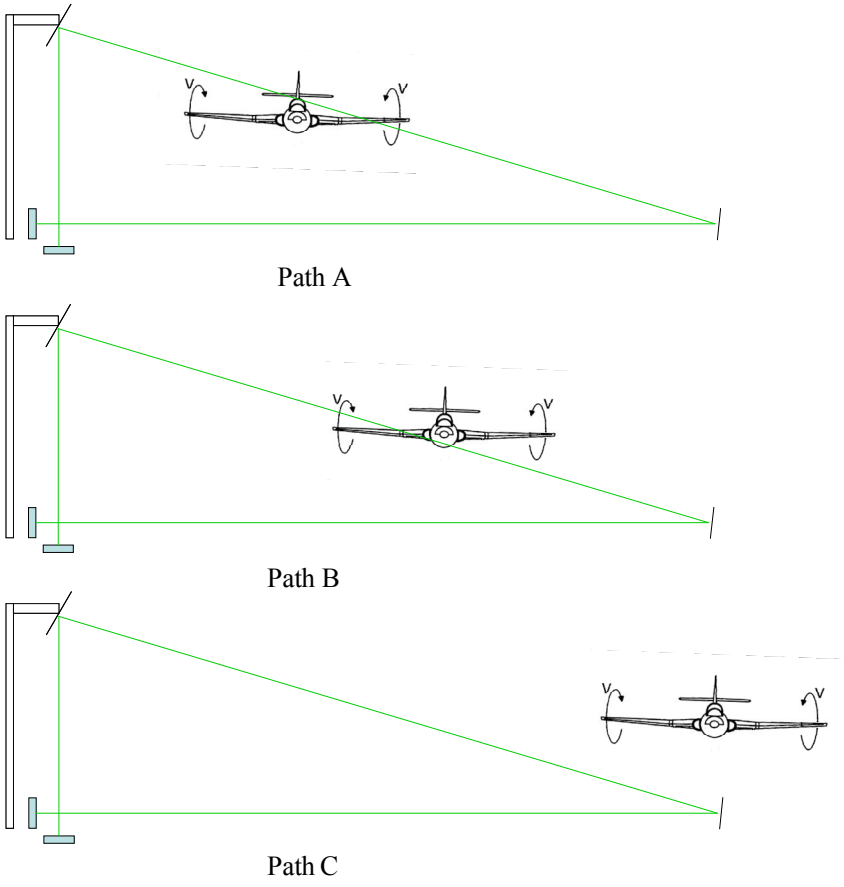

Figure 4.1 – Schematics of three flight paths used during field testing

An expected circulation value of the wake vortex generated by the aircraft was calculated for each trial flight. Knowledge of the aircraft lift, flight speed during fly-by, wing span and density of air, enables a calculation of the theoretical vortex strength shed behind each wing using the modified Kutta-Joukowski theorem shown in Eq. (4.1). Table 4.1 shows a summary of the meteorological conditions and aircraft statistics for each trial

conducted. Flap settings range from 0-3, indicating no flaps to full flaps, respectively. Lift was approximated by the weight of the aircraft and contents since relatively level flight was maintained while aircraft passed test area. Air density was assumed to be 1.25 kg/m^3, and wing semi-span b′ is 4 meters. It is expected that the circulation values will be positive based on the direction of flight and method of Δt calculations.

$$\Gamma \approx \frac{(1/2)L}{\rho V b'} \tag{4.1}$$

Table 4.1 – Meteorological and aircraft information for each trial flight, with expected circulation values calculated.

Trial	Date	Temp (ºC)	Winds (observed)	Flight Path	Aircraft Mass	Flight Speed	Flap Setting	Lift (N)	Circulation (m^2/s)
1	4/10/05	7	Calm	A	993 kg	31 m/s	3	9731	31.4
2	4/10/05	7	Calm	A	993 kg	30 m/s	3	9731	32.4
3	4/10/05	7	Calm	A	993 kg	31 m/s	3	9731	31.4
4	4/10/05	8	Calm	A	993 kg	31 m/s	3	9731	31.4
5	4/10/05	8	Slight breeze	A	993 kg	31 m/s	3	9731	31.4
6	4/16/05	-1	Calm	A	1012 kg	36 m/s	3	9918	27.6
7	4/16/05	-1	Calm	A	1012 kg	33 m/s	3	9918	30.1
8	4/16/05	-1	Calm	A	1012 kg	35 m/s	3	9918	28.3
9	4/16/05	0	Calm	C	1012 kg	35 m/s	3	9918	28.3
10	4/16/05	0	Calm	C	1012 kg	35 m/s	3	9918	28.3
11	4/16/05	0	Slight breeze	C	1012 kg	34 m/s	2	9918	29.2
12	4/16/05	3	Slight breeze	B	1012 kg	30 m/s	3	9918	33.1
13	4/16/05	3	Slight breeze	B	1012 kg	32 m/s	2	9918	31.0
14	4/16/05	3	Slight breeze	B	1012 kg	32 m/s	2	9918	31.0

Figure 4.2 shows a typical example of signal data from one pulse pair. Depicted in this figure is the filtered, normalized, 100-sample segment of the pulse before and after transmission along the acoustic path, the correlation function, and the Hilbert transform envelope function.

Figure 4.3 shows circulation data gathered from one trial flight. This graph shows actual data points plotted, along with a running average of five data points shown by the solid line. The graph is setup such that the aircraft passes by the measurement equipment at time zero. Prior to aircraft passage it is clear that circulation values have some natural variation, yet are essentially zero. Circulation spikes immediately after aircraft passage, and then decreases back to ambient levels within 60 seconds.

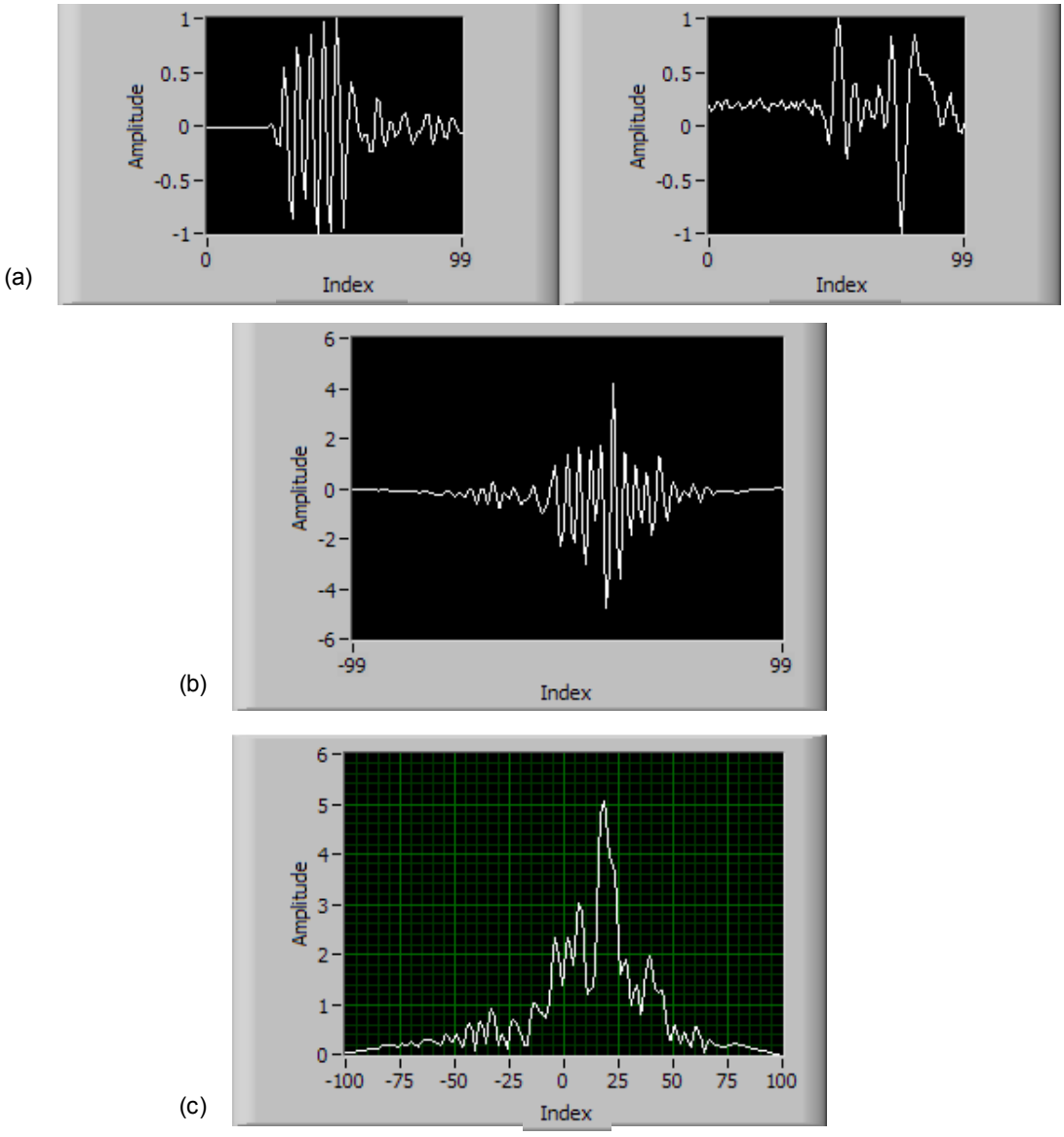

Figure 4.2 – Representative example of (a) actual signals recorded, (b) the correlation function, and (c) corresponding Hilbert transform envelope function.

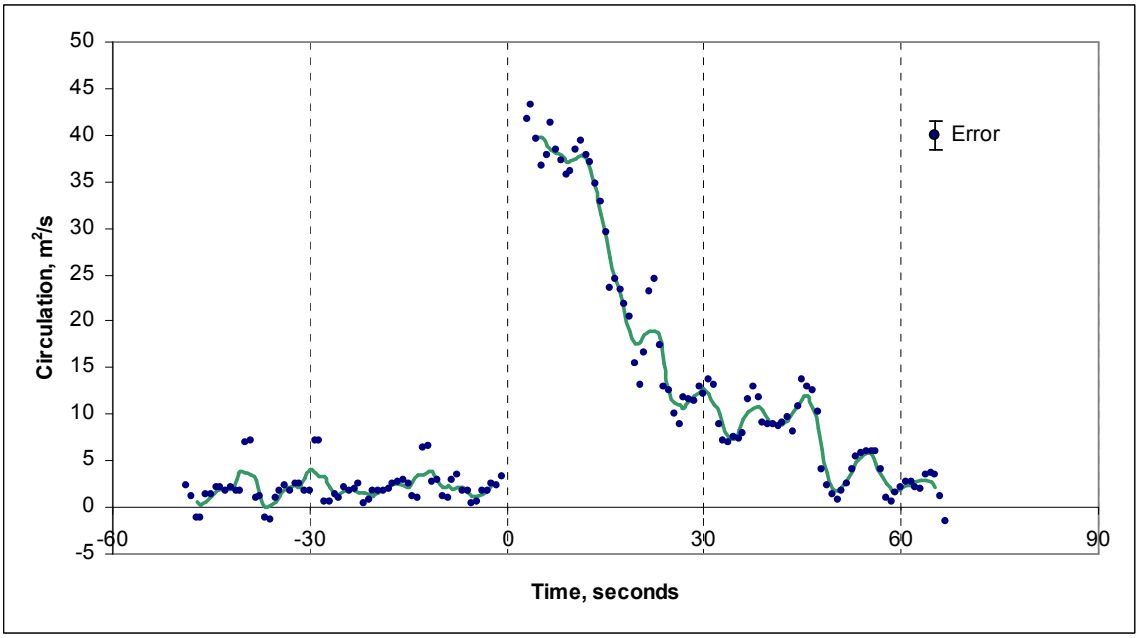

Figure 4.3 – Circulation vs. time for trial 6, solid line is a 5-point running average of data

During the first day of data collection five passes were conducted using flight path A, and on the second day of data collected three passes each were made using flight paths A, B, and C, as shown in Figure 4.1. For all trials the plane passes the cross sectional area at time zero. Figures 4.4 and 4.5 display circulation values vs. time observed from path A flights during the first and second day of data collection, respectively. Figures 4.6 and 4.7 display data collected during second day for flight paths B and C. Figures 4.4 - 4.7 show an averaged circulation using a running average of five data points. Individual graphs for each flight can be found in Appendix II.

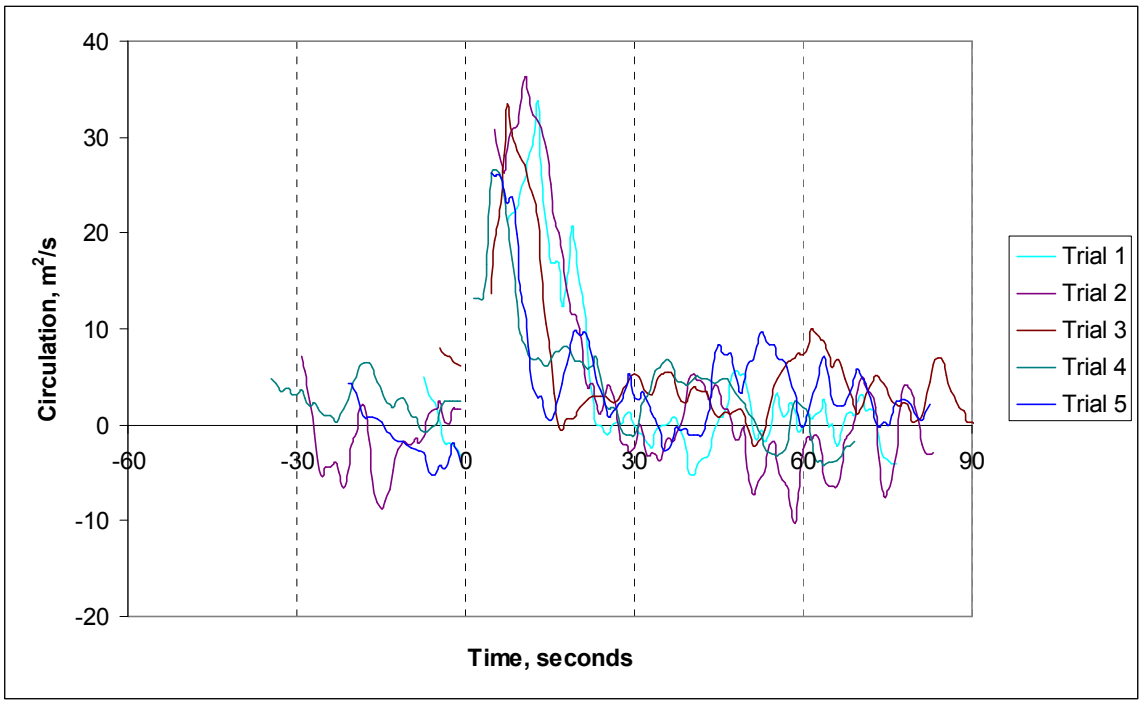

Figure 4.4 – Averaged circulation data for day one trials using flight path A.

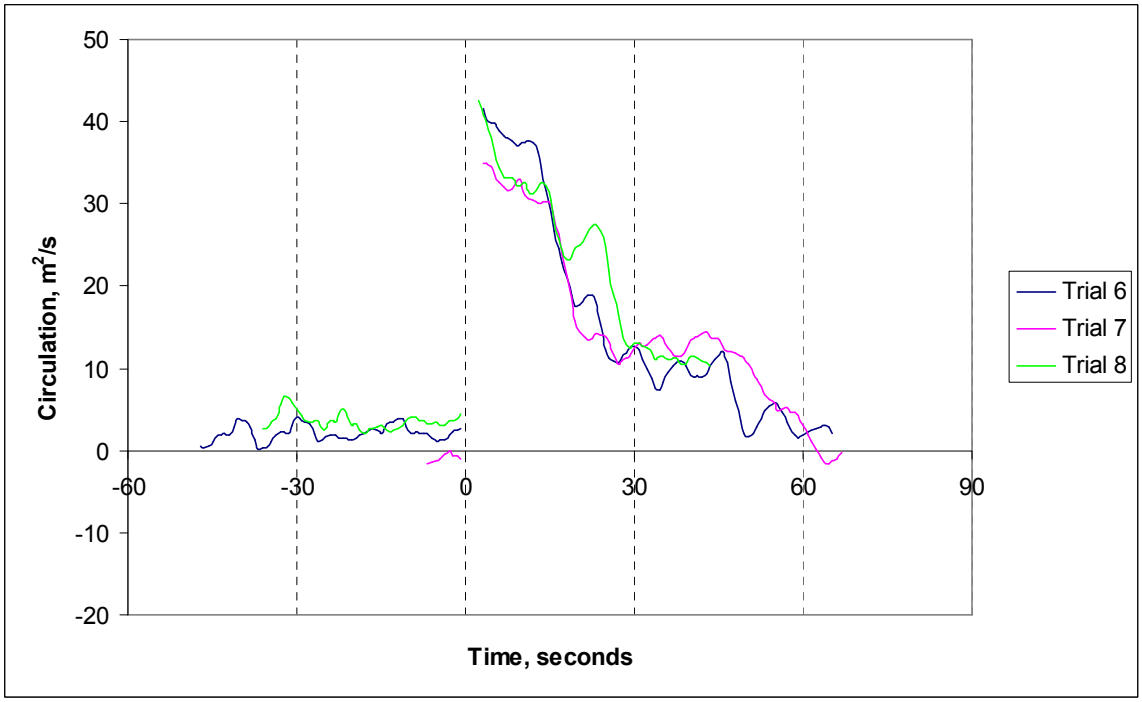

Figure 4.5 – Averaged circulation data for day two trials using flight path A.

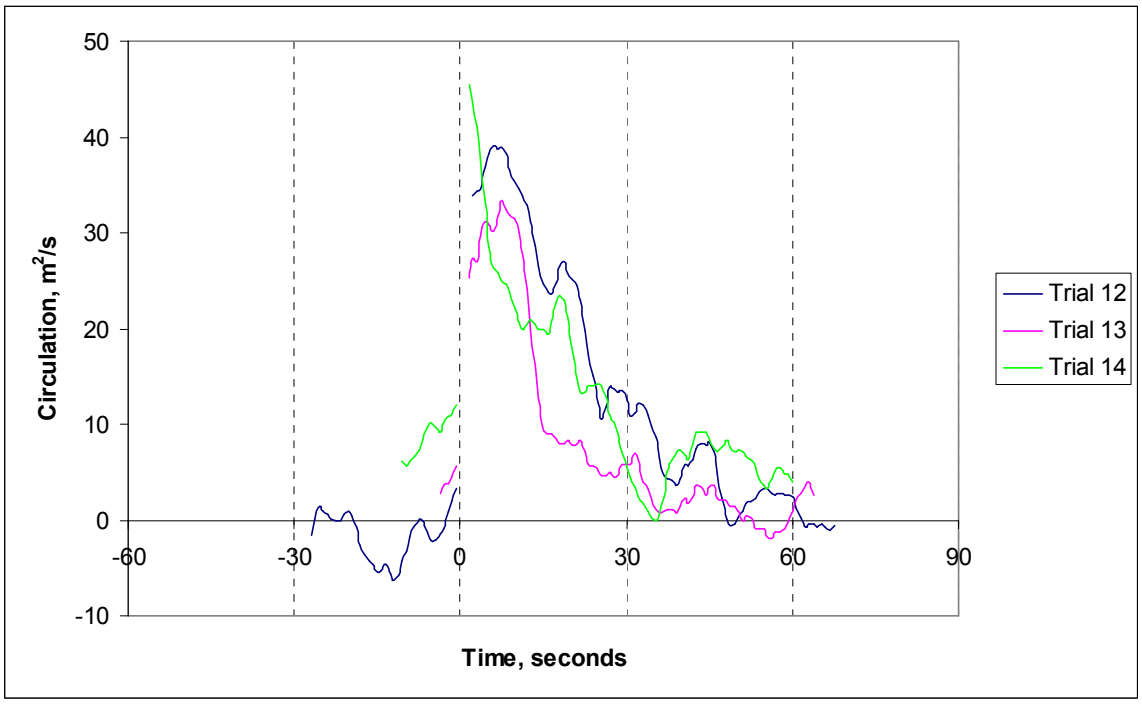

Figure 4.6 – Averaged circulation data for trials using flight path B.

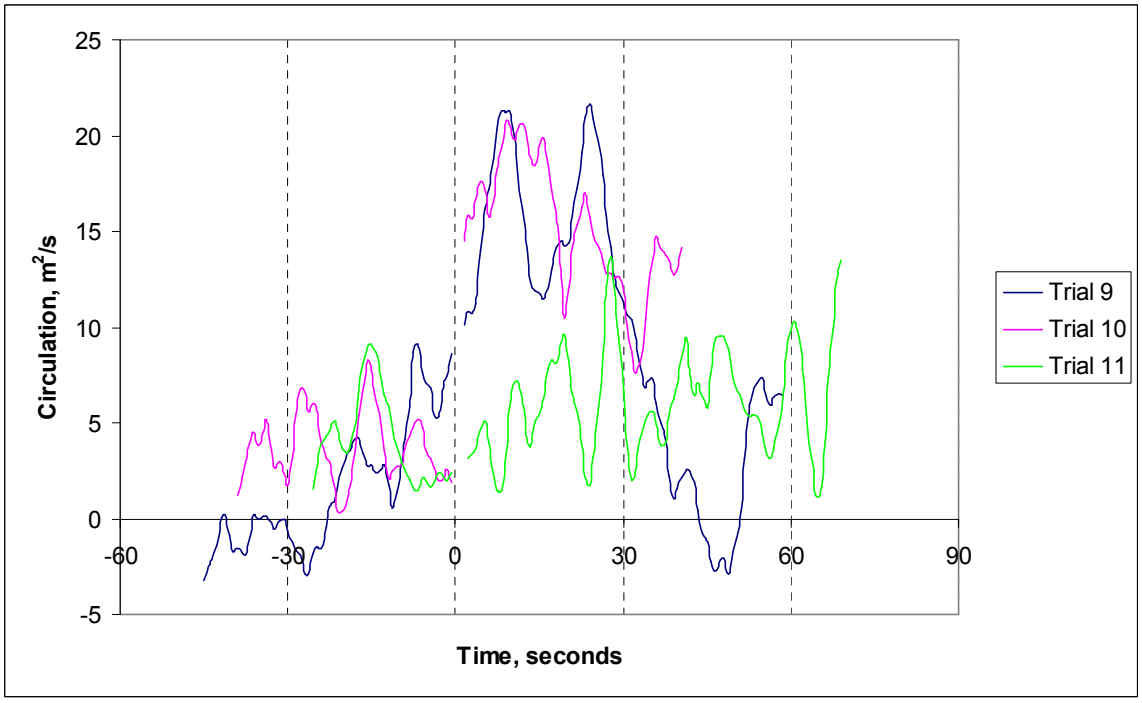

Figure 4.7 – Averaged circulation data for trials using flight path C.

Ambient noise and ambient circulations were also measured at Tanner-Hiller Airport prior to data collection. Ambient noise was measured with no aircraft operating in the area, and is shown in Figure 4.8. A Fast Fourier Transform is used to convert the data into the frequency spectrum. It is observed that for our pulse transmission frequency of 57 kHz, there is no significant ambient noise level.

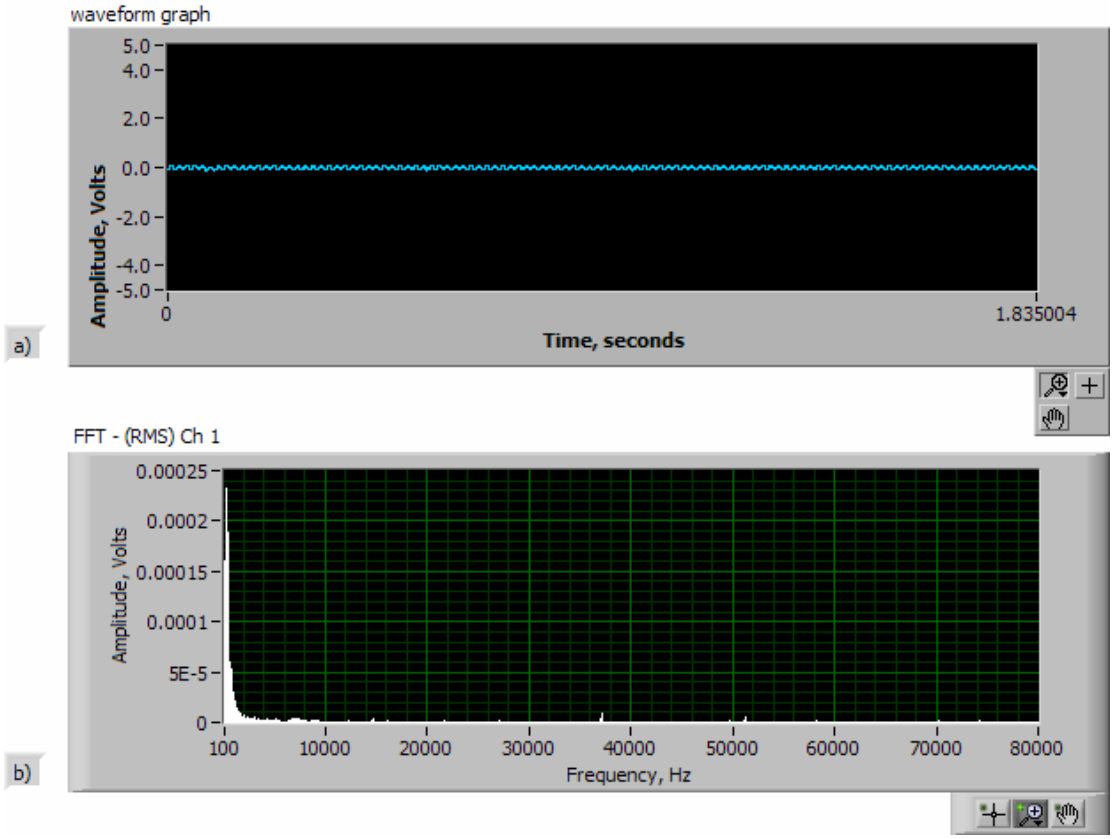

Figure 4.8 – Ambient noise waveform, amplitude vs. time in (a), and amplitude vs. frequency in (b), at Tanner-Hiller, 04-10-05, without air traffic

Figure 4.9 shows ambient atmospheric circulation levels measured at Tanner-Hiller prior to field testing. It is apparent that ambient circulations are very weak, which is expected in conditions of minimal wind and convection. Statistical analysis of this ambient circulation shows the average and standard deviation are 2.06 m^2/s and 1.86 m^2/s, respectively.

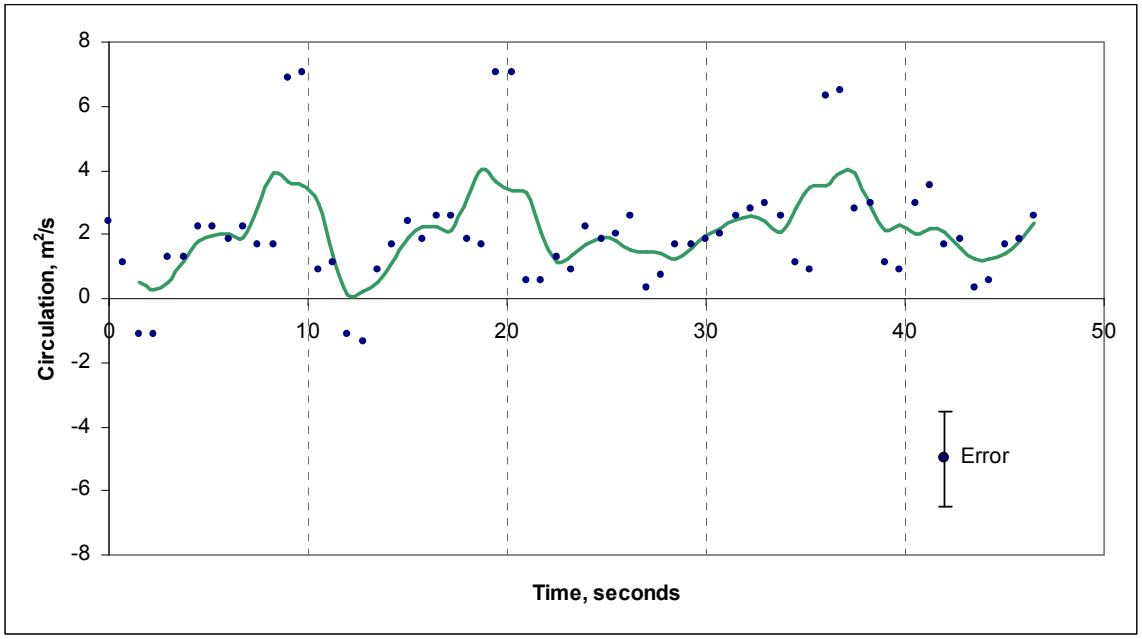

Figure 4.9 – Example of ambient atmospheric circulations that existed at Tanner-Hiller Airport prior to testing, 4-16-05, solid line is a 5-point running average of data points

4.1.1 Analysis of Data in Ideal Atmospheric Conditions

Adjustments were made to the raw delta-t and circulation values in order to achieve the results shown in section 4.1. This analysis consisted of discarding delta-t values due to aircraft noise pollution and other errors, and making adjustments for microphone placement. All graphs depicted in section 4.1 and Appendix II have been corrected using the following techniques.

Aircraft noise overwhelmed the microphones for approximately three seconds as it passed by the measurement equipment. Filtering helped reduce the aircraft noise, but for a few seconds it did result in an inability to detect the transmitted acoustic pulse. For these periods of time, where the signal could not be detected, the data points were removed from the data set. It is believed that extensive filtering could reduce this noise contamination even further, however for this study only simple filtering was applied.

In addition, for each successive pulse pair a value of speed of sound can be calculated. This speed of sound calculation is used to determine the accuracy of the data points. If the speed of sound calculation was significantly different from the preceding or following values calculated for speed of sound, then the data point was removed from the data set. Errors of this nature were most likely due to signal not being detected on its return, which results in correlations being performed between a signal and a sample of ambient noise; the resulting delta-t value will be incorrect. Table 4.2 shows the average speed of sound calculation for all fourteen trials, along with standard deviation in speed of sound. While this analysis was performed manually, this technique of using instantaneous speed of sound calculations to validate the integrity of a data point could be incorporated into future versions of analysis programming. Figure 4.10 graphs the instantaneous speed of sound vs. time for all fourteen trials. This figure illustrates the consistency of this value throughout a collection cycle, yet does vary with different trials as daytime temperatures were rising during times of data collection.

Table 4.2 – Statistics for Speed of Sound calculations for each field trial

	Speed of Sound	
Trial	**Average**	**Std. Dev**
1	327.8	0.11
2	328.5	0.15
3	328.8	0.16
4	329.1	0.09
5	329.5	0.14
6	326.2	0.05
7	326.3	0.05
8	326.4	0.05
9	326.6	0.08
10	326.7	0.08
11	326.8	0.08
12	328.1	0.09
13	328.3	0.08
14	328.5	0.09

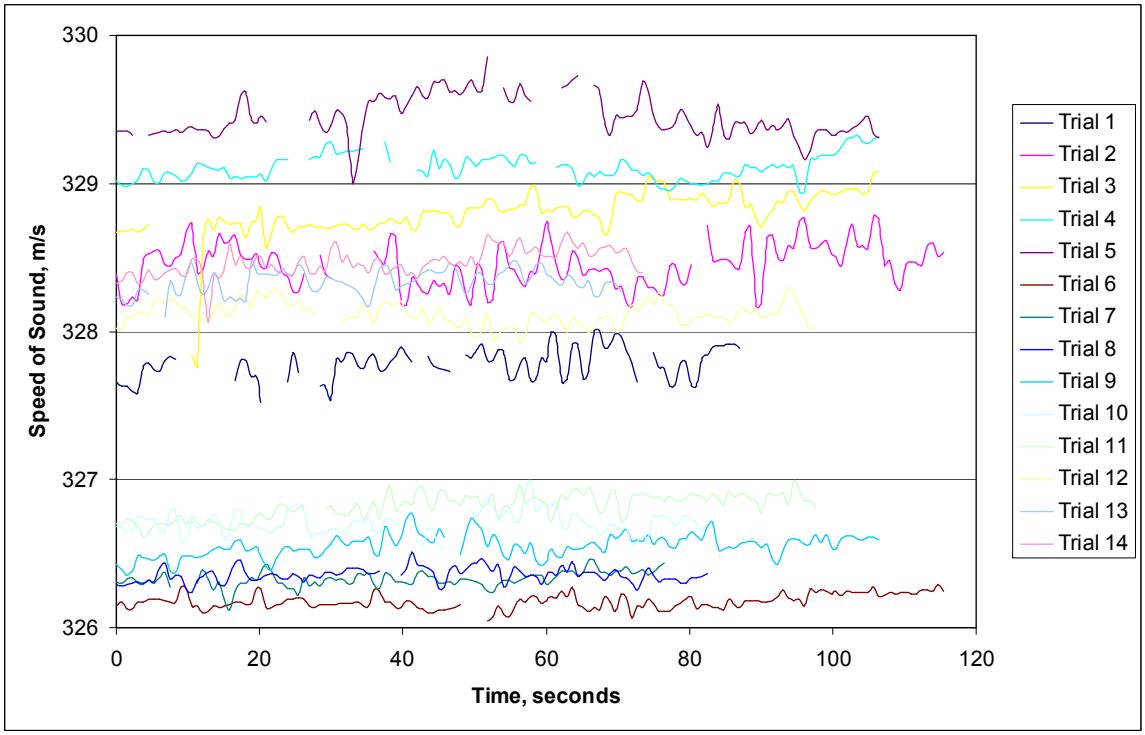

Figure 4.10 – Instantaneous speed of sound for each field trial plotted vs. time.

In determining a threshold for what deviation of speed of sound equates to data error rather than natural variation we can analyze a sample case. The equation for the speed of sound in an ideal gas is shown in equation 4.2. It was assumed that γ and R are constants with values of 1.4 and 287 J/(kg*K) respectively, yet temperature fluctuations can occur. Since speed of sound comparisons are done between successive pulse pairs, the time over which temperature changes occur to cause errors in speed of sound calculations is 0.75 seconds. Table 4.3 shows some examples of temperature changes, and the resulting effect on the speed of sound. It is apparent that even temperature fluctuations that would be extreme over a 0.75 second period, such as 2 degrees Celsius, will cause only a minor change in the speed of sound. It becomes apparent from this information that large changes in speed of sound indicate erroneous data, and removal

from the data set is appropriate. For data gathered in this study, variations larger than $\pm$ 1 m/s in the speed of sound was used as a threshold for erroneous data.

$$a = \sqrt{\gamma RT} \tag{4.2}$$

Table 4.3 – Examples of expected variations in sound speed in an ideal gas with various temperatures.

Temperature, Celsius	Speed of sound ($a=\sqrt{\gamma}RT$), m/s
273	331.2
274	331.8
275	332.4
280	335.4

Raw data sets for both days of testing in ideal atmospheric conditions showed an offset of ambient circulation values being negative at approximately 5-10 m^2/s. Analysis of our transmission path revealed the placement of the two microphones was such that the signals were not traveling a path that is exactly the same length. Figure 4.8 shows a schematic of this discrepancy. The exact length by which the transmission paths differed in opposite directions is unknown, since this was first realized well after the original testing. However, pictures taken of equipment setup were used to estimate the difference in path length, and a correction factor was added to all the pulse propagation times of the shorter direction of travel.

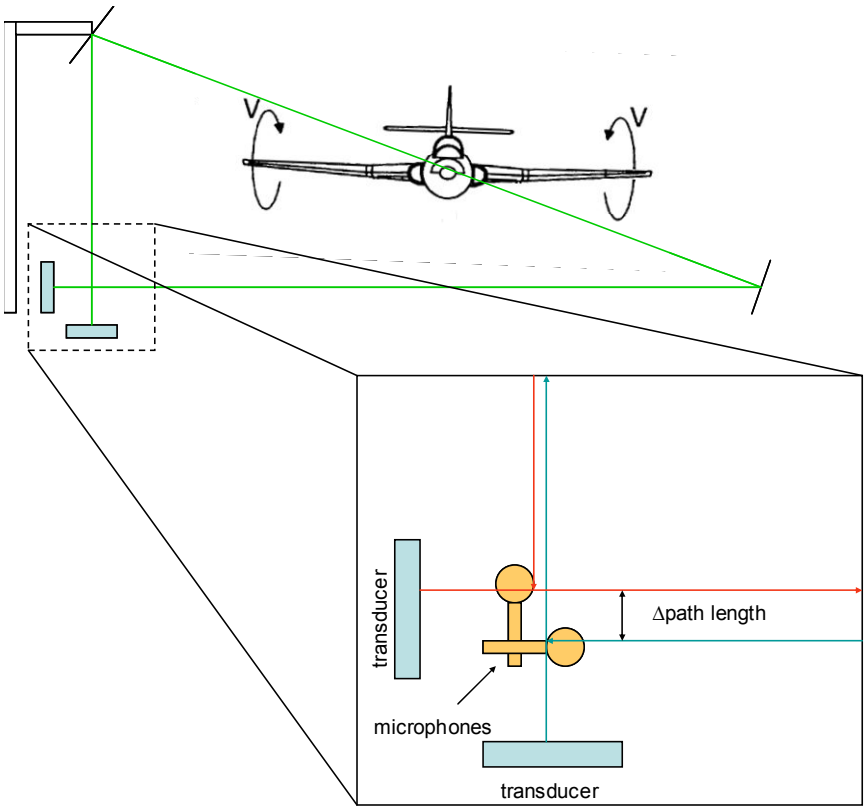

Figure 4.11 – Schematic of error caused by microphone placement within acoustic path. Opposite directed pulses traveled paths that differed in length by the Δpath length shown in this figure.

4.2 Results in Cross Wind Conditions

The second set of trials were conducted using a slightly different experimental setup and with non-ideal meteorological conditions. The acoustic path in this series of tests was not closed; the path segment along the ground was removed. This resulted in a shorter overall path length, which allowed experiments to occur during periods of high temperature and humidity when atmospheric attenuation of the sound signal is greatest. On this particular testing day a cross wind was also present within our acoustic measurement area.

Figure 4.12 – Experimental setup with no ground segment.

The experimental setup is shown in Figure 4.12. The position which previously held the ground reflector was replaced with one transducer and a microphone. The other transducer and microphone are still located at the base of the tower. Signals were redirected along the path just once, by the reflector mounted atop the tower. Additional cables were required to position the transducer and microphone farther away from the tower base, but the relocation was achieved without any loss in quality of signal due to

increased cable lengths. With the ground segment of the acoustic path eliminated, the no slip condition is invoked thereby assuming that zero velocity along the entire ground segment of the path. Revisiting equation 2.12, it is obvious that this assumption does not require any changes to the equations used to calculate circulation, as long as both the time values and path length, L, are based on the same path.

Six test flights were flown, all using flight path B, as illustrated in Figure 4.1. Figure 4.13 shows an aerial view of the test area, and includes the prevailing wind direction. No wind speed data was obtainable for Tanner-Hiller airport itself; however National Weather Service hourly observations indicated that wind speeds were variable between 5-10 knots for all surrounding observation stations. Wind direction was variable between Southwest and Northwest throughout the day, but was primarily out of the West-Northwest. Gusty conditions were also experienced on the Tanner-Hiller airfield during data collection.

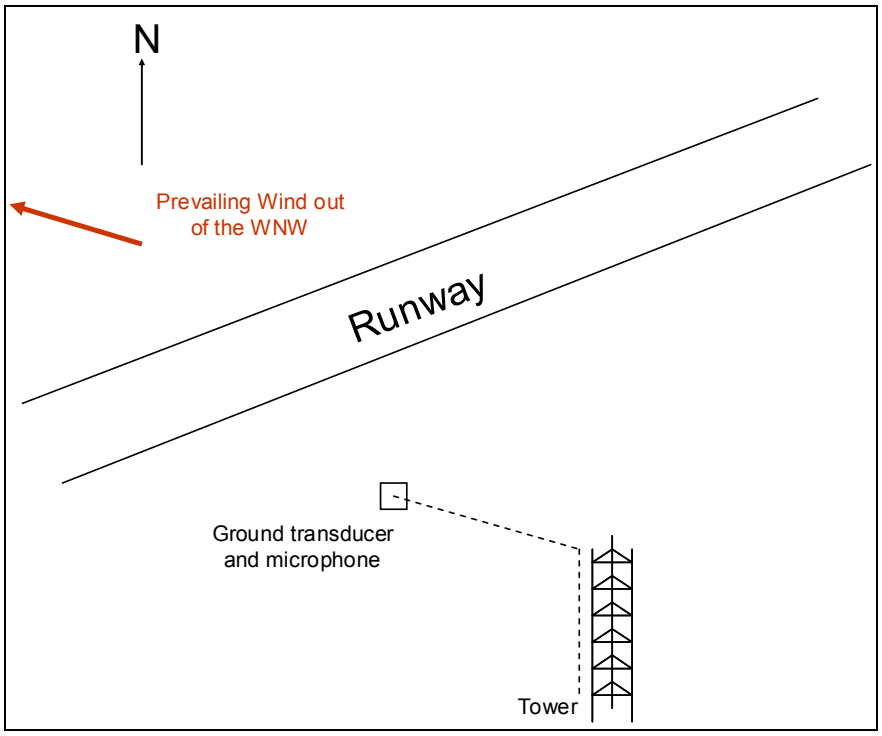

Figure 4.13 – Aerial view of equipment orientation and prevailing wind for testing in cross wind conditions.

It is observed that a component of the prevailing wind was providing a cross wind blowing from the ground equipment toward the tower. With this cross wind present we would expect the vortices to be blown toward the East-Southeast, which would bring both vortices through our acoustic path providing sufficient wind speeds to overcome the lateral propagation speed of the farthest vortex, which is traveling away from the tower.

All data collection and signal correlation technique is the same as described in Section 3.3. However, due to the shortened path length, the gain setting on the conditioning amplifier could be set to 1V/Pa, or zero gain. As in previous trials, signal packets of 5-cycle sine waves were transmitted at a frequency of 57 kHz, a frequency interval of 1.33 Hz, and amplitude of 3 Volts. Figure 4.14 shows an example of actual signals at beginning and end of transmission, and the resulting cross correlation function and Hilbert envelope function.

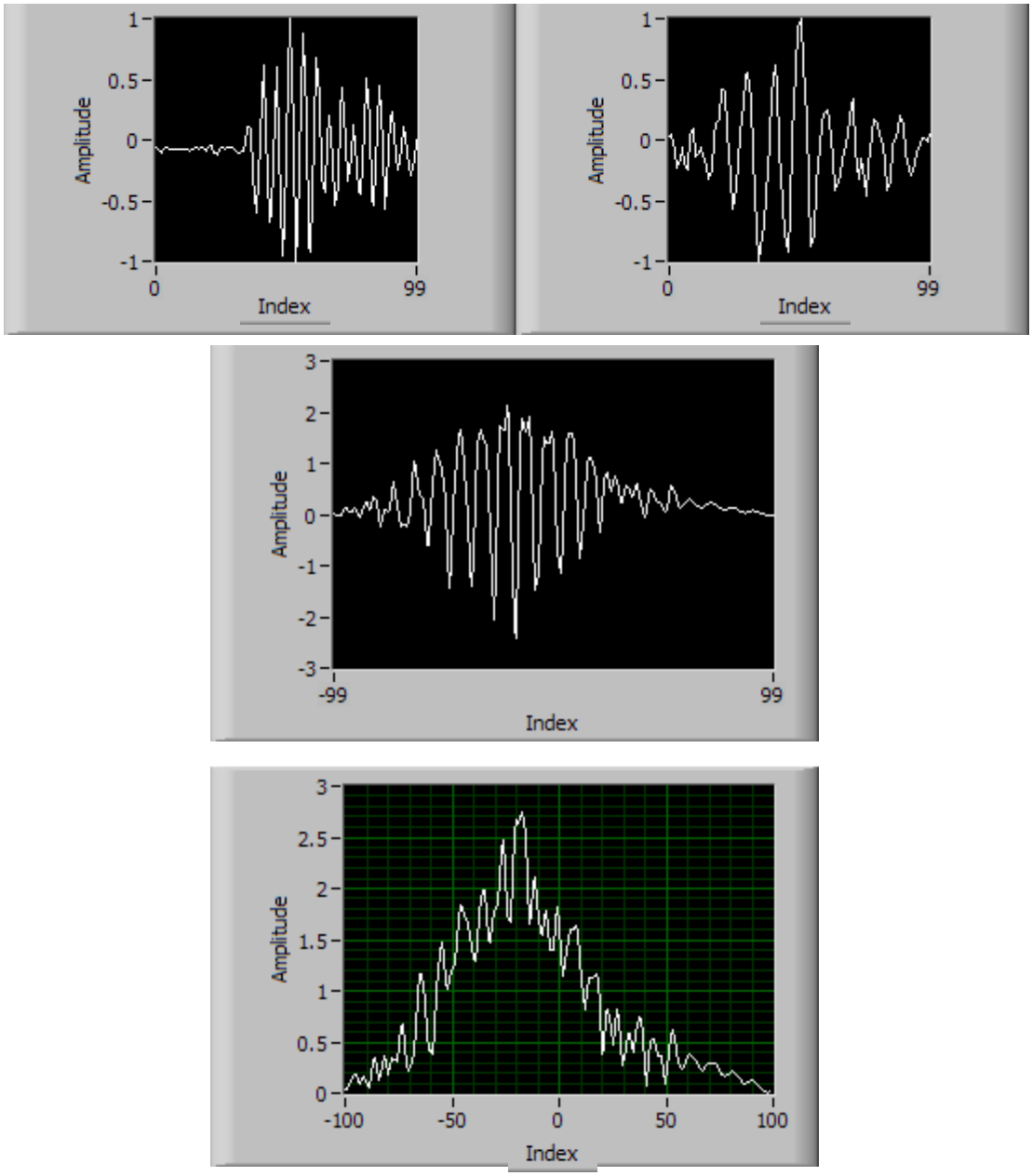

Figure 4.14 – Example of actual signal data gathered in cross wind conditions

The first vortex to arrive at the acoustic path is expected to have negative circulation values. The second vortex, if blown into the path, would have positive circulation values. Graphs depicting the circulation observed for each of the six flights are shown in Figures 4.15 through 4.20. In all cases, the aircraft passed the measurement

equipment at time zero. All plots depict actual observed circulation values with data points, and the line indicates a running average of five data points. Figure 4.21 shows the running average plotted for all six trials.

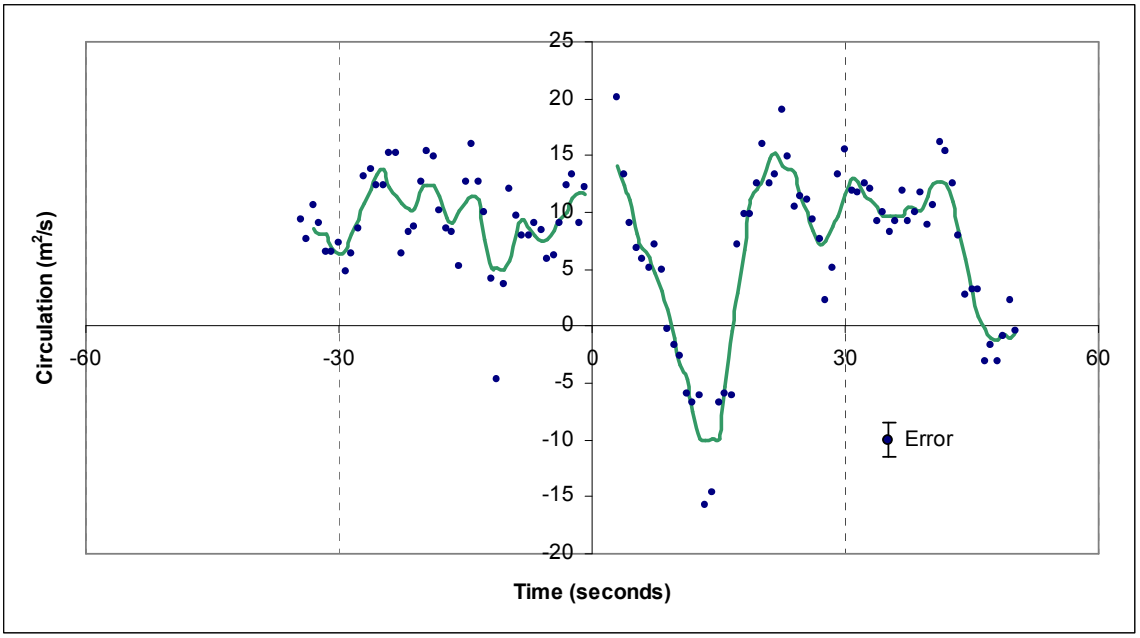

Figure 4.15 – Circulation vs. time for Trial 1 on 7-21-05 with cross wind

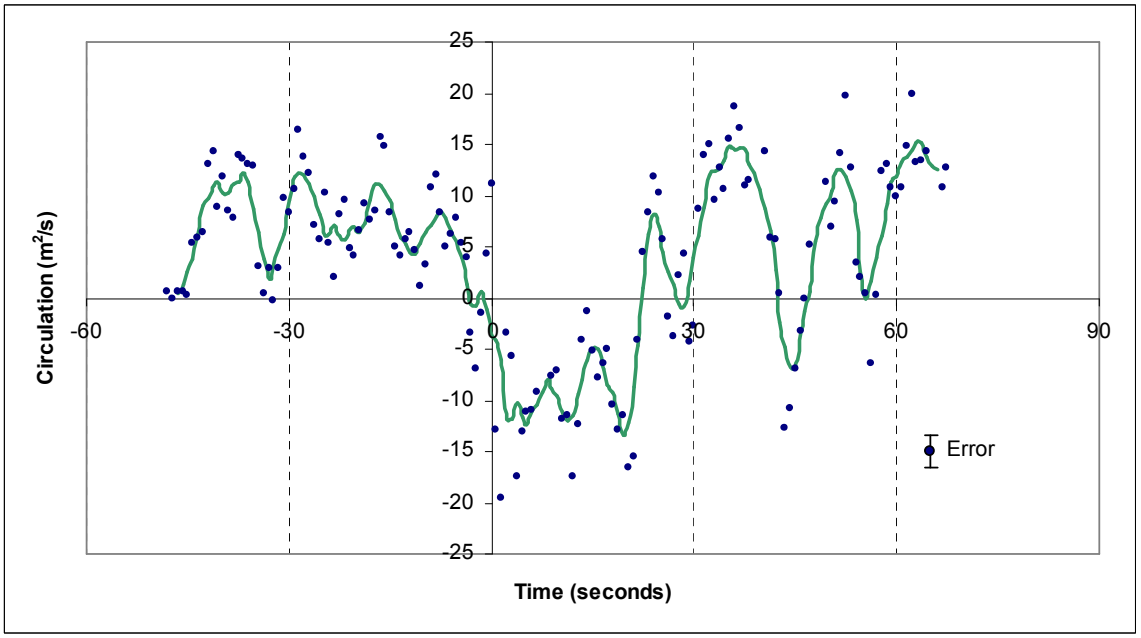

Figure 4.16 – Circulation vs. time for Trial 2 on 7-21-05 with cross wind

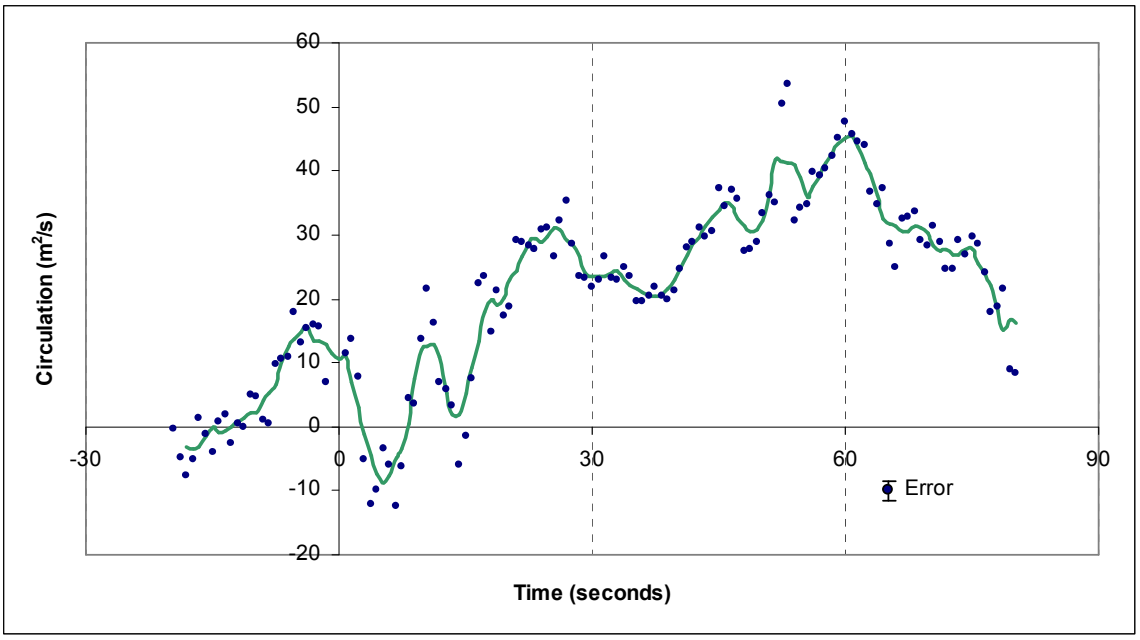

Figure 4.17 – Circulation vs. time for Trial 3 on 7-21-05 with cross wind

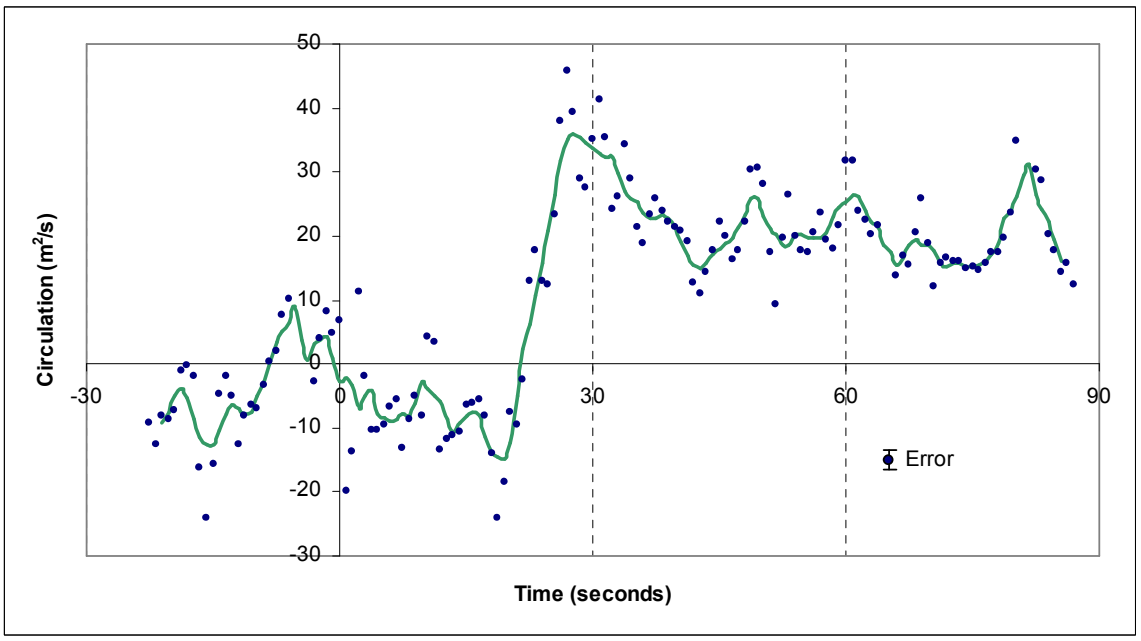

Figure 4.18 – Circulation vs. time for Trial 4 on 7-21-05 with cross wind

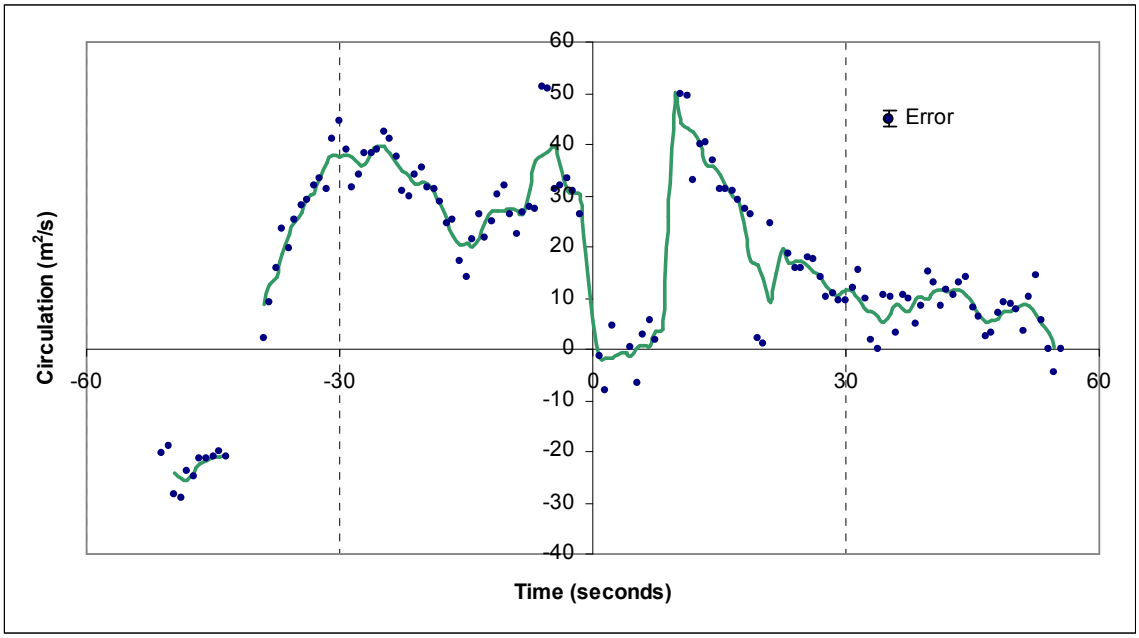

Figure 4.19 – Circulation vs. time for Trial 5 on 7-21-05 with cross wind

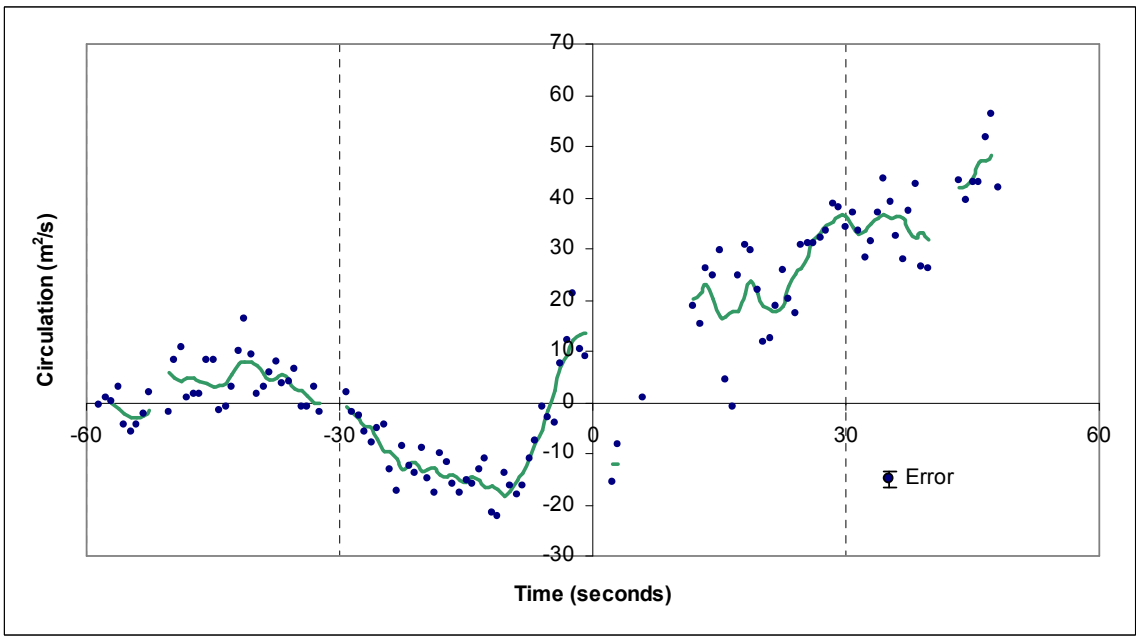

Figure 4.20 – Circulation vs. time for Trial 6 on 7-21-05 with cross wind

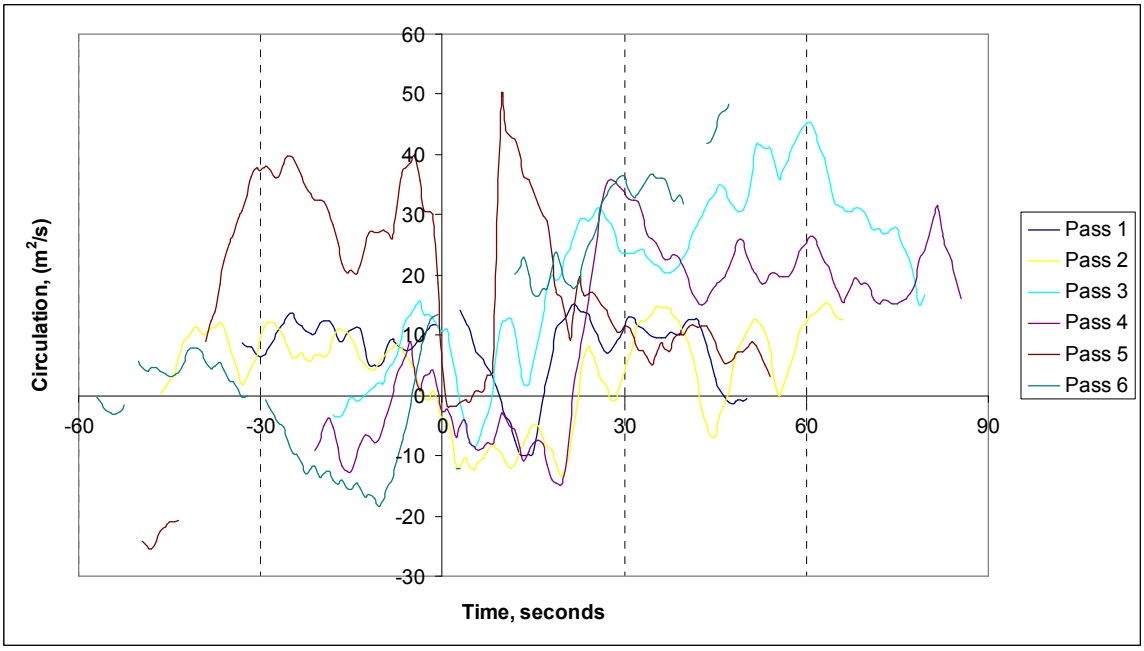

Figure 4.21 – Averaged Circulation vs. time for Trials 1-6 on 7-21-05 with cross wind

Ambient airport noise data were also obtained prior to aircraft or transducer operation. A Fast Fourier transform was used to convert data into the frequency spectrum, and is shown in Figure 4.22. It is observed that for our pulse transmission frequency of 57 kHz, there is no significant ambient noise level.

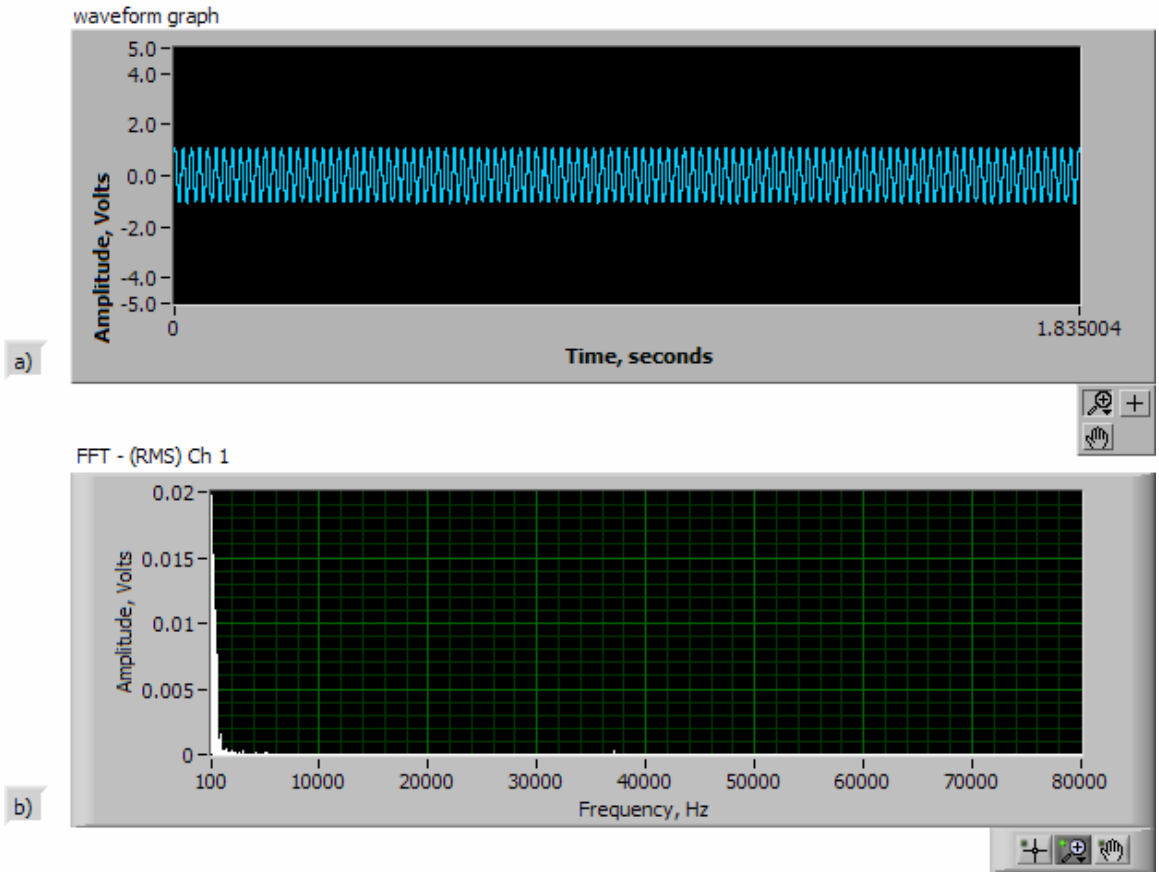

Figure 4.22 – Ambient noise waveform, amplitude vs. time in (a), and amplitude vs. frequency in (b), at Tanner-Hiller, 07-21-05, without air traffic

Ambient circulation data was also obtained throughout the day of data collection. Temperatures measured at Tanner-Hiller in the shade peaked at 90º F, and as can be observed from Figure 4.12 the solar heating generated surface convection, resulting in the formation of afternoon cumulus clouds. Figure 4.23 shows multiple plots of ambient circulations values collected, and labeled by the times of collection.

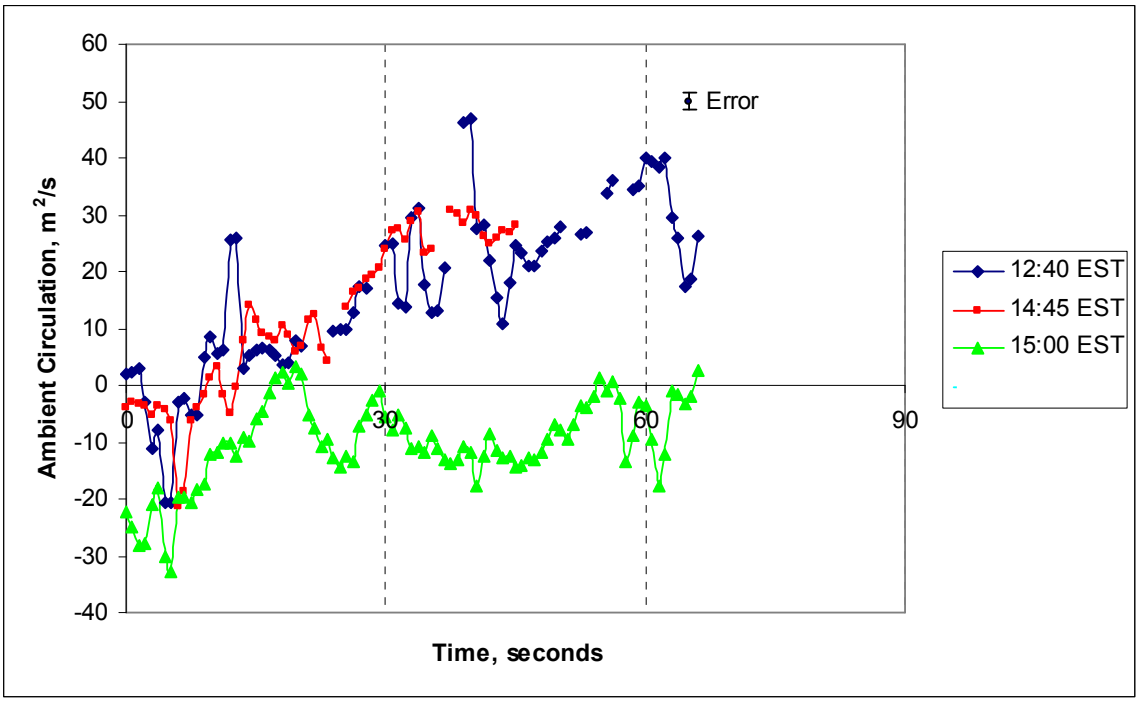

Figure 4.23 – Ambient circulation vs. time, 7-21-05, with cross wind

4.2.1 Analysis of Cross Wind Data

Adjustments were made to the raw delta-t and circulation values in order to achieve the results shown in section 4.2. Erroneous data due to aircraft noise pollution or undetectable signals were discarded. All graphs depicted in section 4.2 and Appendix II have been corrected using the following techniques.

After filtering techniques were applied, the aircraft noise remained at a high enough level to overwhelm the microphones for approximately one second as it passed by the measurement equipment. For these periods of time, where the signal could not be detected, the data point was removed from the data set. The microphone placement was also different, and thus the microphone placement error described in section 4.1.1 is not present in these later trials.

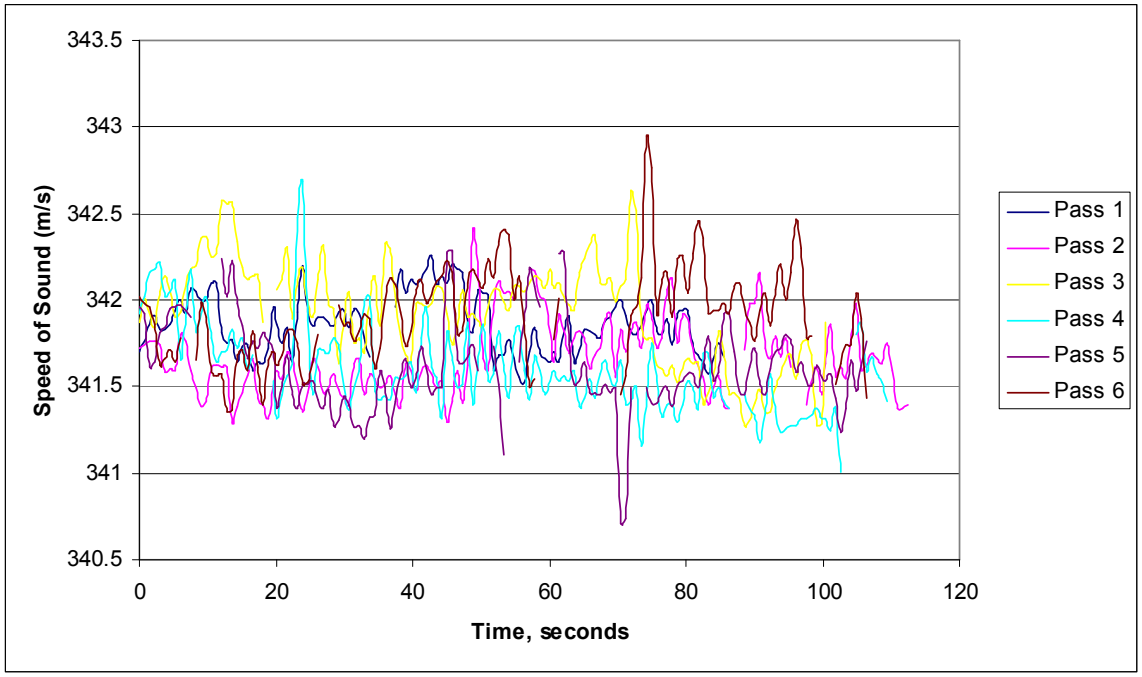

Figure 4.24 – Speed of sound fluctuations for trials 1-6, 7-21-05, with cross wind

Speed of sound data were also used as criteria for eliminating erroneous data points, as was discussed in section 4.1.1. Plots of the speed of sound as a function of time is shown in Figure 4.23. The variation is greater than what is observed from earlier trials, as is evident in the standard deviation measurements shown in Table 4.4, when compared with Table 4.2. This is indicative of a greater degree of error in measurements, which is expected given the ambient wind flow.

Table 4.4 – Statistics for Speed of Sound calculations for each trial, 7-21-05

	Speed of Sound	
Pass	**Average**	**Std. Deviation**
1	341.9	0.17
2	341.7	0.21
3	341.9	0.30
4	341.6	0.26
5	341.6	0.27
6	341.9	0.28

4.3 Aircraft Noise Data

During tests conducted with the Piper PA-32 test aircraft, it is observed that aircraft noise may overwhelm the ultrasonic pulse transmitted around the acoustic path. In some cases, the magnitude of aircraft noise results in an undetectable ultrasonic pulse for a period of up to 3 seconds following the aircraft passing the apparatus, even after filtering the signal. It is realized that a further understanding of the ultrasonic noise emissions from aircraft is needed in order to understand the operational capabilities of this technology.

Aircraft noise data were collected from the Manchester, New Hampshire Airport for a variety of commercial and cargo aircraft. This data were collected using the Bruel & Kjaer microphones, conditioning amplifier, data acquisition system and laptop, while sitting in a Manchester Airport operations vehicle approximately 300 feet from the centerline of the runway. Microphones were placed out the window of the vehicle, which was turned off, and pointed toward the aircraft as it traveled the runway.

Manchester Airport has two runways, both of which were being utilized during the period of data collection. The operations vehicle was able to move between the two runways to gather data, positioning 300 feet from centerline each time, and at a location along the runway where the largest aircraft would leave the ground during takeoff. In addition, ambient noise samples were taken when there was no active air traffic on the runways. Table 4.5 shows the aircraft for which noise data was gathered, assigns each flight a reference number, and details the time of day and runway used. Aircraft identification was provided by MHT operations staff.

Table 4.5 – Table of Aircraft Noise Data Collected from Manchester Airport

#	Aircraft	Runway	Time
01	Ambient airport noise (no planes)	35	05:38
02	Ambient airport noise (no planes)	35	06:41
03	Pilates – Departure	35	06:08
04	Pilates – Departure	35	06:15
05	Caravan – Departure	6	07:03
06	Caravan - Departure	6	07:05
07	Cessna – Departure	35	07:12
08	Saab – Departure	6	07:18
09	Pilates – Departure, & Airbus taxiing	35	06:37
10	Canadian Regional Jet – Departure	35	05:30
11	Canadian Regional Jet – Departure	35	06:48
12	MD-88 – Departure	35	06:46
13	B-737 – Departure	35	05:35
14	B-737 – Departure	35	06:46
15	B-737 – Departure	6	07:00
16	B-737 – Departure	6	07:06
17	B-737 – Departure	35	07:26
18	Airbus-319 – Departure (Prop. plane warming up)	35	06:05
19	Airbus – Departure	6	06:56
20	Airbus-321 – Departure	6	07:02
21	Airbus-300 series – Arrival (Prop. plane warming up)	35	06:10
22	Airbus-300 series – Arrival	35	06:35
23	DC-9 – Arrival	6	06:52

The data samples were collected, and then converted into multiple Lab View Measurement files using the programs in Appendix I. Half second segments of data were then analyzed using a Fast Fourier Transform (FFT) through Lab View to convert the data into the Frequency spectrum. From this frequency vs. amplitude plot, the ultrasonic

noise spectrum can be observed. In addition, the signal was filtered using a bandpass Butterworth filter, with upper and lower limits of 77 kHz and 37 kHz, respectively. This filtered signal gives a sense of what ultrasonic noise remains after applying the basic filtering techniques utilized with previous vortex measurements.

The data is displayed using the reference number found in Table 4.5. Below are data from three different types of aircraft, two during takeoff and one during landing, in figures 4.25-4.27. The remainder of the data can be found in Appendix III.

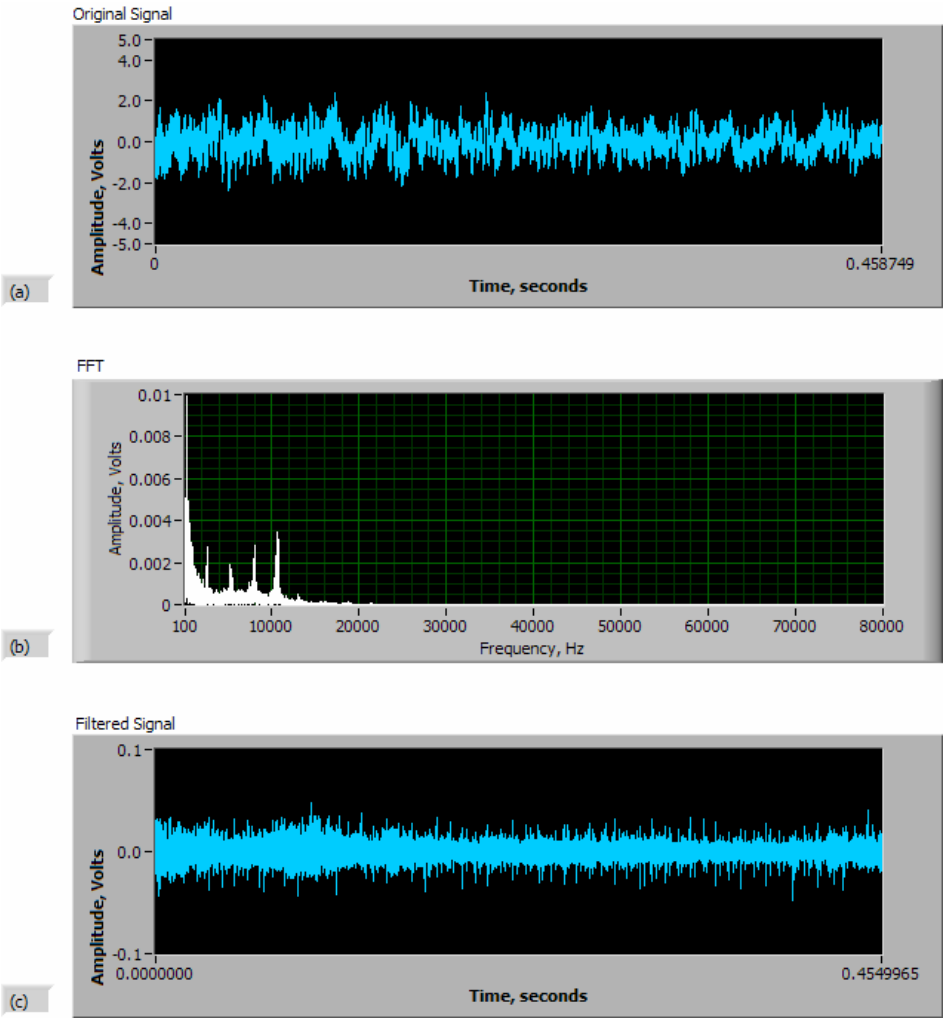

Figure 4.25 – MHT-10 aircraft noise amplitude vs. time in (a), and amplitude vs. frequency in (b), and filtered signal in (c)

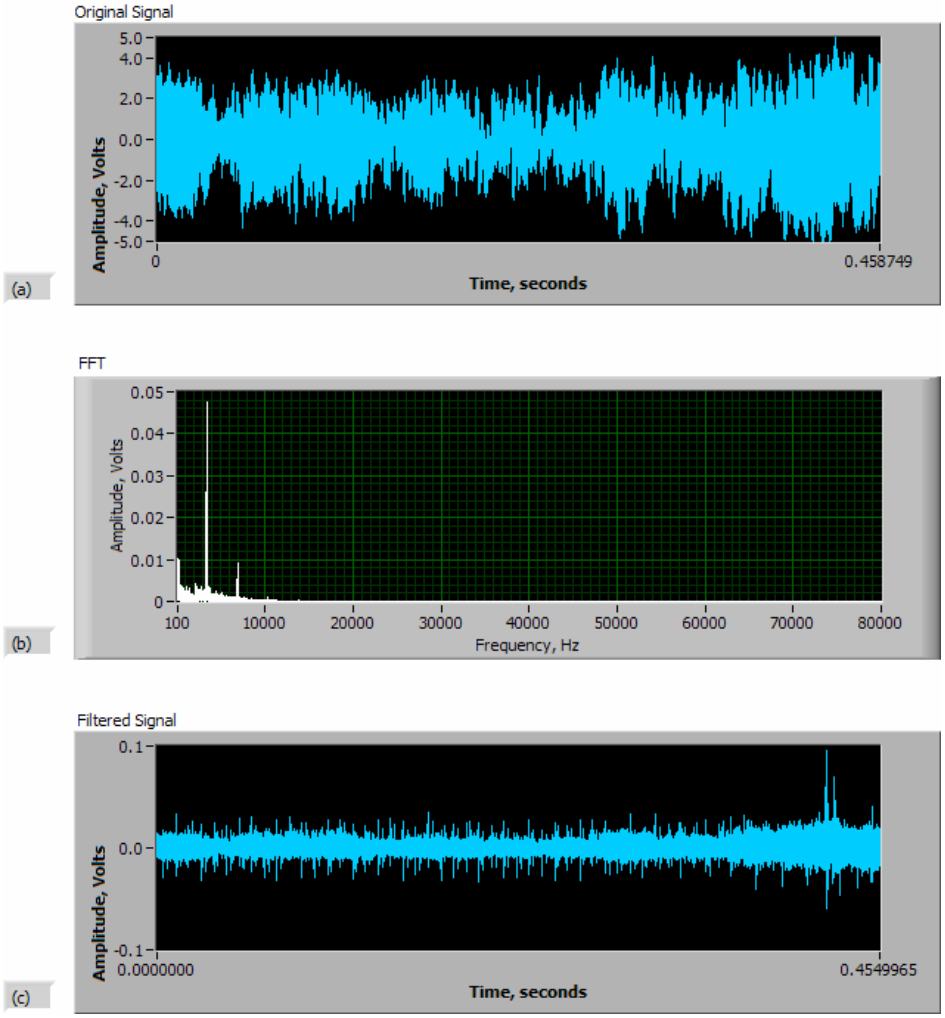

Figure 4.26 – MHT-13 aircraft noise amplitude vs. time in (a), and amplitude vs. frequency in (b), and filtered signal in (c)

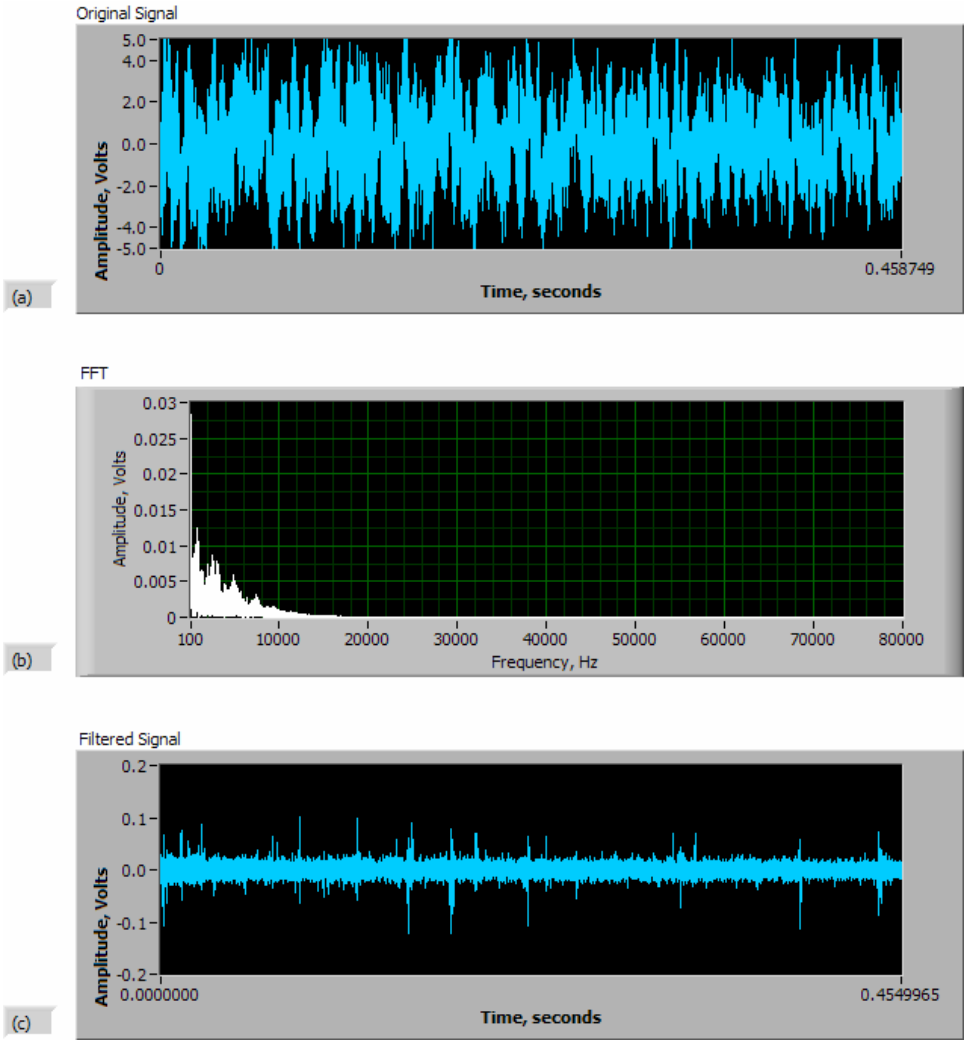

Figure 4.27 – MHT-22 aircraft noise amplitude vs. time in (a), and amplitude vs. frequency in (b), and filtered signal in (c)

5 Discussion

The multitude of data collected during various scenarios provided enormous evidence of the capability and operational limitations of this measurement technology. Initial testing proved the validity of the wake vortex detection concept, and the ability of the prototype equipment. Additional circulation measurements gathered while an ambient cross wind was present provided insight as to the effect ambient winds have on the measurement system. Removing the ground segment of the acoustic path raises additional questions about whether we can accurately discern the ambient circulations in the planetary boundary layer from the wake vortex circulations. In this chapter we examine these issues, and using the data gathered during field testing, we attempt to draw some conclusions about the capabilities of the measurement system.

5.1 Ideal Atmospheric Conditions

Multiple trials show very consistent results for circulation detection in ideal atmospheric conditions. For path A trials, an immediate maximum in circulation is observed after aircraft passes the measurement system, indicating the wake vortex is indeed shed immediately into the closed path. The circulation drops off at different rates for the first and second day of data collection, with circulation falling more rapidly during day one. The vortex decay is attributed to viscous effects, as well as lateral drift from runway which will result in vortex eventually drifting out of the closed path. In addition, circulation detected within the path will be affected by any secondary circulations generated due to ground proximity.

The shape of the day two path A circulation curves are as expected, with the maximum occurring instantaneously after the aircraft flew past, and declining steadily until it was no longer detectable. The path B circulation patterns show a slight difference in that the maximum circulation occurs approximately 10 seconds after the aircraft flew past, indicating that the center of the vortex had to travel downward and laterally to be completely within the observed closed path, signified by a maximum in circulation. However, it is interesting that the same signature is observed with the day one path A circulation curves, indicating that flight location on the day one trials may have been closer to path B than path A.

The path C circulation curves show a significantly greater amount of variation, and less defined peak circulation curves. In all instances, peak circulation occurred within the first 30 seconds, yet is delayed 10-20 seconds from the passing of the aircraft. Greater variability may be an indication that the vortex center was meandering at the closed path edge. In trial 11 there is no clearly defined peak circulation, which also corresponds to conditions of a slight breeze. The winds, when present, were oriented such that they would blow the vortices from the tower to the aircraft flight path. It is possible that in Trial 11 the vortex never completely entered the observation path because ambient winds, even thought they were light, kept it from drifting laterally into the closed path region.

It is important to note that the idealized wake circulation values we expect to observe are based on ideal flow regimes. The actual circulation measured is much more complex due to ground proximity, which induces movement and decay and causes the generation of secondary vorticity. Our measurements are affected by the movement of the vortex through our fixed space of observation. Given the shape of the observation

area, the vortices height above the surface could be a critical factor in the magnitude of circulation observed. If the vortex is traveling horizontally and is far enough from the surface, it will only be within our measurement path for a few meters. All of these complicating effects will lead to unexpected changes in our circulation values, and may be the cause of the variable data shown for path C trials.

The maximum circulation values observed in each trial correlate well with the expected circulation values, shown in Table 4.1. Observed circulation values are slightly higher than the expected circulation values, although the expected circulation calculations assume level flight, and do not take into account the induced drag on the wings and tail section, or the effect of flaps. Table 5.1 shows the maximum circulation detected for each trial based on the running average curve, compared with the theoretical circulation values calculated in table 4.1.

Table 5.1 – Comparison of maximum circulation values for all fourteen initial trials.

Trial	Maximum Circulation (m^2/s)	Theoretical Circulation Calculated (m^2/s)
1	33.8	31.4
2	36.3	32.4
3	33.4	31.4
4	26.6	31.4
5	26.3	31.4
6	41.5	27.6
7	35.0	30.1
8	42.5	28.3
9	21.6	28.3
10	20.7	28.3
11	13.6	29.2
12	39.1	33.1
13	33.4	31.0
14	45.5	31.0
Average	32.1	30.4

The rate of decay also appears to be very consistent between trials. There does seem to be a variation in observed circulation decay rates from day one to day two, but within a given day the decay is very similar. This decline in circulation is more than simply the viscous decay of the vortex, as noted previously. For this reason, direct comparison to previous research on vortex decay is not appropriate. However, in a qualitative sense we can discuss these results and compare them with previous studies.

Prior research by Sarpkaya (1998) examined the decay of wake vortices as a function of time, and noted the rate of decay is non-liner with time. The decay observed in these trials is also non-linear in nature. Sarpkaya observed vortices from large aircraft (DC-10 and B-757) using a LIDAR system, and therefore was able to track the vortices through space and monitor their decay regardless of any movement or secondary circulation generation. In the Sarpkaya study, data show vortex strength was observed to be 25% of initial strength anywhere from 75-160 seconds from vortex generation.

The vortices produced by a DC-10 or B-767 aircraft are at least one order of magnitude greater than what is produced from the small Piper aircraft. In addition, the segmented or elliptical shape of the large aircraft wings result in different aerodynamic formation of the wake vortices than is occurring off the rectangular Piper wing. In this study, it took approximately 20 seconds for the vortex to reach 25% of original strength. It is expected that the decay rate would be significantly greater for these smaller vortices than was observed in the Sarpkaya study.

5.2 Cross Wind Conditions

At first glance the circulation measured during conditions of ambient cross wind does not appear nearly as valuable as the clean data gathered under ideal atmospheric conditions. However, this round of trials provided substantial amounts of information about the capability and limitations of this measurement equipment.

Looking at the circulation plots, it can be seen that the ambient circulation values are ten times greater than what was observed in the data taken with no ambient wind flow. In fact, the ambient circulations are of the same order of magnitude as the wake vortices which we were attempting to measure. Due to this poor signal to noise ratio, the vortices are difficult to discern for many of the trials. A case can be made that the first vortex (expected to have a negative circulation) is seen in the measurement area. In all six cases the circulation values drop to zero or below, and the trend is particularly evident in Figure 4.21 where all plots are collapsed onto one graph.

It is not discernable whether the second vortex is ever detected by the measurement system or not. In most cases, circulation values rise considerably following the initial decrease. However, that rise could just as likely be due to ambient circulation fluctuations as the second wake vortex entering the path. It is clear that vortices of this strength can easily get lost in ambient circulations caused by atmospheric conditions.

However, numerous advantages were realized with this new experimental setup. First, the microphone signal strength microphone enabled all gain settings on data acquisition system and conditioning amplifier to be zero. Secondly, the signal clarity observed in both microphones was greatly improved from the previous round of trials. This resulted in better cross correlation results, and more distinct Hilbert envelope

functions, and overall less data points were thrown out. All of these advantages to signal clarity were observed despite the fact that the meteorological conditions resulted in greater attenuations of signal. There were also variable winds which did not appear to negatively impact the equipment or tower. In addition, the microphones were not as overwhelmed with aircraft noise when the test plane flew by. In most cases just one or two data points were lost, instead of the five or six with the previous configuration.

The ambient circulations certainly must be understood in order to anticipate the sensitivity of this measurement system in various wind flow conditions. These trials differed from the previous set because there was ambient wind flow, and with a no slip condition invoked at the surface, there is wind shear within the measurement area. The wind shear of the planetary boundary layer contains vorticity, which is being measured by the equipment.

The planetary boundary layer is composed of three layers: the molecular layer, the surface layer, and the mixed layer. The molecular layer is dominated by viscous forces, and extends only a few millimeters above the surface. The surface layer is dominated by wind shear, which increases logarithmically with height, and extends approximately 40 meters above the surface. The mixed layer contains little wind shear, and can extend up to 1 kilometer above the surface. The top of the mixed layer contains geostrophic wind flow which indicates the end of the planetary boundary layer (Holton, 1992; Wallace and Hobbs, 1977).

These layers of the PBL can vary with synoptic scale weather systems and surface topography and roughness. However, it is apparent that our measurements are conducted primarily in the surface layer in the presence of wind shear. Given that the area over

which we are measuring circulation varies with height (a greater portion of the triangular shaped area is closer to the surface than at the top of the tower), it is important to understand the distribution of vorticity as a function of height in the surface layer. By applying Green's Theorem to equation 2.1, circulation can be defined by Equation 4.3, where ω is vorticity oriented orthogonal to the measurement area (Kreyszig, 1999).

$$\Gamma = \iint_A (\omega) dA \tag{4.3}$$

In theory, knowing the gradient of vorticity with height and our defined measurement area, we can use equation 4.3 to calculate the ambient circulation due to the wind shear of the PBL. However, knowing that wind speed is logarithmic with height is not of general practical use because that is an averaged, idealized wind shear relationship. In actuality, there are turbulent eddies present in the PBL, which disrupts the typical wind distribution with height. In addition, surface heating generates convective plumes and turbulent eddies, which also change the structure of the wind field in the surface layer (Holton, 1992; Wallace and Hobbs, 1977). Attempting to discriminate what component of circulation observed by the measurement device is a result of a trailing vortex or PBL wind shear at a given instant in time can prove very difficult.

While calculating an exact instantaneous measurement of PBL circulation for a specific area is nearly impossible, it is believed that a reasonable estimate could be obtained. By placing an anemometer at the top of the tower, we could observe the wind direction and speed, and calculate the component of the wind that is parallel with our measurement area.

An example calculation can be made to estimate the ambient circulations present during the cross wind trials shown in section 4.2. Lowest wind speeds were observed to

be 5 knots, which corresponds to approximately 2.5 m/s. As a first estimate, we can assume the vertical wind shear is constant within the 9 meter height of the acoustic path. Assuming constant wind shear and no vertical wind flow, vorticity is simplified, equation 4.4, with horizontal and vertical directions represented with x and y, respectively.

$$\omega \equiv \frac{\partial v}{\partial x} - \frac{\partial u}{\partial y} \approx \frac{\partial u}{\partial y} \tag{4.4}$$

This yields a constant vorticity value for the entire measurement area of 0.28 s^{-1}. Our measurement area is approximately 90 m^2, which results in an ambient circulation value of 25.2 m^2/s. Similarly, with the highest wind speeds observed at 10 knots, or 5m/s, the resulting ambient circulation, based on a linear shear profile with height, would be 50 m^2/s. Therefore, using these simplifications, we would expect ambient circulation to vary between 25 and 50 m^2/s assuming wind speeds were maintained between 5 and 10 knots. Large commercial aircraft are observed to have vortices with initial strength of 300-500 and

Having instantaneous wind data from an anemometer at the top of the tower would provide us with a method for accounting for some of these ambient circulations, and possibly discriminating between these circulations and those produced by a wake vortex. Of course, turbulent fluctuations will ensure the vorticity profile with height is never constantly uniform, however initial calculations show it can provide a good estimate of in-situ calculations. With a responsive anemometer that provides data at the same time resolution as our measurement system (1.33 Hz), we can observe temporal changes in ambient circulations simultaneously with circulation measurements. When

considering measuring vortices from large aircraft with initial strengths of 300-500 m^2/s (Sarpkaya, 1998), the ambient circulation fluctuations of 25-50 m^2/s can be neglected.

5.3 Aircraft Noise

A large sampling of aircraft noise emission data is shown in section 4.3 and Appendix III. From these data it is observed that the majority of aircraft noise emissions are in the low audible frequency range. Filtering the signal using a bandpass filter with limits of 37 kHz and 77 kHz reveals there is still noise detected in the ultrasonic frequency range.

In determining whether this ultrasonic aircraft noise emission will affect the measurement system, a comparison must be made between these noise emission levels and our ultrasonic pulse we detect when making circulation measurements. The frequency spectrum plot of aircraft noise gives an overall sense of the distribution of frequencies within the noise sample, but it is graph (c) of Figures 4.25-4.27 and Appendix III that provides the best sample for comparison.

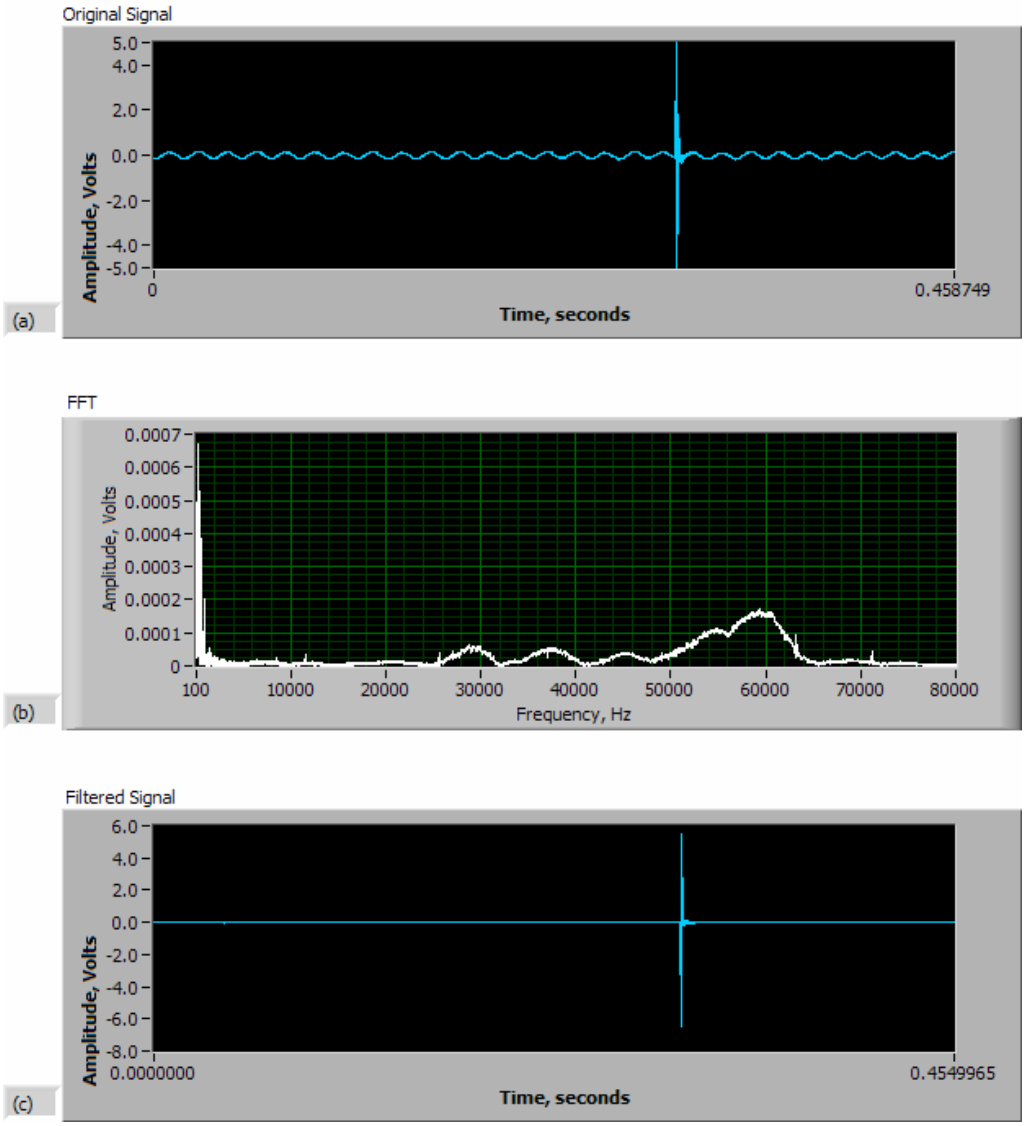

Figure 5.1 – Transmitted acoustic pulse before traveling acoustic path, amplitude vs. time in (a), and amplitude vs. frequency in (b), and filtered signal in (c)

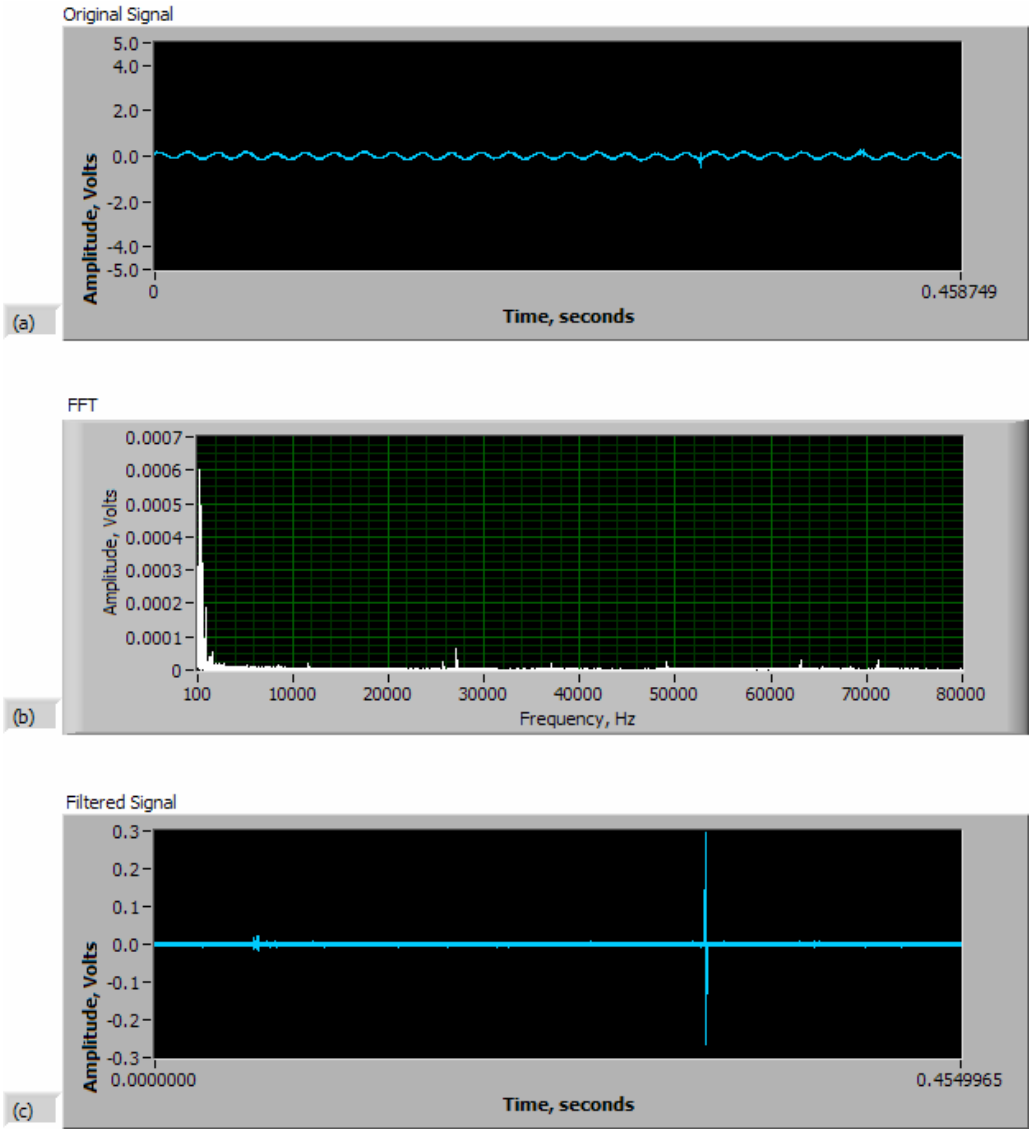

Figure 5.2 – Transmitted acoustic pulse after traveling acoustic path, amplitude vs. time in (a), and amplitude vs. frequency in (b), and filtered signal in (c)

The 57 kHz ultrasonic pulses transmitted must be detected immediately after leaving the transducer, and then again once they have traveled the acoustic path. Samples of these ultrasonic pulses, both before and after traveling the acoustic path, are shown in Figures 5.1-5.2. It is seen that the acoustic pulse contains significant amplitude before traveling the acoustic path, approximately 5 volts, and much less amplitude after traveling the acoustic path, approximately 0.3 volts. Comparing these noise levels of the

filtered signals to that of the aircraft noise emissions after filtering, it is clear that the initial detection of the acoustic pulse will be unaffected by the aircraft noise.

The second detection of the acoustic signal, shown in Figure 5.2, can be compared with the values of ultrasonic noise emissions of various aircraft. Aircraft noise emission are observed to have average amplitudes of approximately 0.05 volts, with maximums around .1 or .2 volts. Our acoustic pulse has a larger amplitude, even after traversing its path. It is possible that the signal could be undetectable for one or two pulse transmissions, but the levels of noise do not indicate that ultrasonic aircraft emissions will be a hindrance to this measurement system.

Microphone placement of an operational system will be in the vicinity of 300 feet from the runway centerline, the distance at which these measurements were taken. We can expect noise emission levels to vary based on atmospheric variables, aircraft type, and take-offs vs. landings. However, all indications from the data set collected are that the ultrasonic noise emissions from aircraft are extremely low, and will not pose a significant problem to this measurement system.

6 Conclusions

The data gathered in this study validates this technology as a viable means of wake vortex detection. The ultrasonic measurement technology is able to detect the direction and magnitude of the vortex generated at one wing tip of the test aircraft during low-pass flights. Although this study proved this concept, there is still additional work that needs to be completed to validate that this is a practical and effective method of wake vortex detection in a large airport environment during a range of meteorological conditions.

The results of the study clearly show that this measurement technology is able to detect the presence of wake circulation produced by aircraft in ideal meteorological conditions. In almost all initial trials, an immediate spike in circulation was detected that was well above all ambient fluctuations and therefore is definitively from the passing aircraft's wake vortex. The magnitude of the circulation detected is in general agreement with the predicted values based on the modified Kutta-Joukowski theorem.

The vortex signature observed in the trials is distinct and unique as well. The circulation peaks and rate of decay follow the same pattern for similar flight paths within a single day. In light of this fact, automatic algorithms could be developed to detect in a true/false manner the presence of a specific wake circulation within the acoustic path. Consistency of the observed signatures also indicates that the technology is highly reliable, albeit for a very small data set. The vortices detected in this study are much smaller than dangerous wake circulations produced by large commercial aircraft. Given the accuracy and clarity of detecting these weaker circulations, it is very likely that the technology will prove to be highly reliable for detecting stronger wake circulations.

In conditions of ambient winds, specifically a cross wind, natural variations of circulation can be an order of magnitude greater than in conditions of no wind. The magnitude of these in-situ circulations are equal to the magnitude of the wake vortices produced by the Piper aircraft. Therefore it is obvious that clear detection of the presence of a wake vortex of that size is not practical with a cross wind present.

Greater variability is observed in the circulation and speed of sound measurements when a cross wind is present. Due to fluctuations in winds on the same time scale as signal interval frequency, the flow field may change between transmission of pulses in opposite directions, thus resulting in inaccurate speed of sound information for that pulse pair. Decreasing the interval frequency, currently 1.33 Hz, would alleviate some of that variability when ambient wind fluctuations are great.

In summary, the data detailed in this thesis supports the following conclusions:

1) Measurement system is able to detect the magnitude and direction of wake vortex circulations.
2) Multiple trials reveal similar vortex circulation plots, indicating automatic algorithm development for the presence of wake vortices is possible.
3) Cross winds generate vorticity within the planetary boundary layer that are detected by measurement system.
4) Ambient circulations are predictable to some extent by knowing surface wind speed and direction information.
5) Eliminating the ground segment of the acoustic path results in better signal quality and cross correlation results, less data corrections, and fewer lost data points.

6) There is no significant ultrasonic noise detectable 300 feet from runway centerline from the aircraft sampled at Manchester Airport.

6.1 Considerations for Operational Use of Technology

The experimental setup used in this experiment is clearly not viable as a means of vortex detection at an airport with regular commercial air travel. The experiment was setup to prove the validity of the measurement technology, and the proximity of the tower to the passing aircraft is clearly not safe for regular airport use. The Johari and Durgin patent (2000) depicts various configurations that would be viable for use at an airport runway. Figure 6.1 shows one of these configurations at a single runway airport. Based on information gathered from the present field trail, this would be one of the most practical methods for effective detection at a runway while maximizing safety and minimizing interruption of normal airfield activities.

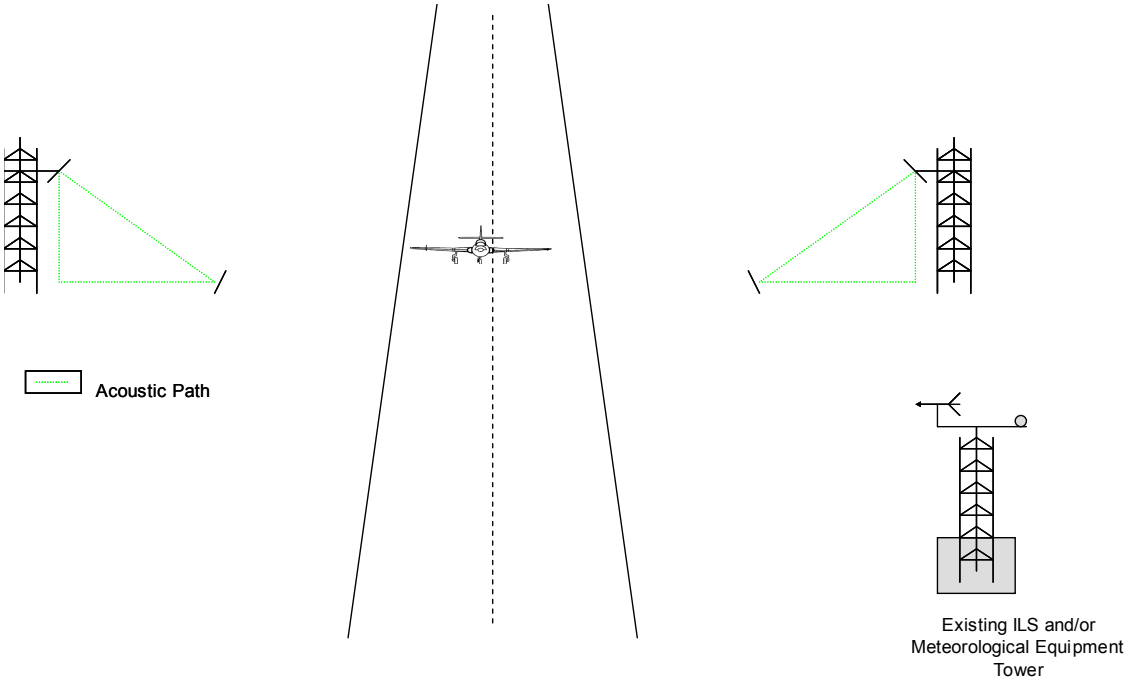

Figure 6.1 – Example of possible operational setup at a large airport.

In the configuration in Figure 6.1 there are two measurement systems set up symmetrically at a runway. The towers would have to be far enough from the runway so as not to pose a safety hazard. A guideline used in this schematic is to have the towers the same distance away as the Instrument Landing System (ILS) towers. The system would ideally be at a point along the runway before the expected point where aircraft touch down, or after lift off, where wake circulations are greatest.

The wake circulations generated by the Piper were nearly undetectable within the ambient circulations in the cross wind scenario. However, the wake circulations generated by the Piper are not at a dangerous level, and therefore there is no need for a measurement system to have the sensitivity to detect circulations of this magnitude. The dangerous circulations generated from large aircraft are an order of magnitude greater than the Piper circulations, 300-500 m^2/s (Sarpkaya, 1998), and it is expected that these circulations will be detectable above ambient circulation levels.

Aircraft noise emission data from Manchester Airport reveals that there is very little ultrasonic noise emission from many types of aircraft at 300 feet from runway centerline. If this holds true for all aircraft not sampled in this data set, then operationally this system would be able to be utilized with all types of aircraft. At an operational distance equal to the ILS towers, which is 300 feet from runway centerline at MHT, there is no ultrasonic noise emission at a level that would interfere with system operation.

The measurement system proved to be very robust during field trials. All equipment operated very well in an outdoor environment, where ambient noise, wind, and temperatures are not always ideal. Although field trials occurred during ideal conditions, often preliminary testing and setup occurred in non-ideal conditions.

Equipment packaging issues need to be addressed to utilize the system in precipitation, but preliminary assessment indicates overall system robustness appears compatible with continuous outdoor use.

6.2 Future Work

While the results of initial testing were successful, a considerable amount of further work is required if this technology is going to be pursued as a solution to the wake vortex problem. The current study has tested the technology under idealized meteorological conditions and with a cross wind, and only utilized a single test aircraft with one general operational configuration. Considerable investigation must occur to fully understand the capability of this technology, and only then can it be evaluated as a tool for implementation at airports with the operational capability of active runway management by airport officials. This technology shows a lot of promise, but the overall investigation is still young.

Further field work with the prototype is needed to determine the ability of this technology in a variety of conditions and with a variety of aircraft. It is recommended that rigorous field testing occur with all types of aircraft, particularly larger aircraft that produce the most intense trailing vortices. These field tests also need to occur in all meteorological conditions. It is expected that varying meteorological conditions will affect the signal transmission attenuation, performance of equipment, and ambient circulation values.

In addition, a large data set will be needed to determine the reliability and capability of this technology as a tool for reducing spacing distances. The Federal Aviation Administration has set forth the minimum aircraft spacing policy in order to

maintain the highest level of safety for air travel. Any technology that will result in a change to this federal policy needs to be proven highly reliable with considerable supportive data.

Future testing will enable a comparison of wake vortex measurements from large aircraft to prior studies that utilized different technology. Accuracy and performance comparison will aid in development of this prototype. In addition, this technology can be utilized to study the behavior and movement of wake vortices, particularly their interaction with the ground. Ground interaction phenomena of wake vortices has been studied and modeled, yet very little experimental data exists to validate the theory. This technology can also be utilized for measuring and further understanding wake vortices produced by helicopters.

In considering this technology for operational use at airports, further development is needed in many areas. A computer programs that performs data sampling and instantaneous analysis is needed, with automated algorithms to detect the vortex presence within the path. Configurations of the system along the runway, distance from the runway, and positioning in cross-runway layouts will all need to be investigated as well. It is anticipated that use of multiple setups for a single runway could allow the ability to detect the speed and direction of vortex line movement. For operational use, a user-interface must be considered to display data from sensors in the most effective manner possible. Data need to be available rapidly for immediate decision making on the air traffic controllers part in order for this system to be practical.

Bibliography

Anderson, J. D., *Fundamentals of Aerodynamics*, McGraw-Hill, New York, 1984.

Andrade, M., and Messina, A. R., "Application of Hilbert Techniques to the Study of Subsynchronous Oscillations," International Conference of Power Systems Transients, Tech Report IPST05_172, 2005.

Baart, D., Rovinsky, R., Monk, H., and Schweiker, M., "Effect of Reduced Intrail Separations on Capacity," Volpe National Transportation Systems Center, Report DOT-VNTSC-FAA-92-7.1, Cambridge, MA, Oct. 1991.

Brown, C. E., "Aerodynamics of Wake Vortices," AIAA Journal, Vol. 11, 1973, pp. 531-536.

Burnham and Hallock, "Measurments of Wake Vortices Interacting With the Ground," AIAA-1998-593, Aerospace Sciences and Meeting Exhibit, Reno, NV, Jan. 1998.

Boluriaan, S., and Morris, P., "Numerical Simulation of Wake Vortex Detection Using a Radio Acoustic Sounding System," AIAA, Vol.39, 2001, pp.1097-1105.

Corjon, A., and Poinsot, T., "Wake Vortices Behavior Near Ground," ESAIM: Proceedings, Vol. 1, 1996, pp.279-294.

Desabrais, K.J., "Direct Measurement of Wing Tip Vortex Circulation Using Ultrasound," M.S. Thesis, Worcester Polytechnic Institute, Worcester, MA, 1997.

Desabrais, K. J., and Johari H., "Direct Circulation Measurement of a Tip Vortex," AIAA Journal, Vol. 38, 2000, pp. 2189-2192.

Federal Aviation Administration, "Aeronautical Information Manual," FAA, Washington, DC, 2004.

Flight Safety Technologies, "Socrates Wake Vortex Detection and Tracking: A Status Report" November 2004.

Fox, R. W. and McDonald, A.T., *Introduction to Fluid Mechanics*, Wiley, New York, 1985.

Fresch, M., and Zinner, T., "Concept of Wake Vortex Behavior Class," Journal of Aircraft, Vol. 41, 2004, pp. 564-570.

Gerz, T., and F. Holzapfel, "Wing-Tip Vortices, Turbulence, and the Distribution of Emissions," AIAA Journal, Vol. 37, 1999, pp. 1270-1276.

Hamilton, D. W., and Proctor F.H., "Wake Vortex Transport in Proximity to the Ground," 16th Digital Avionics Systems Conference, Philadelphia, PA, October 2000.

Hinton, D. A., "Description of Selected Algorithms and Implementation Details of a Concept-Demonstration Aircraft Vortex Spacing System," NASA TM211027, 2001.

Hinton, D. A., et. al. "NASA Aircraft Vortex Spacing System Development Status," AIAA 99-0753, 37th Aerospace Sciences Meeting, Reno, NV, 1999.

Holton, J. R., *An Introduction to Dynamic Meteorology*, Academic Press, New York, 1992.

Holzapfel, F., Gerz,T., Fresch, M., and Dornbrack, A., "Wake Vortices in Convective Boundary Layer and Their Influence on Following Aircraft," Journal of Aircraft, Vol. 37, 2000, pp. 1001-1007.

Johari, H., and Durgin, W. W., "Direct Measurement of circulation using ultrasound," Experiments in Fluids, Vol. 25, 1998, pp. 445-454.

Johari, H. and Durgin, W. W., "Ultrasonic Monitoring Method and System for Wake Turbulence Useful at Runways," US Patent # 6062076, 2000.

Kreyszig, E., *Advanced Engineering Mathematics*, Wiley, New York, 1999.

Long, S., Huang, N., Tung, C., Wu, R., Mollo-Christensen, E., and Juan, Y., "The Hilbert Techniques: An Alternate Approach For Non-Steady Time Series Analysis," IEEE-GRS-S Newsletter, 1992, pp. 6-11.

O'Conner, C. and Rutishauser, D., "Enhanced Airport Capacity Through Safe, Dynamic Reductions in Aircraft Separation: NASA's Aircraft Vortex Spacing System," NASA Langley Research Center, Report, NASA TM-211052, Hampton, Virginia, 2001.

Ozger, E., Schell, I., and Jacob, D., "On the Structure and Attenuation of an Aircraft Wake," Journal of Aircraft, Vol. 38, 2001, pp. 878-887.

Panton, R. L., *Incompressible Flow*, Wiley, New York, 1996.

Rubin, W., Burnham, D., Spitzer, E., and Rudis, R., "Robust Low Cost Airport Wake Vortex Sensor," Journal of Aircraft, Vol. 37, 2000, pp. 377-382.

Rudis, Wang, and Daskalakis, "Status Report Socrates Concept Exploration Effort", Volpe Report, October 2001.

Rutishauser, D. et. al, "Wake Vortex Advisory System (WakeVAS) Concept of Operations, NASA paper, April 2003.

Sarpkaya, T., “Decay of Wake Vortices of Large Aircraft,” AIAA, Vol. 36, 1998, pp. 1671-1679.

Schevell, R. S., *Fundamentals of Flight*, Prentice Hall, New Jersey, 1989.

Schmidt, D. W., “Acoustical Method for Fast Detection and Measurement of Vortices in Wind Tunnels,” ICIASF Record, 1975, pp. 216-228.

Shariff, K. and A. Wray, “Analysis of the Radar Reflectivity of Aircraft Vortex Wakes,” Journal of Fluid Mechanics, Vol. 463, 2002, pp. 121-161.

Wallace, J. M. and Hobbs, P. V., *Atmospheric Science*, Academic Press, New York, 1977.

Appendix I

Lab View program for data collection, front panel and block diagram. (Program adapted from Lab View example, 'Cont Acq to File.vi')

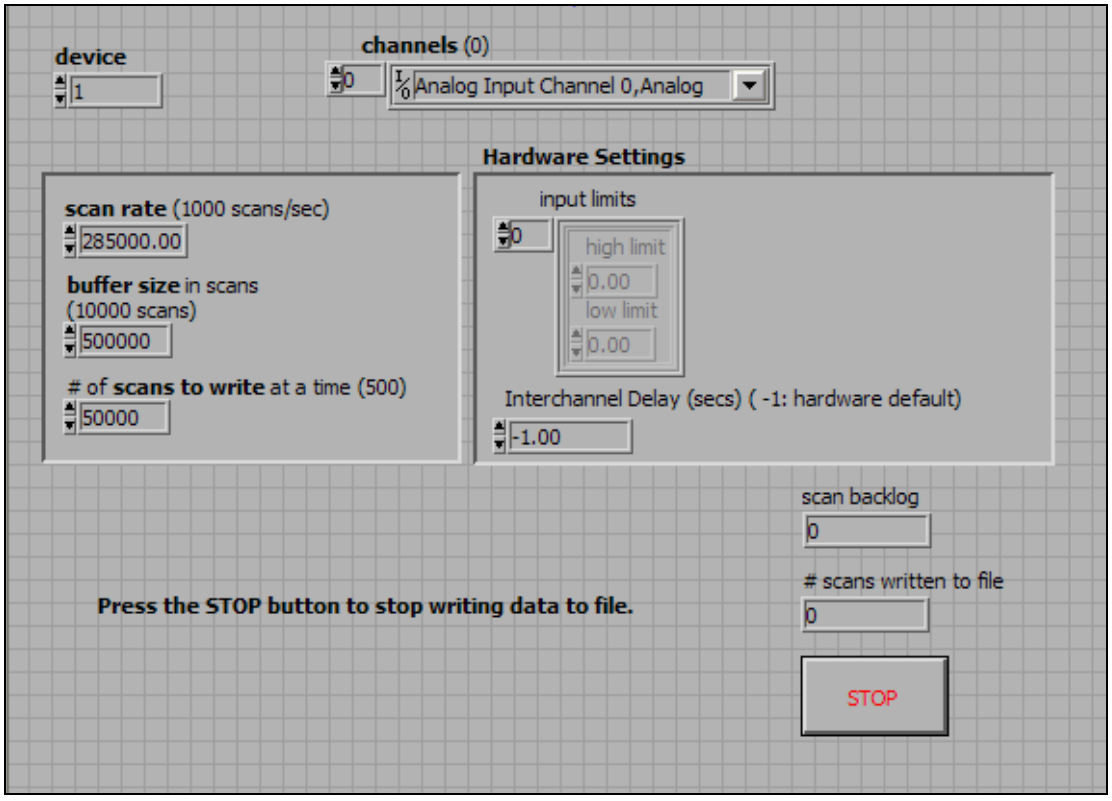

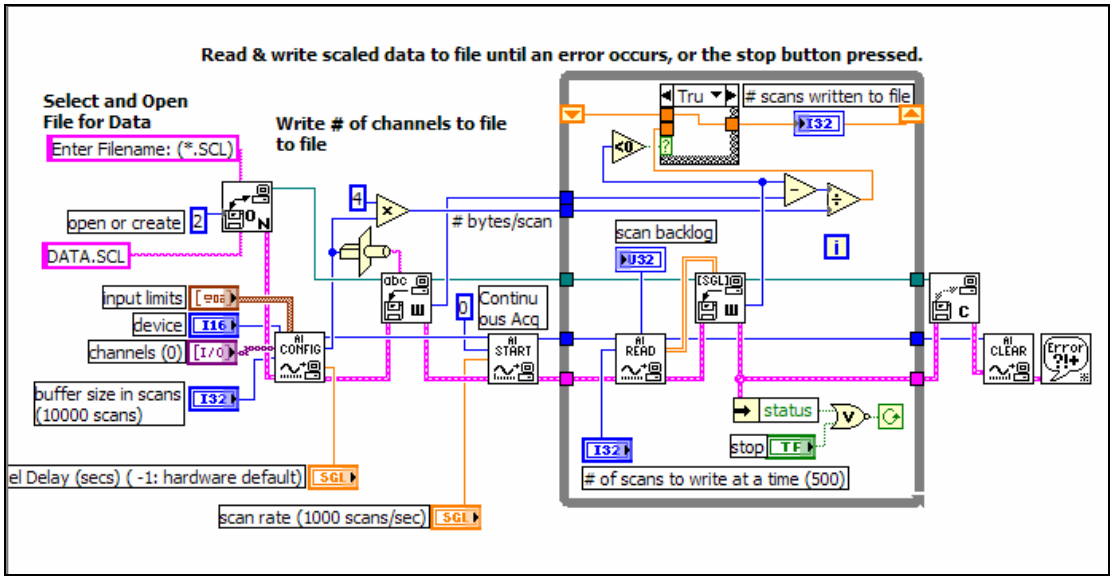

Lab View program for converting into multiple .lvm files, front panel and block diagram.

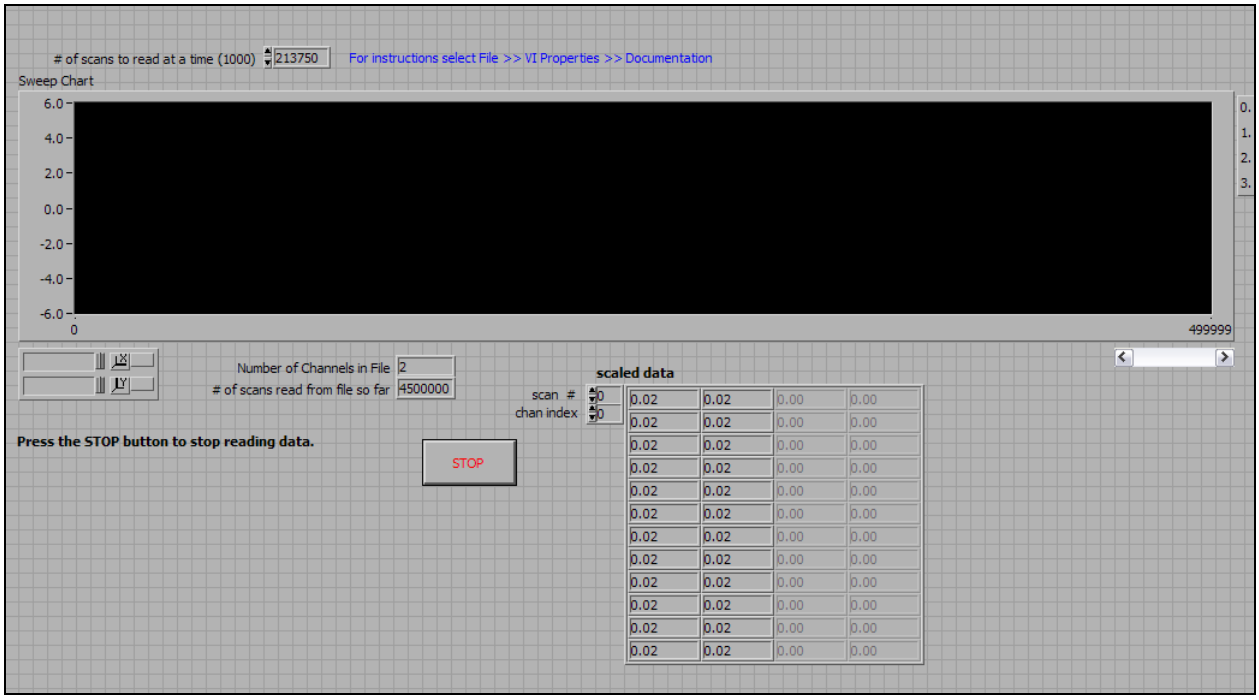

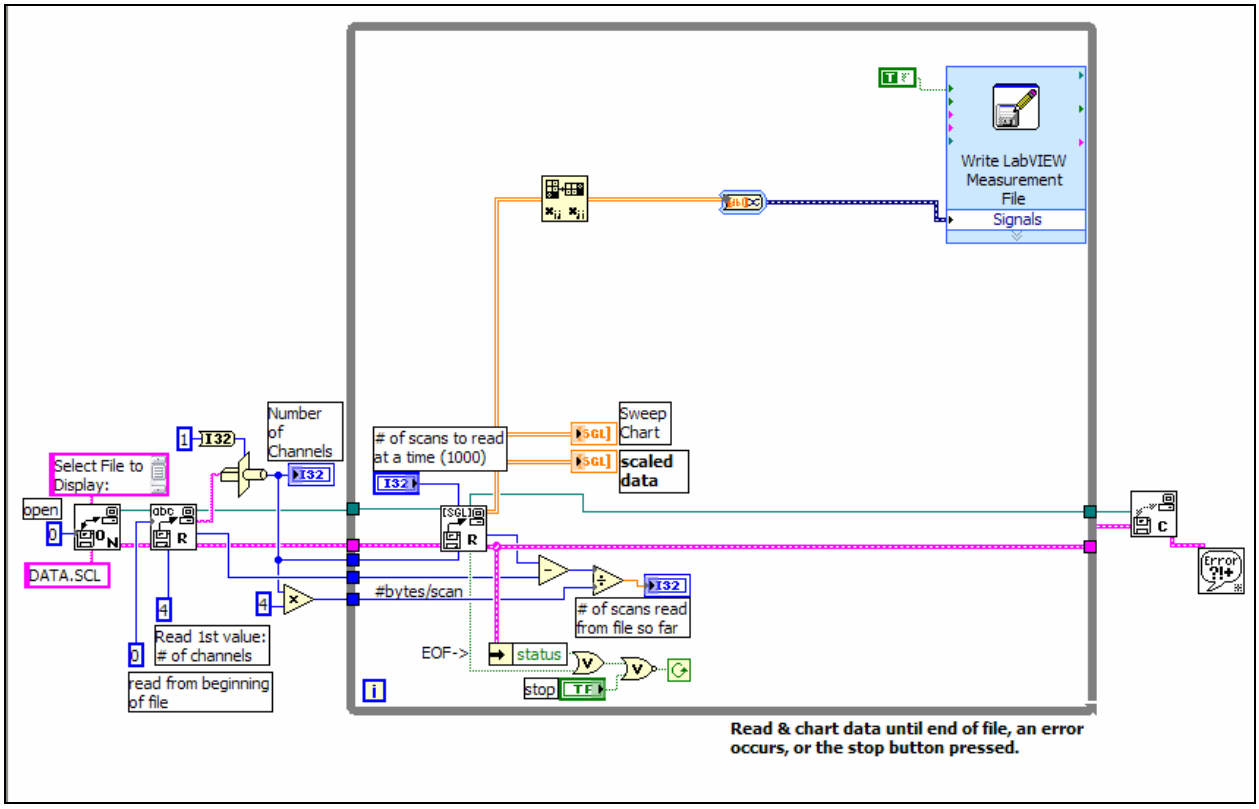

Lab View program for data analysis, closed acoustic path, front panel and block diagram.

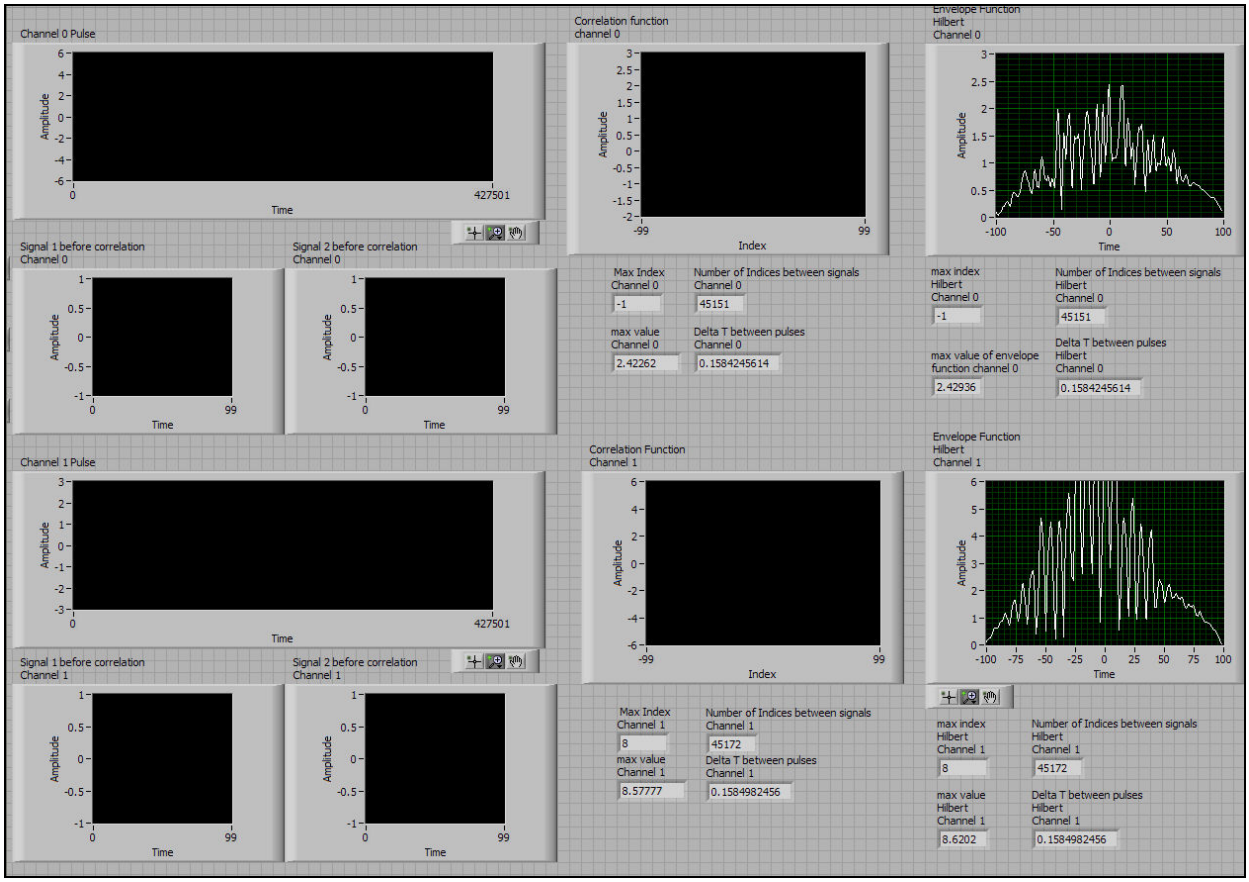

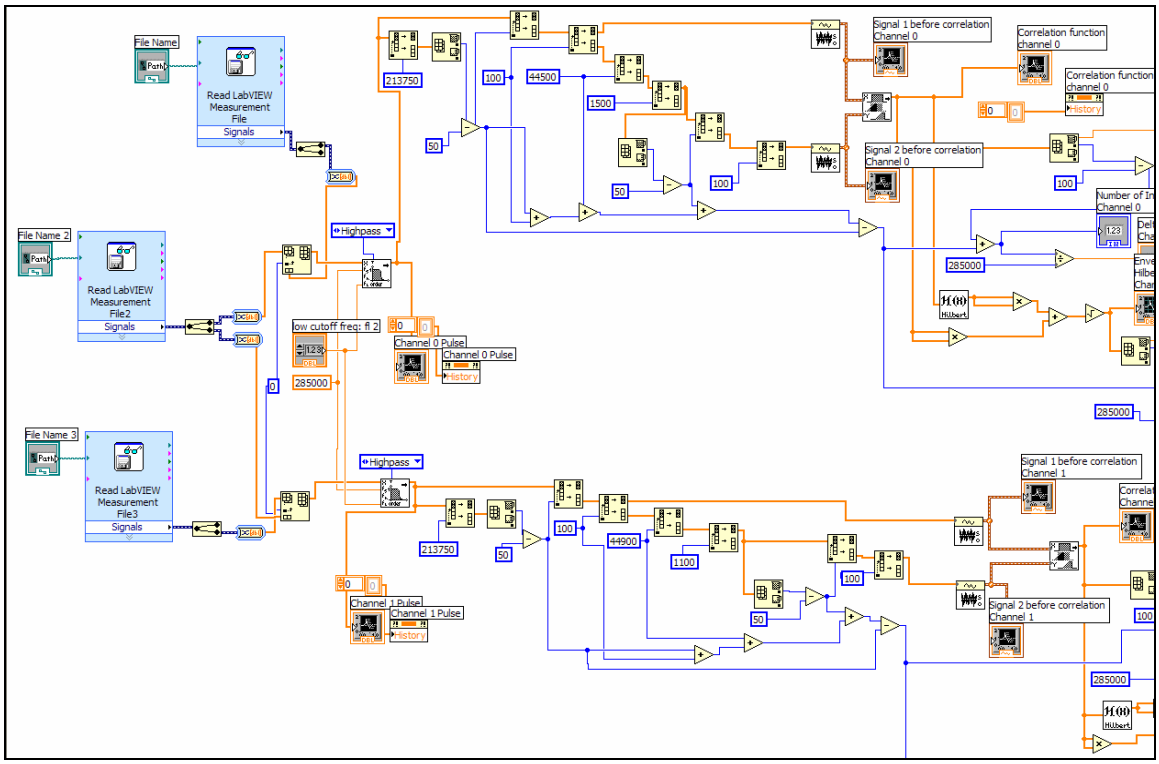
File Name
Read LabVIEW Measurement File
Signals
File Name 2
Read LabVIEW Measurement File2
Signals
File Name 3
Read LabVIEW Measurement File3
Signals
Highpass
Highpass
low cutoff freq: fl 2
Channel 0 Pulse
Channel 0 Pulse
Channel 1 Pulse
Channel 1 Pulse
Signal 1 before correlation Channel 0
Correlation function channel 0
Correlation function channel 0
Signal 2 before correlation Channel 0
Signal 1 before correlation Channel 1
Signal 2 before correlation Channel 1
213750
100
44500
1500
50
285000
44900
1100

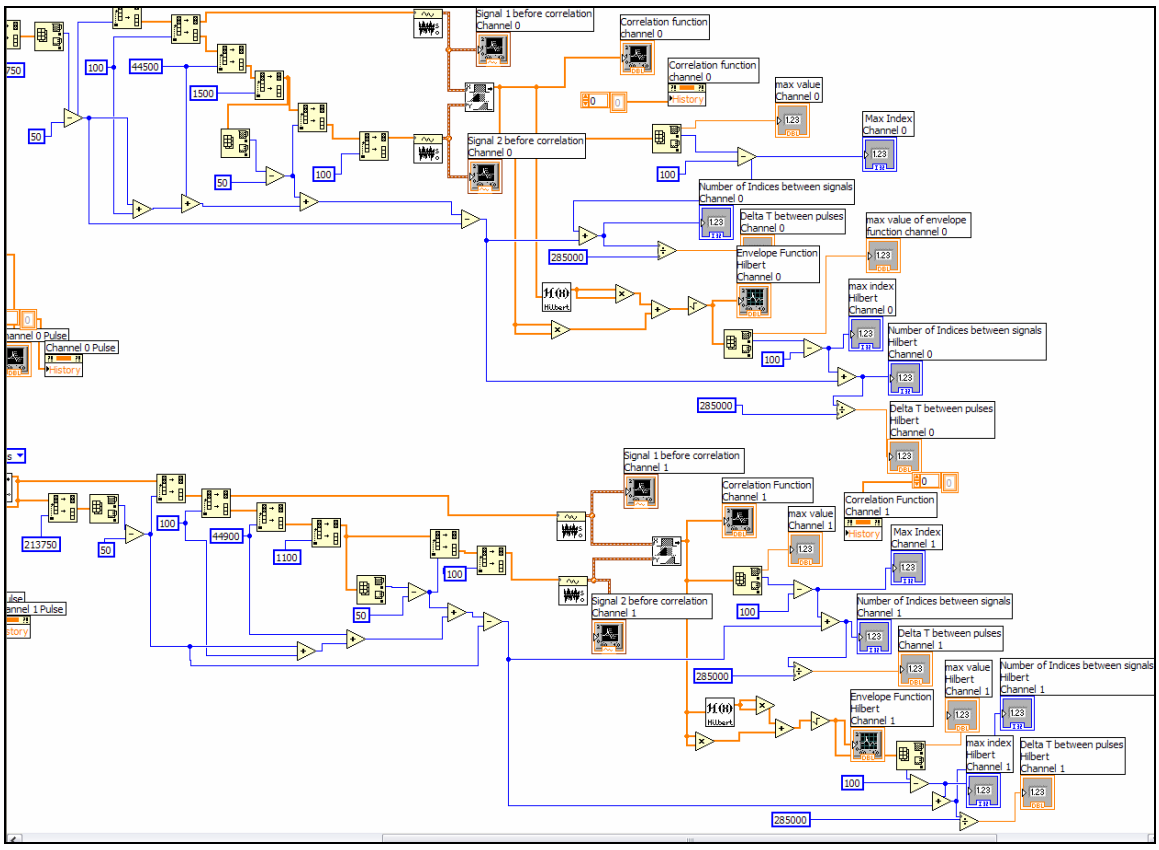
Signal 1 before correlation Channel 0
Correlation function channel 0
Correlation function channel 0
max value Channel 0
Max Index Channel 0
Signal 2 before correlation Channel 0
Number of Indices between signals Channel 0
Delta T between pulses Channel 0
max value of envelope function channel 0
Envelope Function Hilbert Channel 0
max index Hilbert Channel 0
Number of Indices between signals Hilbert Channel 0
Delta T between pulses Hilbert Channel 0
Channel 0 Pulse
Signal 1 before correlation Channel 1
Correlation Function Channel 1
Correlation Function Channel 1
max value Channel 1
Max Index Channel 1
Signal 2 before correlation Channel 1
Number of Indices between signals Channel 1
Delta T between pulses Channel 1
max value Hilbert Channel 1
Number of Indices between signals Hilbert Channel 1
Envelope Function Hilbert Channel 1
max index Hilbert Channel 1
Delta T between pulses Hilbert Channel 1
213750
100
44500
1500
50
285000
44900
1100

Lab View program for data analysis, eliminating ground path segment, front panel and block diagram.

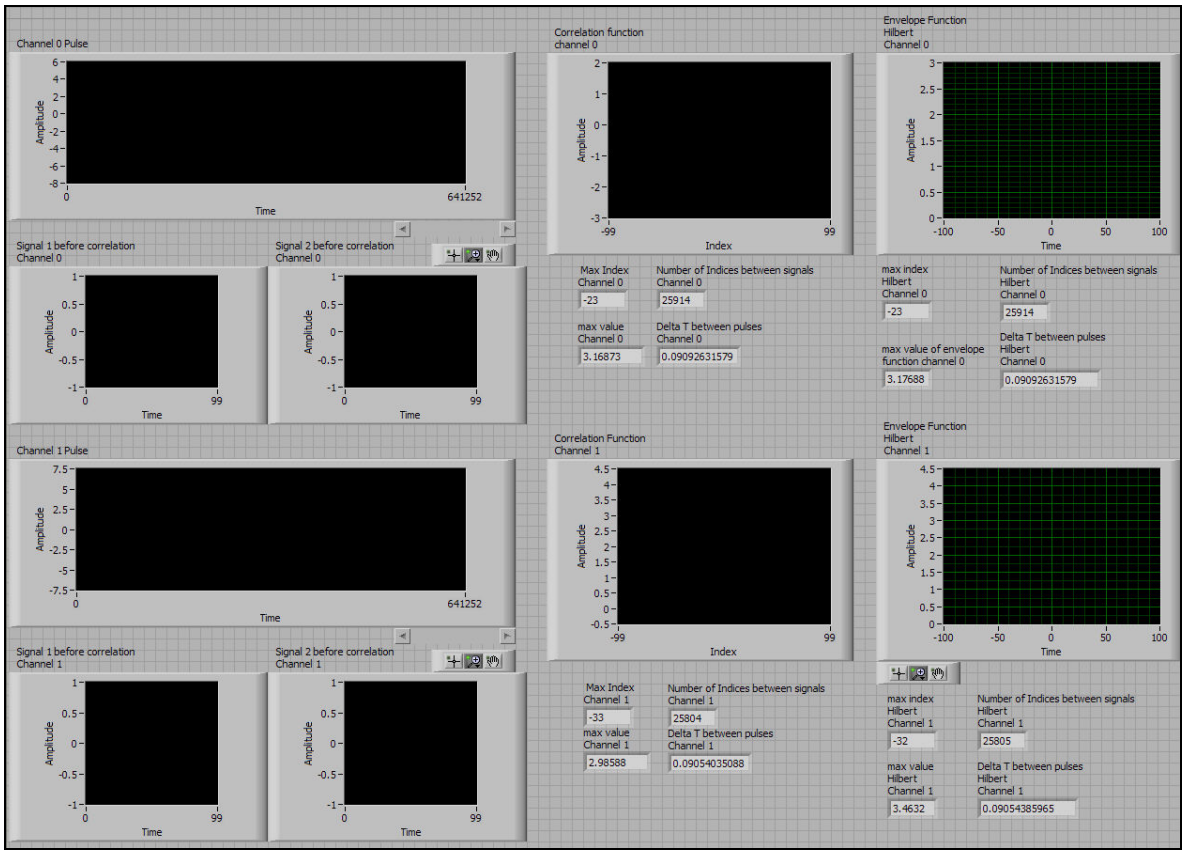

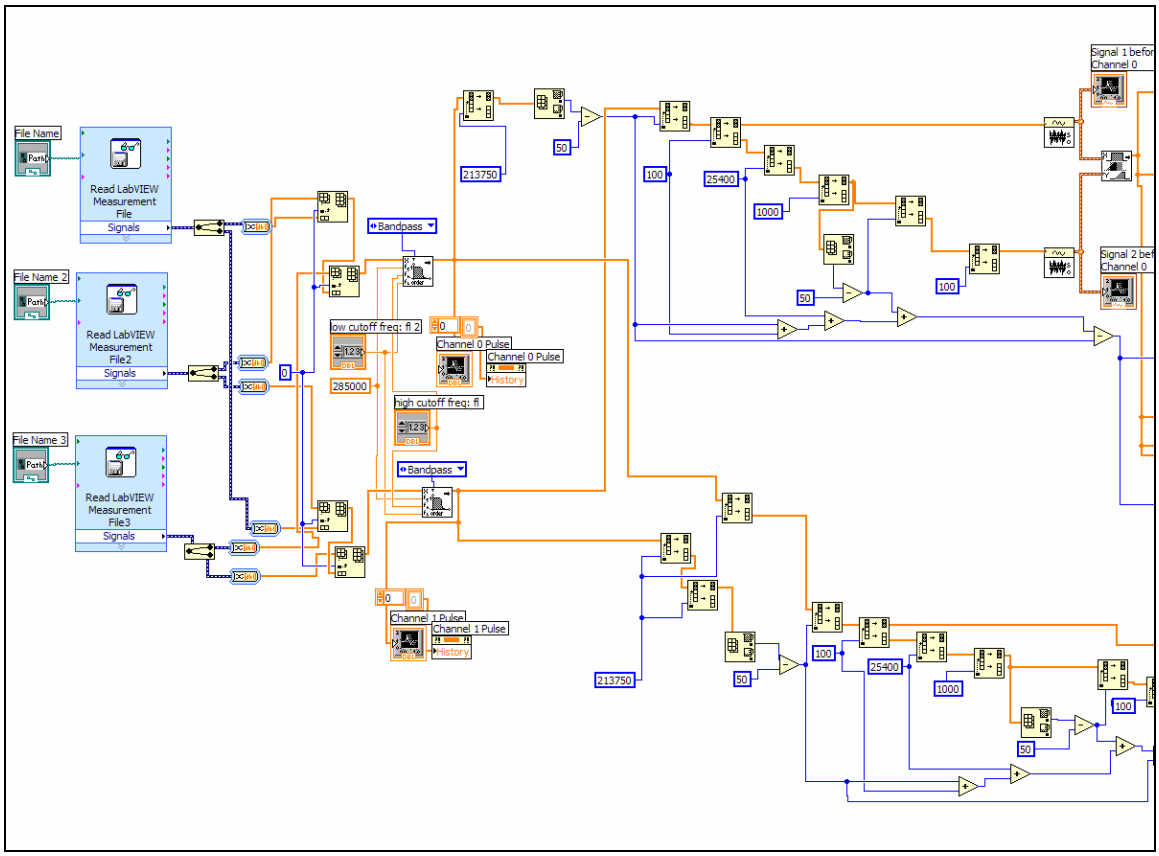
File Name
Read LabVIEW Measurement File
Signals
File Name 2
Read LabVIEW Measurement File2
Signals
File Name 3
Read LabVIEW Measurement File3
Signals
Bandpass
low cutoff freq: fl 2
high cutoff freq: fl
Channel 0 Pulse
Channel 1 Pulse
History
285000
213750
25400
1000
100
50
0

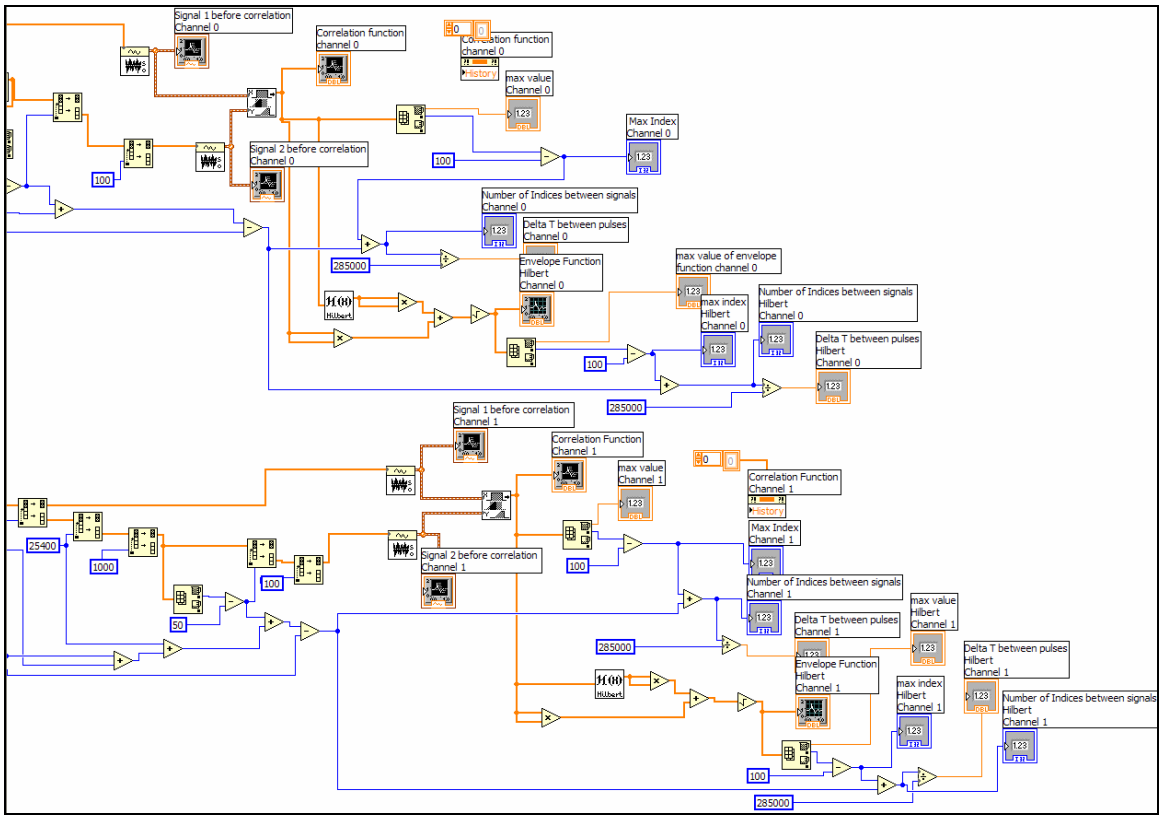
Signal 1 before correlation Channel 0
Correlation function channel 0
max value Channel 0
Max Index Channel 0
Signal 2 before correlation Channel 0
Number of Indices between signals Channel 0
Delta T between pulses Channel 0
Envelope Function Hilbert Channel 0
max value of envelope function channel 0
max index Hilbert Channel 0
Number of Indices between signals Hilbert Channel 0
Delta T between pulses Hilbert Channel 0
Signal 1 before correlation Channel 1
Correlation Function Channel 1
max value Channel 1
Max Index Channel 1
Signal 2 before correlation Channel 1
Number of Indices between signals Channel 1
Delta T between pulses Channel 1
Envelope Function Hilbert Channel 1
max value Hilbert Channel 1
max index Hilbert Channel 1
Delta T between pulses Hilbert Channel 1
Number of Indices between signals Hilbert Channel 1
285000
100
25400
1000
50

Lab View program used to gather frequency spectrum information of aircraft noise data.

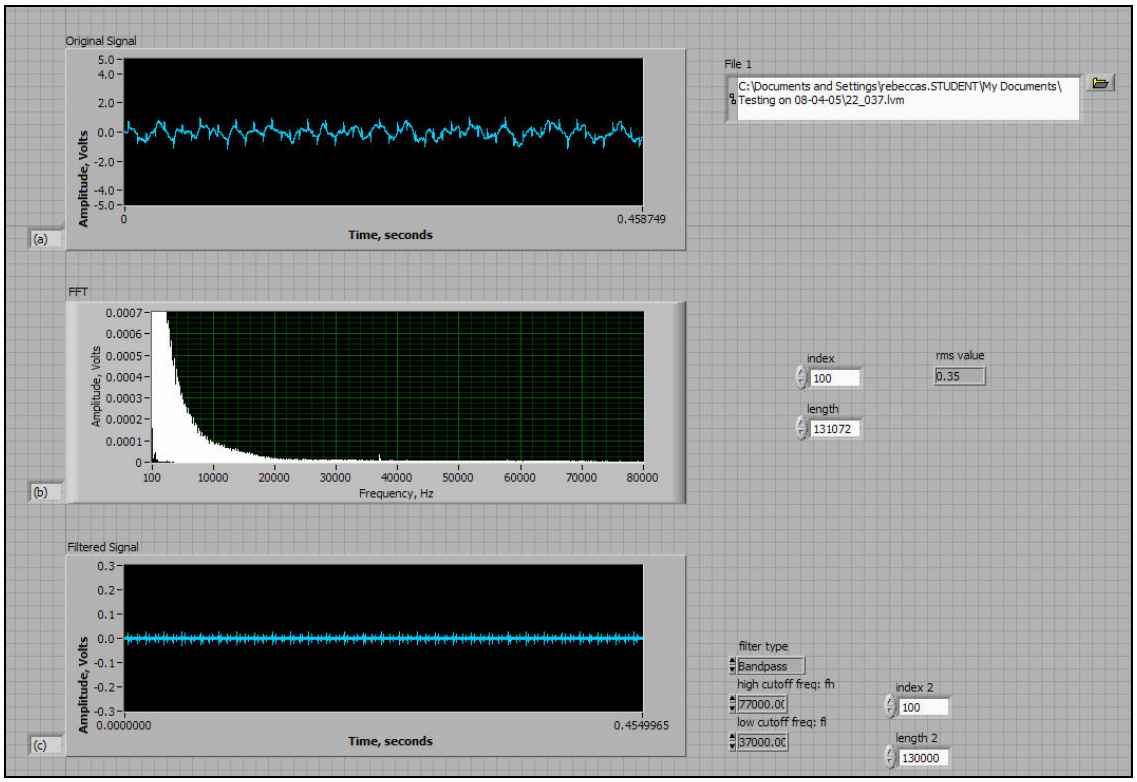

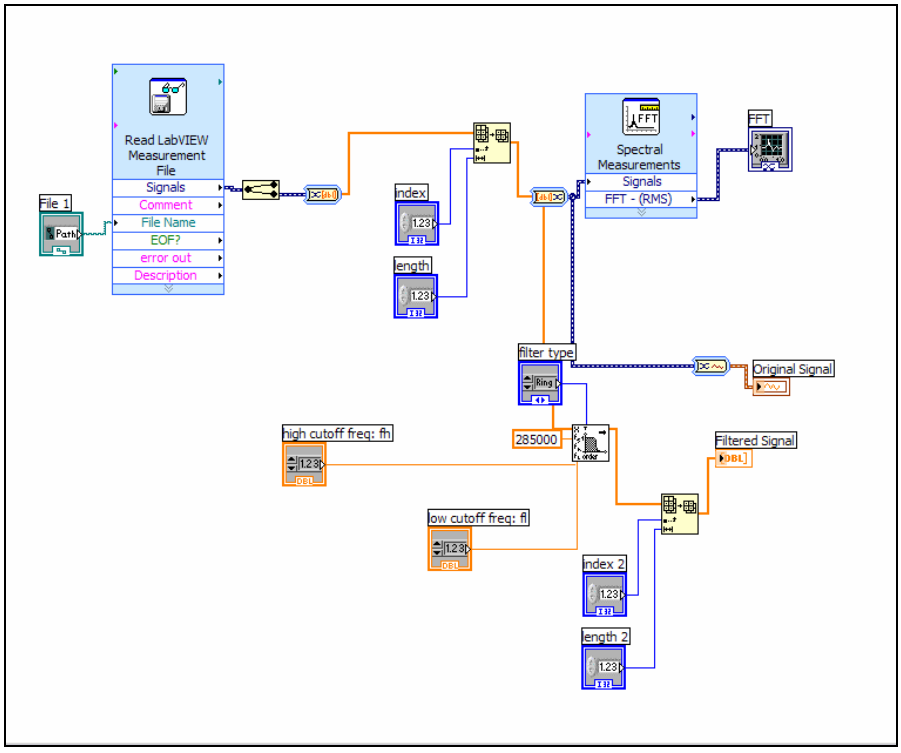

Appendix II

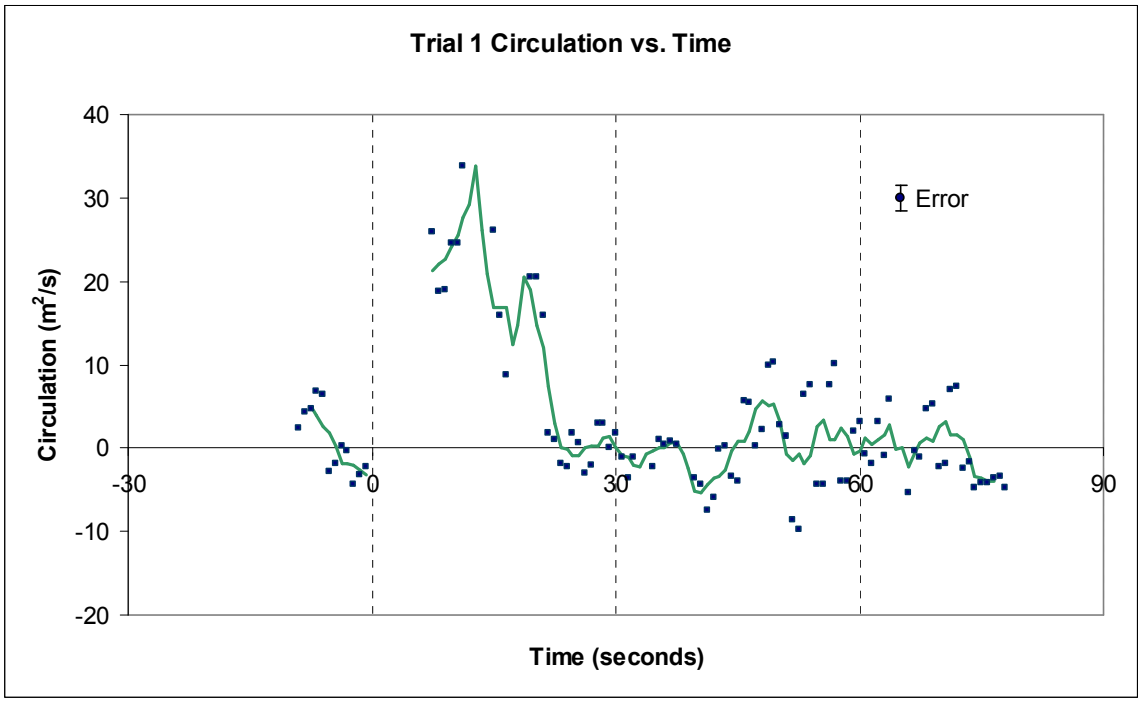
Trial 1 Circulation vs. Time
Circulation (m²/s)
40
30
20
10
0
-10
-20
-30
0
30
60
90
Error
Time (seconds)

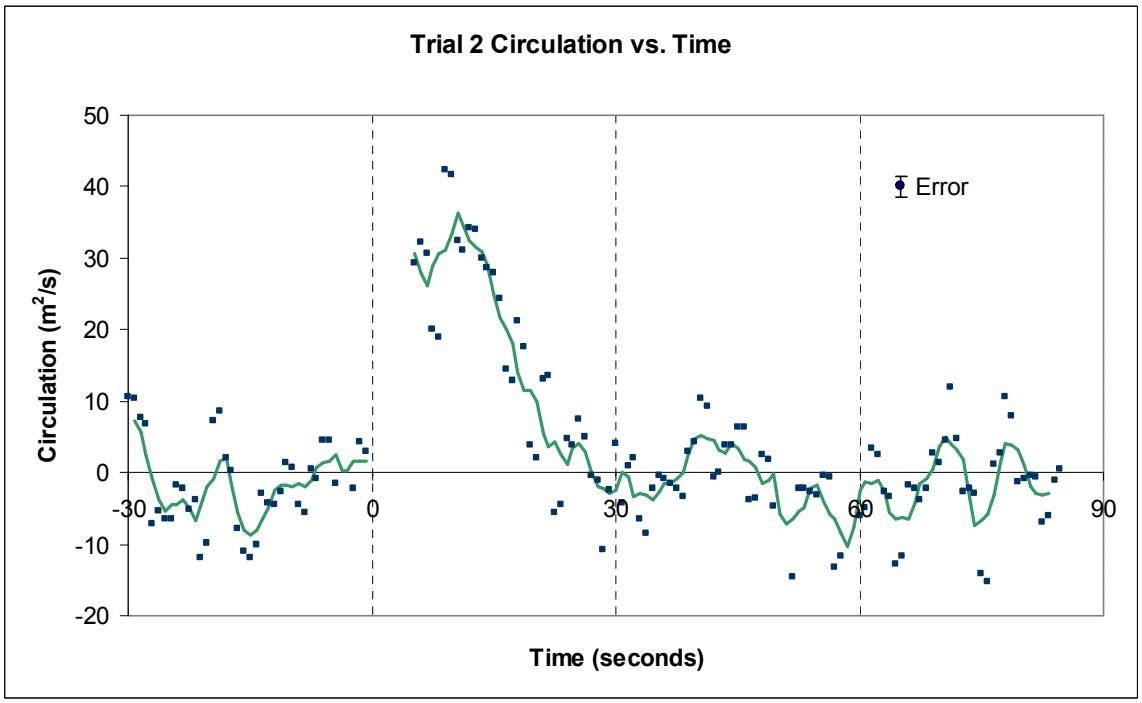
Trial 2 Circulation vs. Time
Circulation (m²/s)
50
40
30
20
10
0
-10
-20
-30
0
30
60
90
Error
Time (seconds)

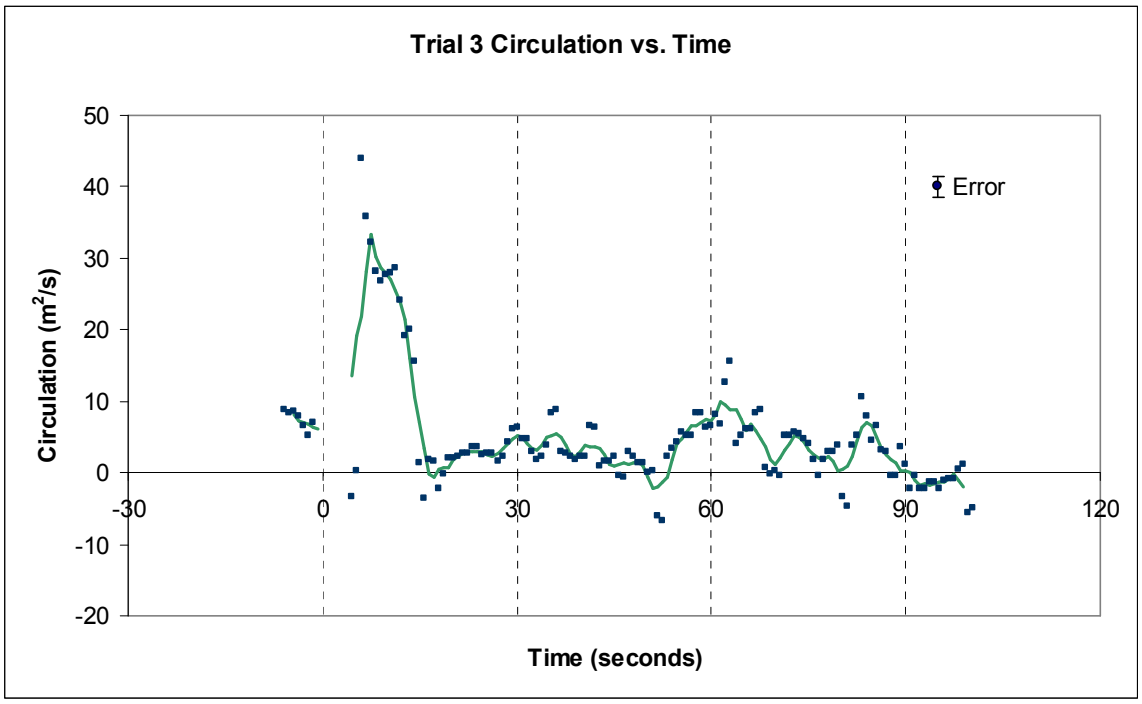
Trial 3 Circulation vs. Time
Circulation (m²/s)
50
40
30
20
10
0
-10
-20
-30
0
30
60
90
120
Error
Time (seconds)

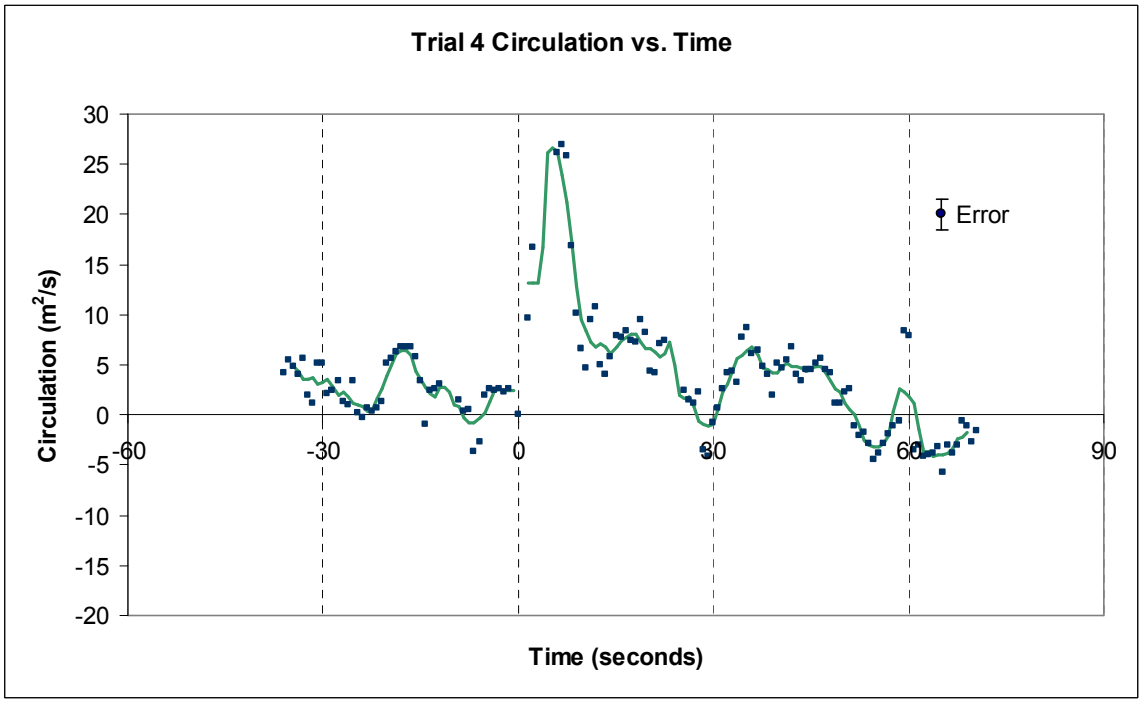
Trial 4 Circulation vs. Time
Circulation (m²/s)
30
25
20
15
10
5
0
-5
-10
-15
-20
-60
-30
0
30
60
90
Error
Time (seconds)

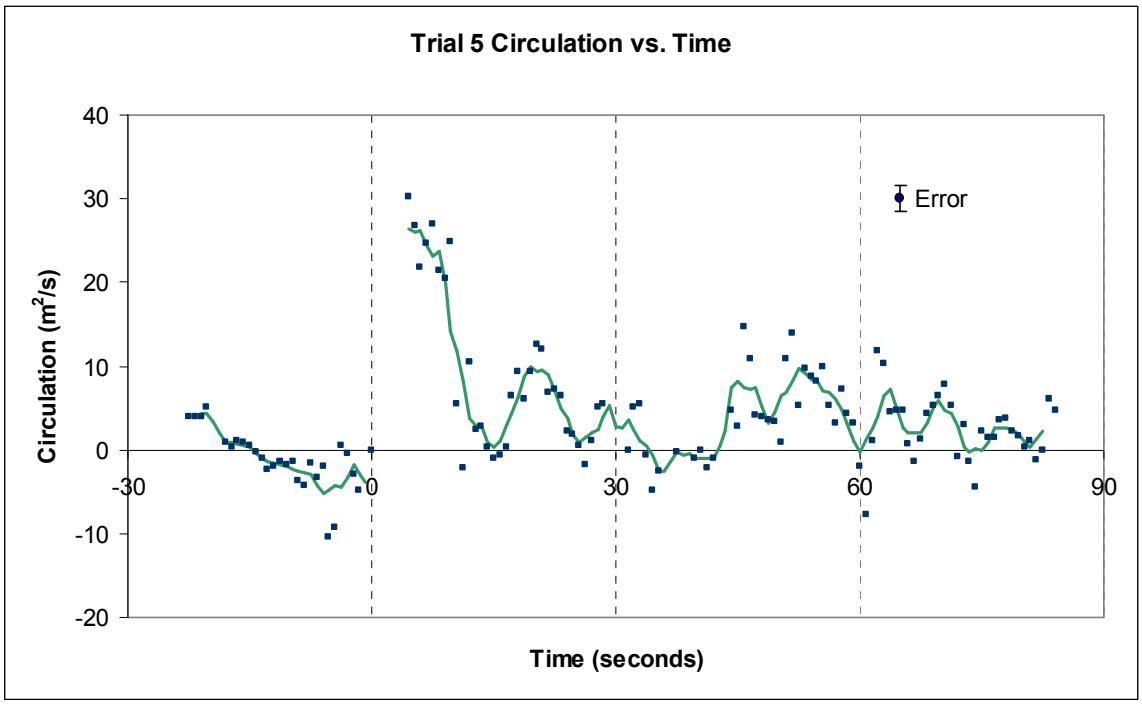
Trial 5 Circulation vs. Time
Circulation (m²/s)
40
30
20
10
0
-10
-20
-30
0
30
60
90
Error
Time (seconds)

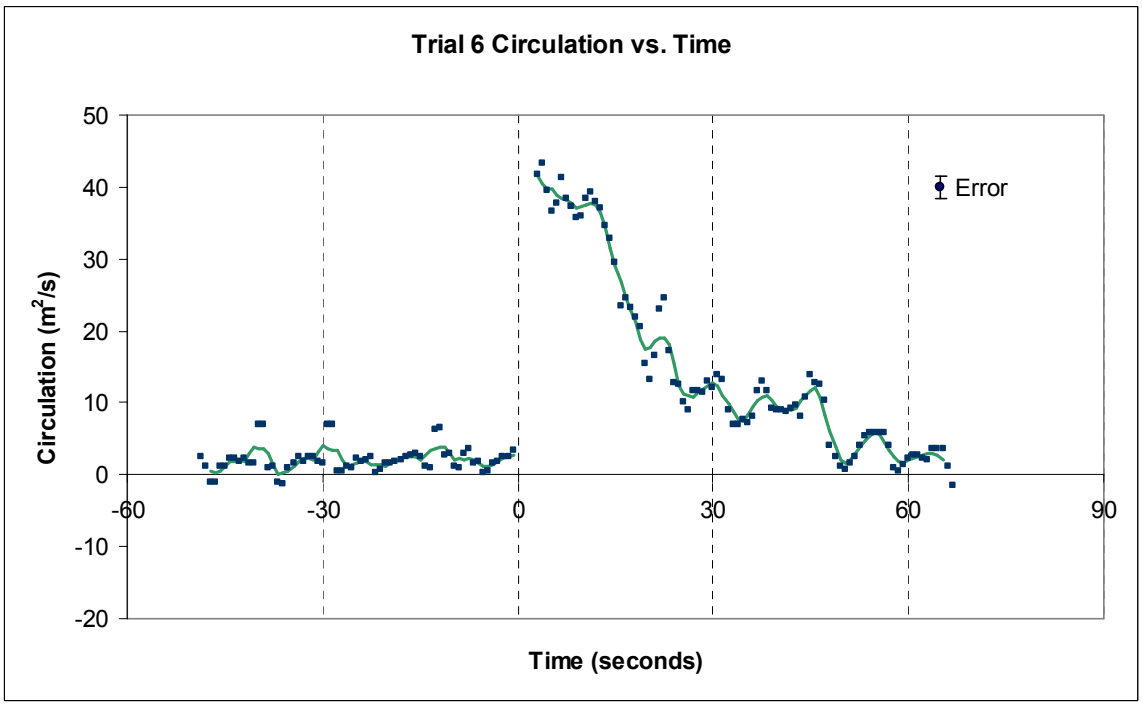
Trial 6 Circulation vs. Time
Circulation (m²/s)
50
40
30
20
10
0
-10
-20
-60
-30
0
30
60
90
Error
Time (seconds)

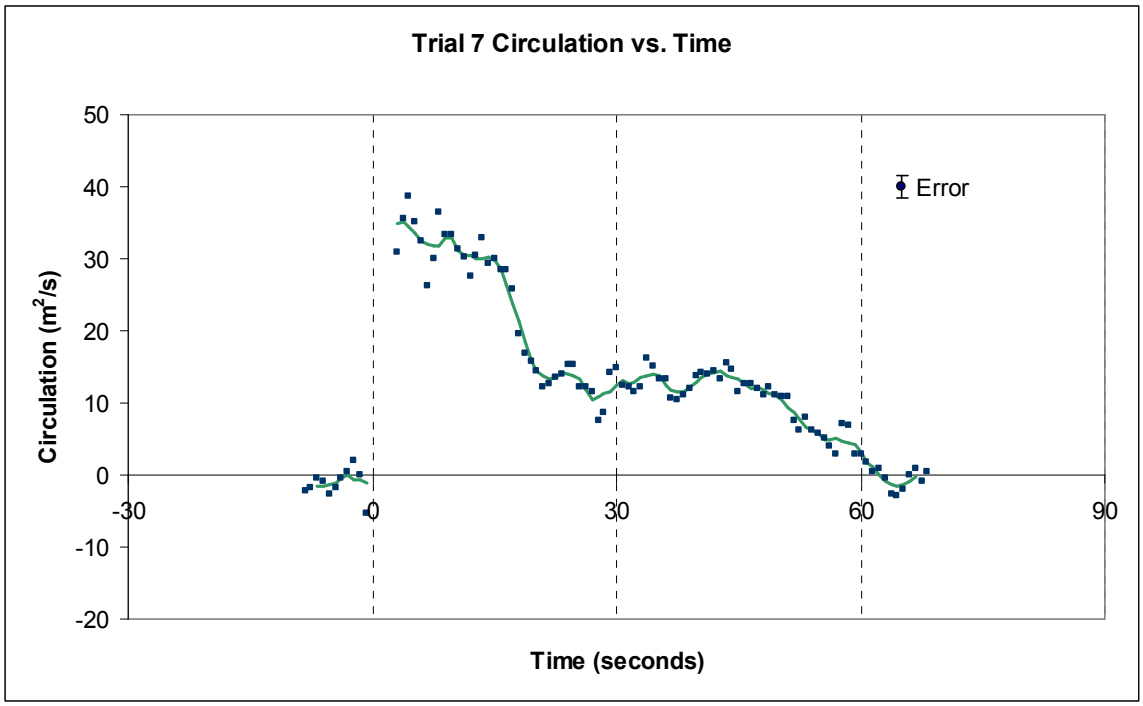
Trial 7 Circulation vs. Time
Circulation (m²/s)
50
40
30
20
10
0
-10
-20
-30
0
30
60
90
Error
Time (seconds)

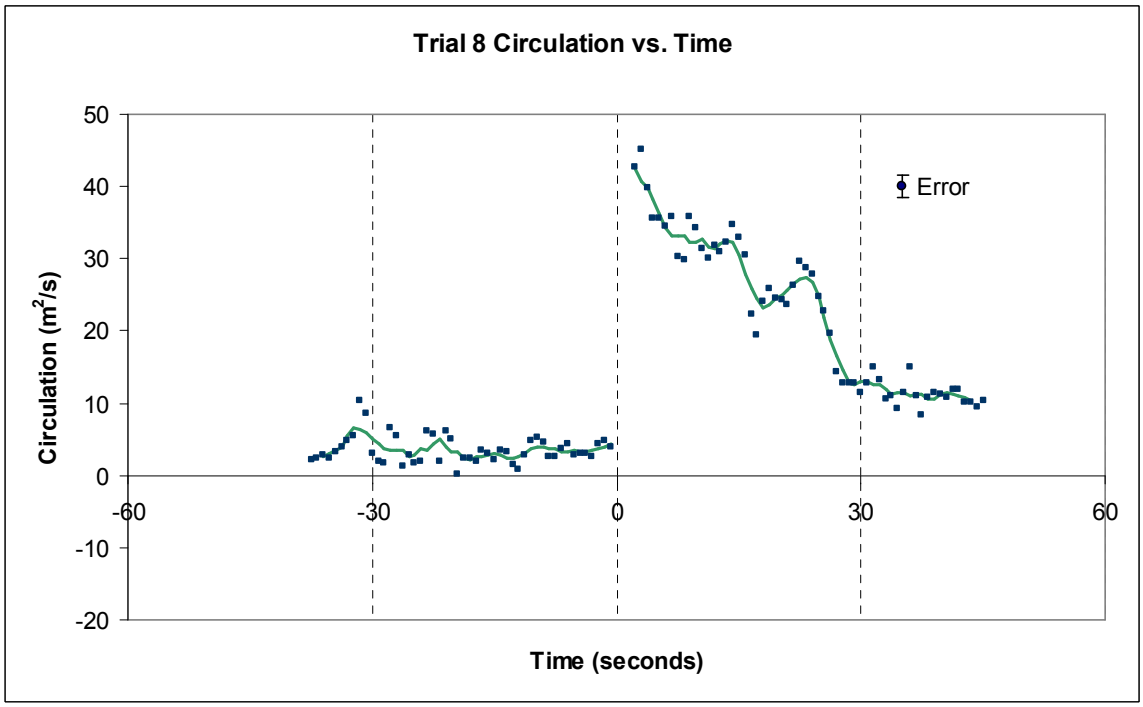
Trial 8 Circulation vs. Time
Circulation (m²/s)
50
40
30
20
10
0
-10
-20
-60
-30
0
30
60
Error
Time (seconds)

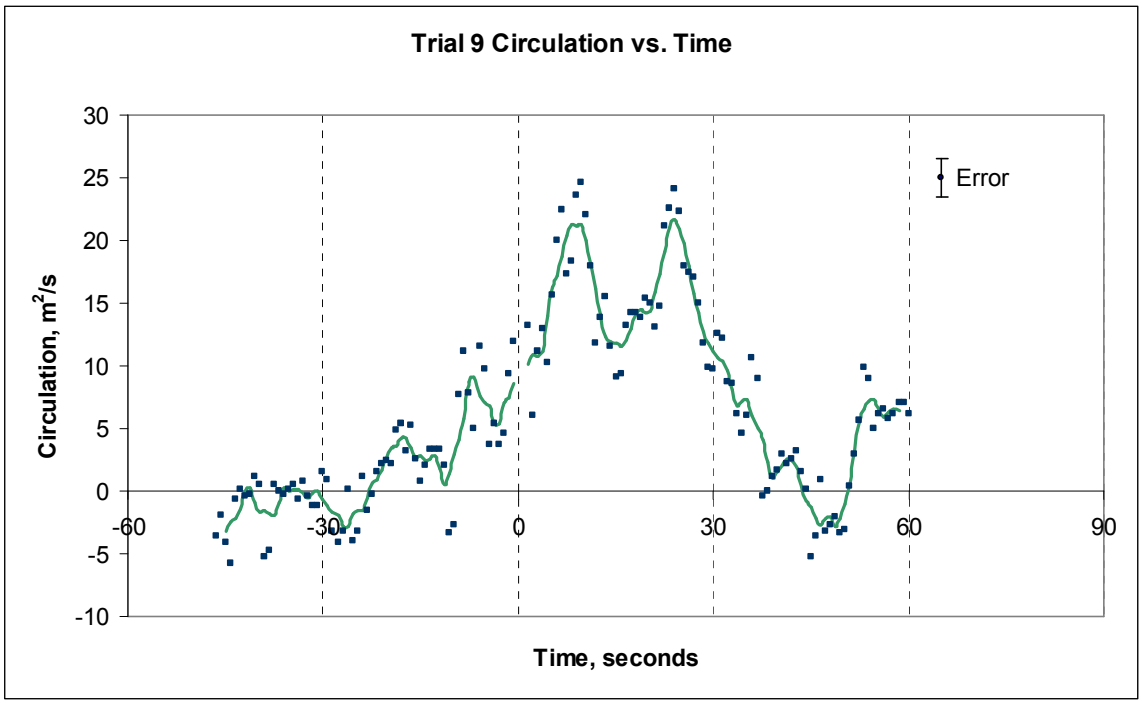
Trial 9 Circulation vs. Time
Circulation, m²/s
30
25
20
15
10
5
0
-5
-10
-60
-30
0
30
60
90
Error
Time, seconds

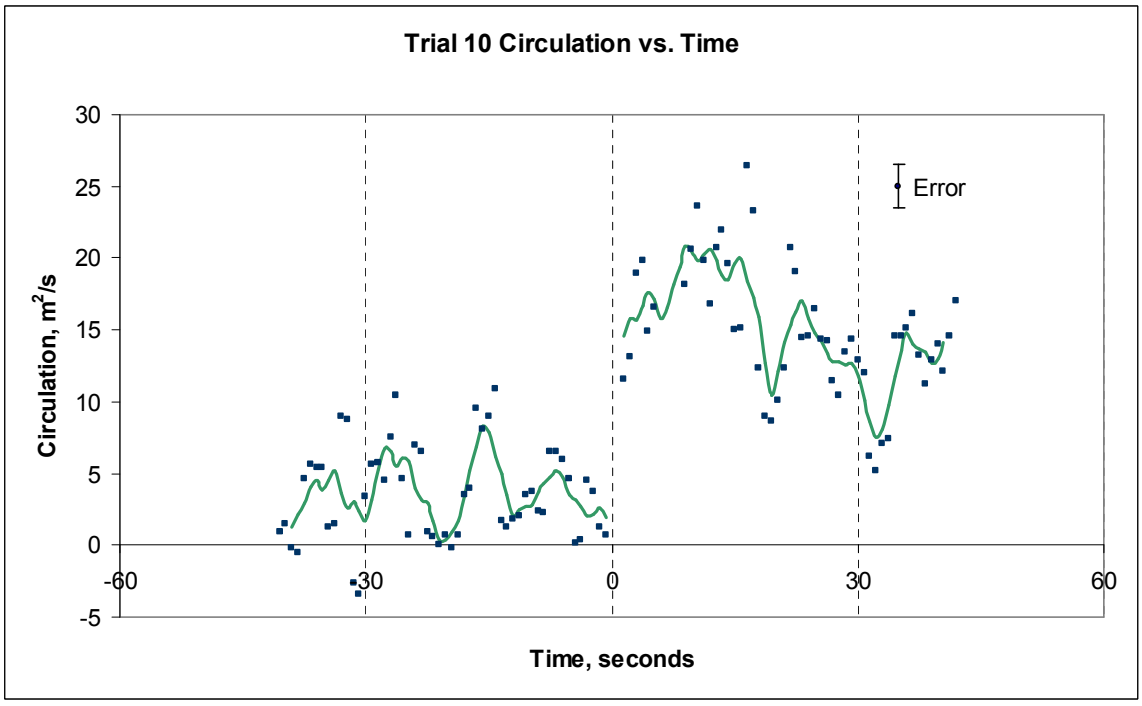
Trial 10 Circulation vs. Time
Circulation, m²/s
30
25
20
15
10
5
0
-5
-60
-30
0
30
60
Error
Time, seconds

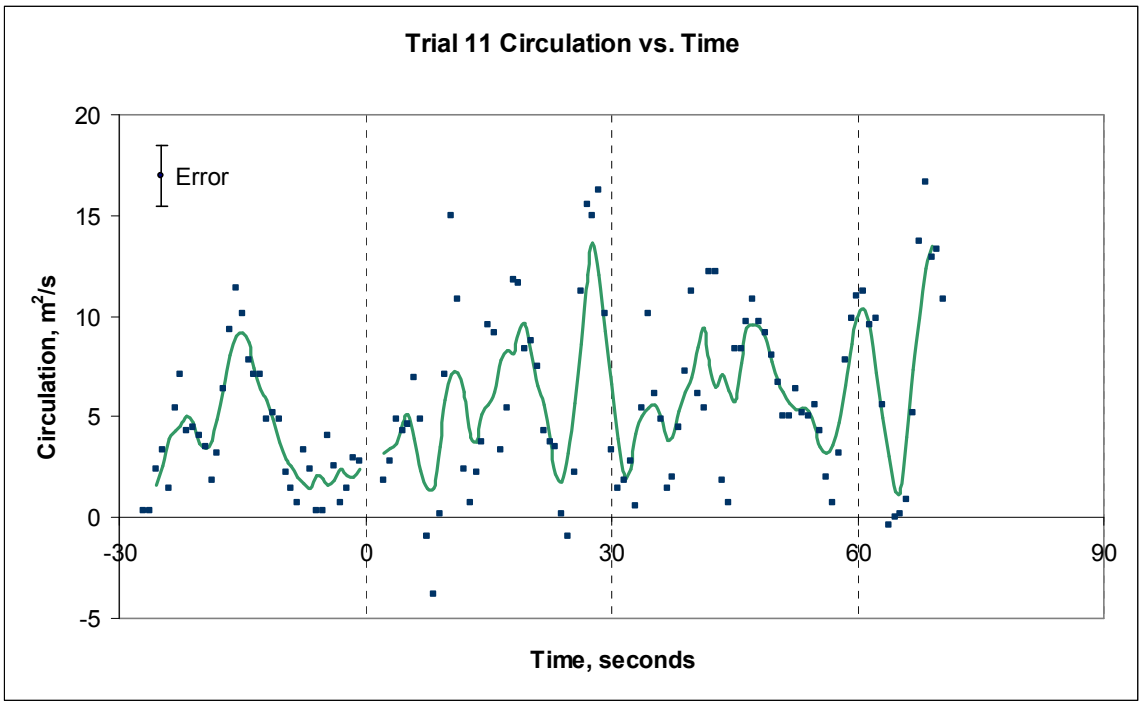
Trial 11 Circulation vs. Time
Error
Circulation, m²/s
20
15
10
5
0
-5
-30
0
30
60
90
Time, seconds

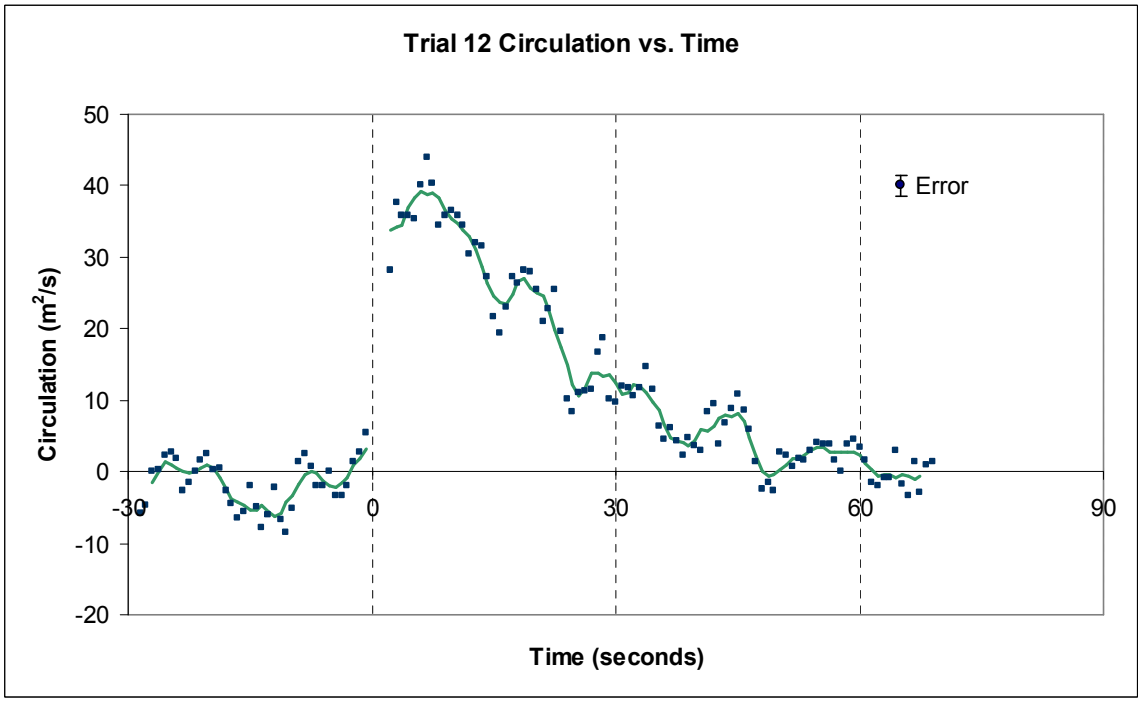
Trial 12 Circulation vs. Time
Error
Circulation (m²/s)
50
40
30
20
10
0
-10
-20
-30
0
30
60
90
Time (seconds)

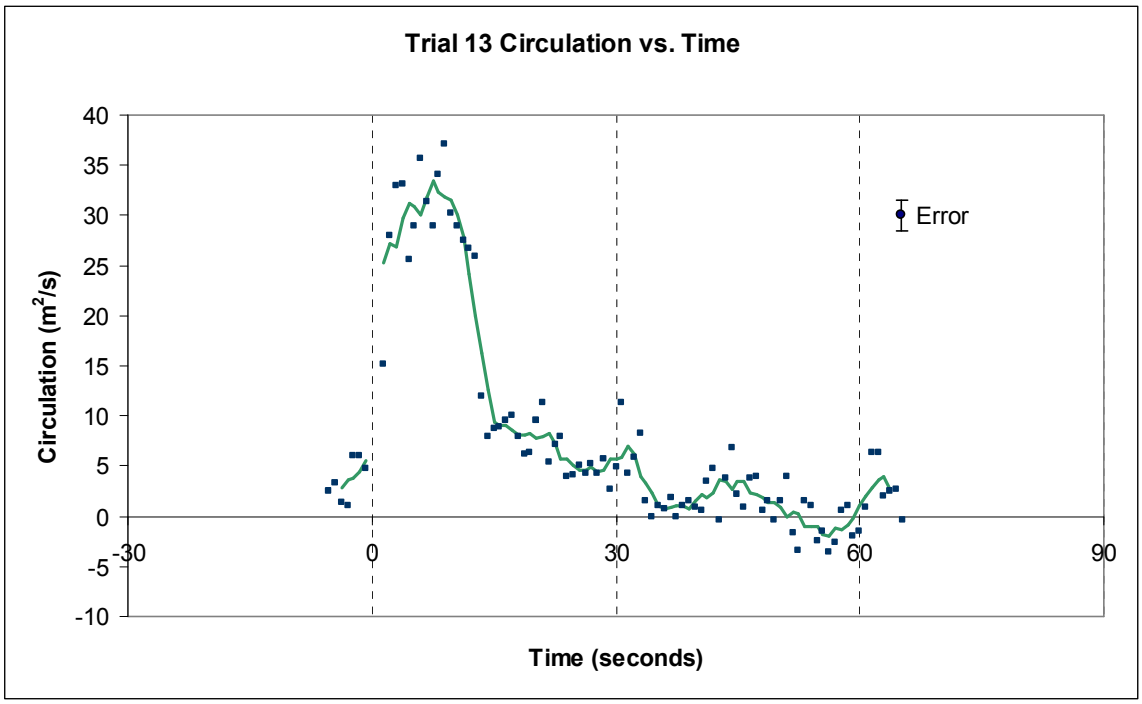
Trial 13 Circulation vs. Time
Circulation (m²/s)
40
35
30
25
20
15
10
5
0
-5
-10
-30
0
30
60
90
Time (seconds)
Error

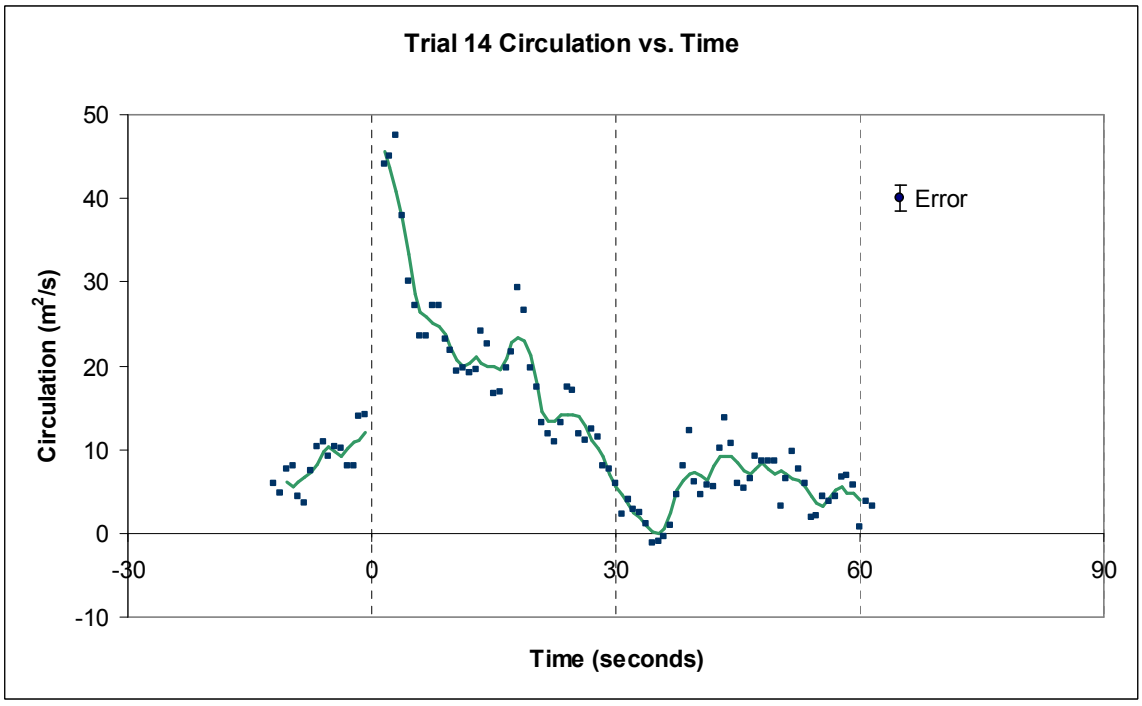
Trial 14 Circulation vs. Time
Circulation (m²/s)
50
40
30
20
10
0
-10
-30
0
30
60
90
Time (seconds)
Error

Appendix III

The following charts depict aircraft noise samples gathered at Manchester Airport, and are labeled as indicated in Table 4.5. The original sound sample is shown in (a), the frequency spectrum is depicted in (b), and the original signal sent through a bandpass filter with limits of 37 kHz and 77 kHz is shown in (c).

MHT-01

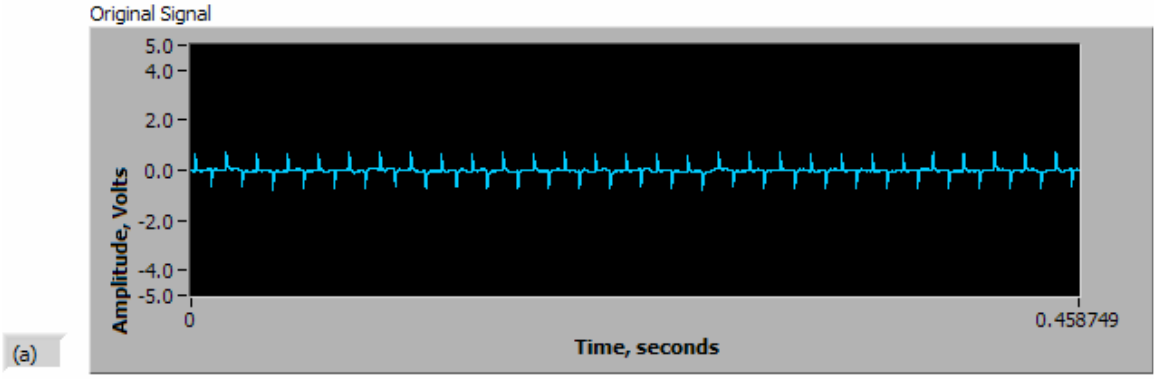

(a)

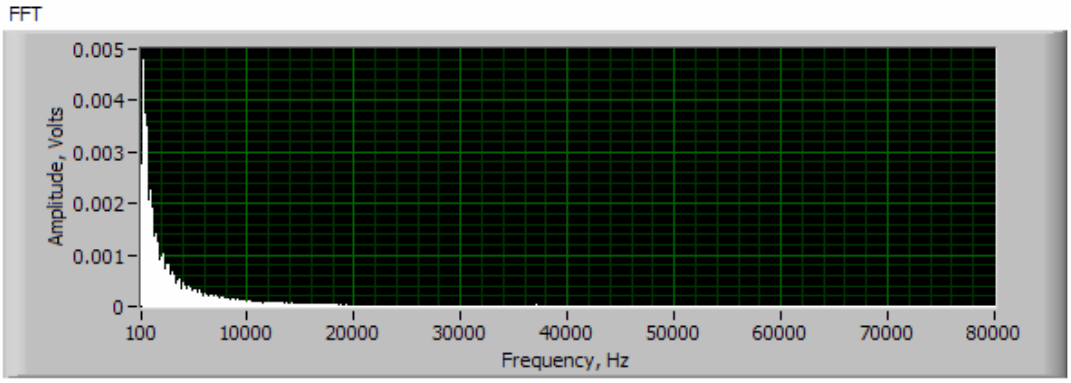

(b)

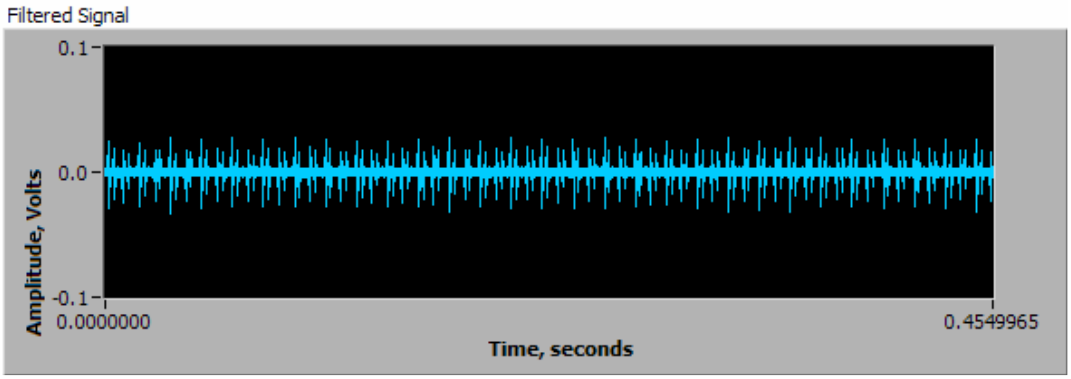

(c)

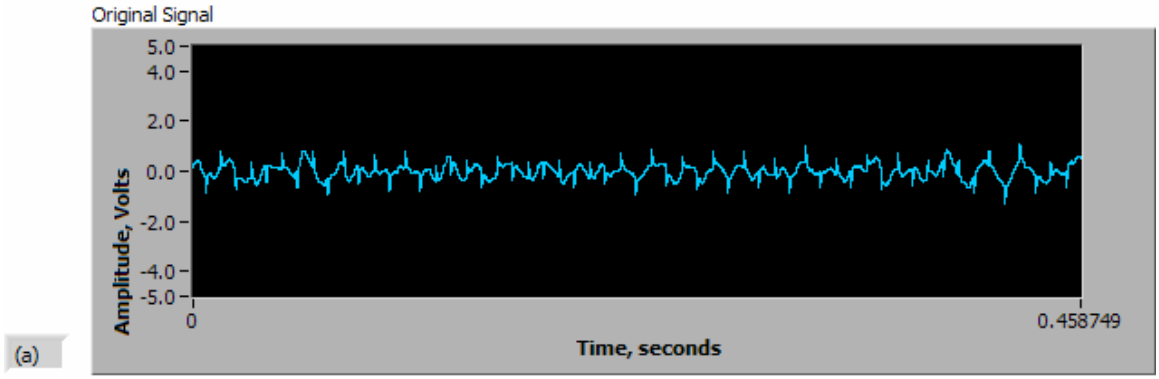
Original Signal
5.0
4.0
2.0
0.0
-2.0
-4.0
-5.0
Amplitude, Volts
0
0.458749
Time, seconds

(a)

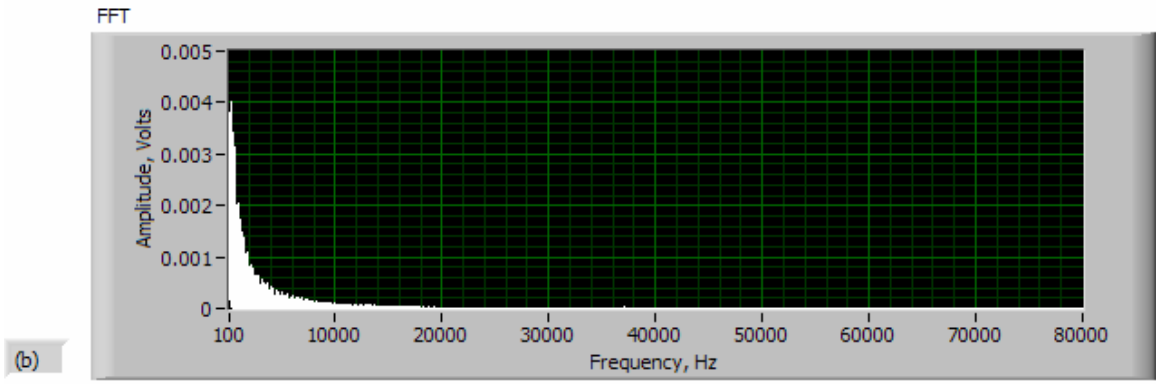
FFT
0.005
0.004
0.003
0.002
0.001
0
Amplitude, Volts
100
10000
20000
30000
40000
50000
60000
70000
80000
Frequency, Hz

(b)

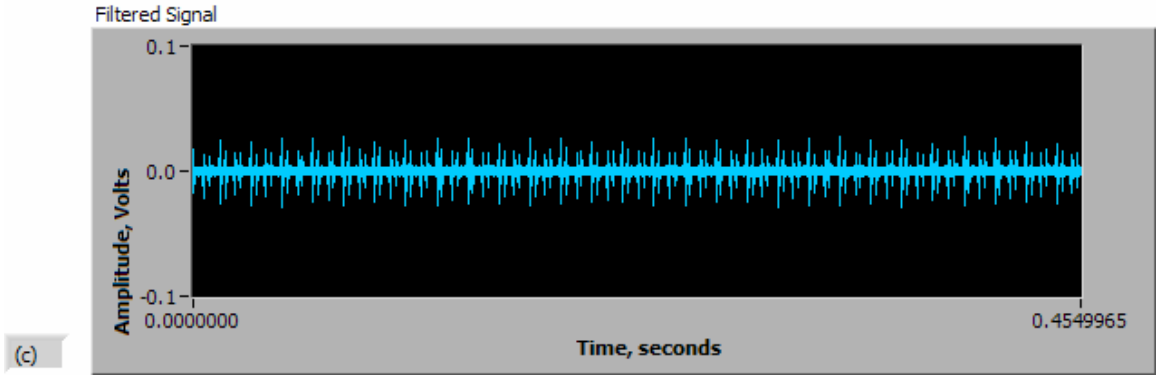
Filtered Signal
0.1
0.0
-0.1
Amplitude, Volts
0.0000000
0.4549965
Time, seconds

(c)

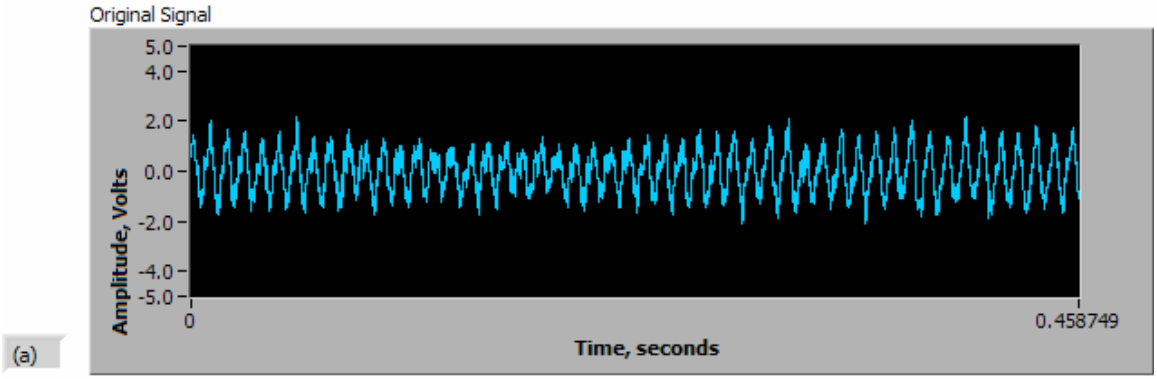
Original Signal
5.0
4.0
2.0
0.0
-2.0
-4.0
-5.0
Amplitude, Volts
0
0.458749
Time, seconds

(a)

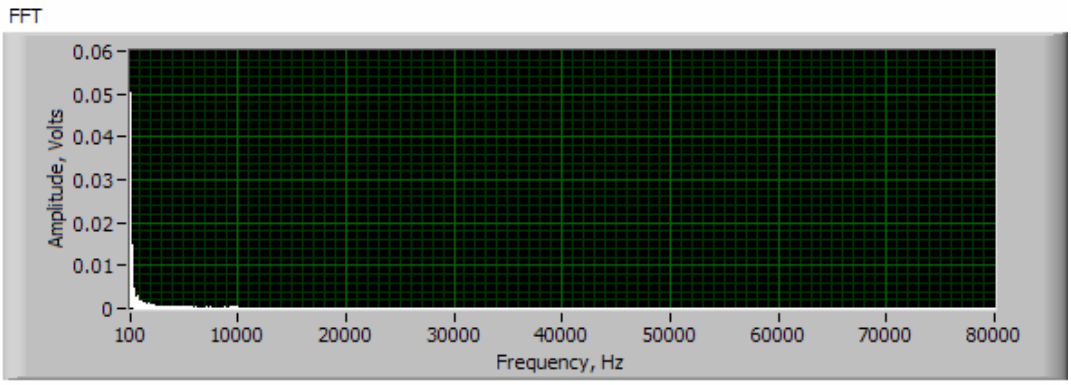
FFT
0.06
0.05
0.04
0.03
0.02
0.01
0
Amplitude, Volts
100
10000
20000
30000
40000
50000
60000
70000
80000
Frequency, Hz

(b)

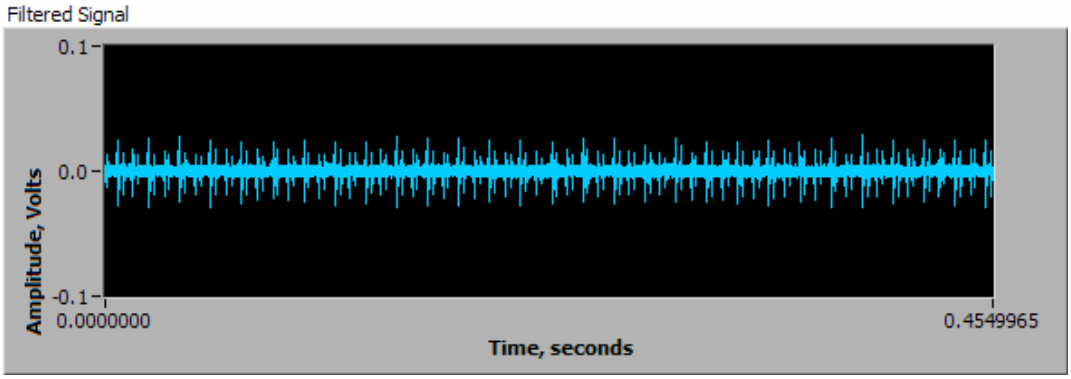
Filtered Signal
0.1
0.0
-0.1
Amplitude, Volts
0.0000000
0.4549965
Time, seconds

(c)

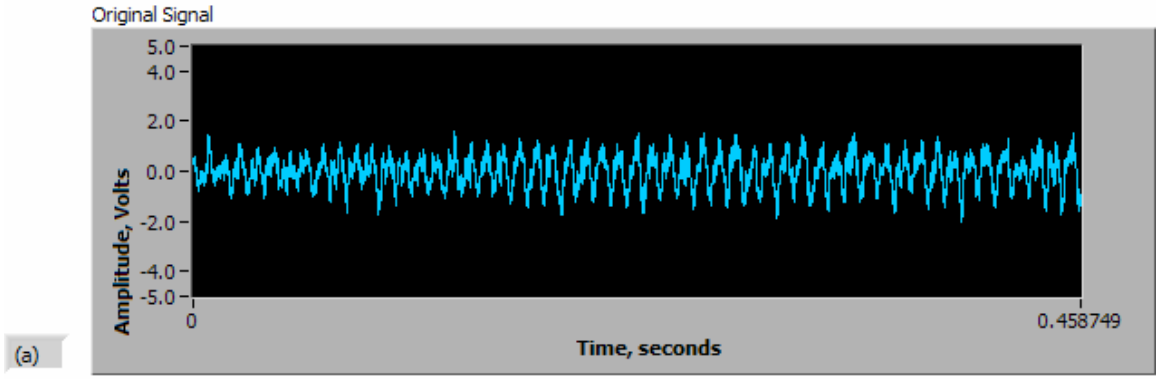
Original Signal
5.0
4.0
2.0
0.0
-2.0
-4.0
-5.0
Amplitude, Volts
0
0.458749
Time, seconds

(a)

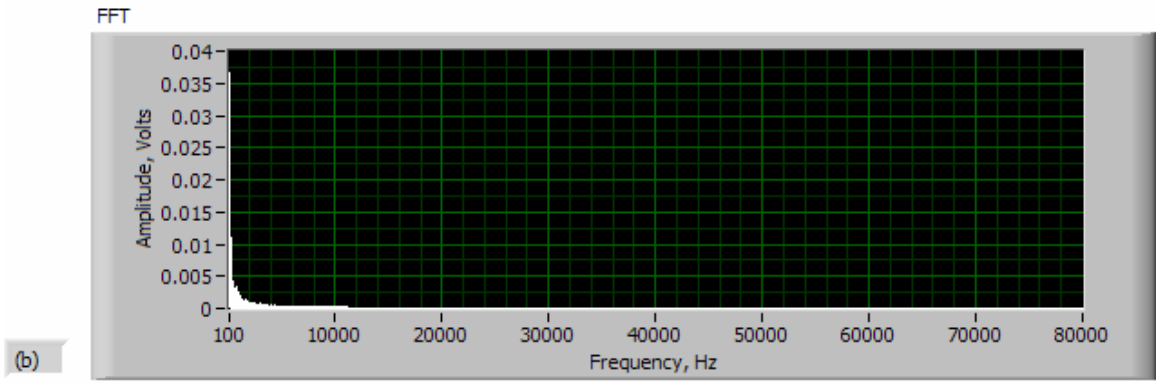
FFT
0.04
0.035
0.03
0.025
0.02
0.015
0.01
0.005
0
Amplitude, Volts
100
10000
20000
30000
40000
50000
60000
70000
80000
Frequency, Hz

(b)

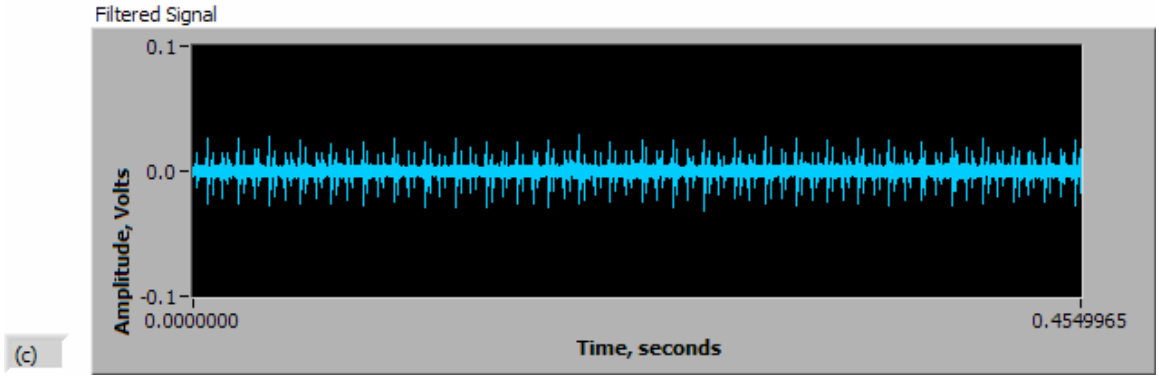
Filtered Signal
0.1
0.0
-0.1
Amplitude, Volts
0.0000000
0.4549965
Time, seconds

(c)

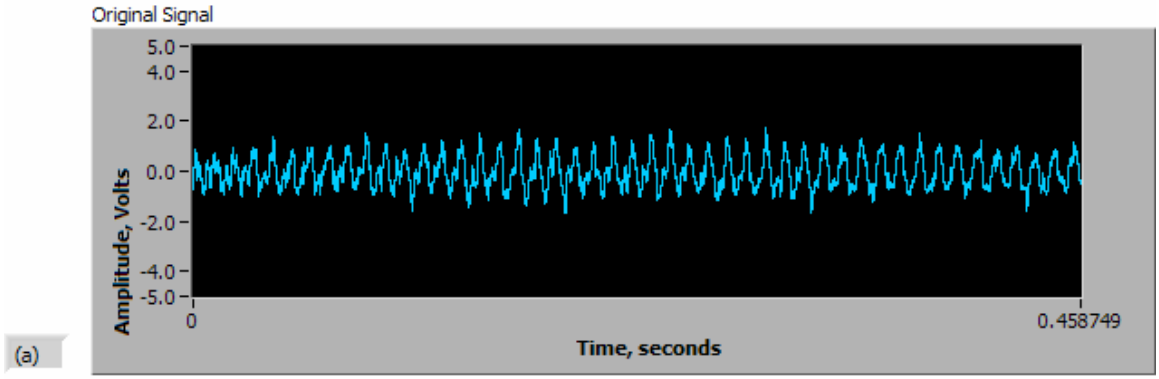
Original Signal
5.0
4.0
2.0
0.0
-2.0
-4.0
-5.0
Amplitude, Volts
0
0.458749
Time, seconds

(a)

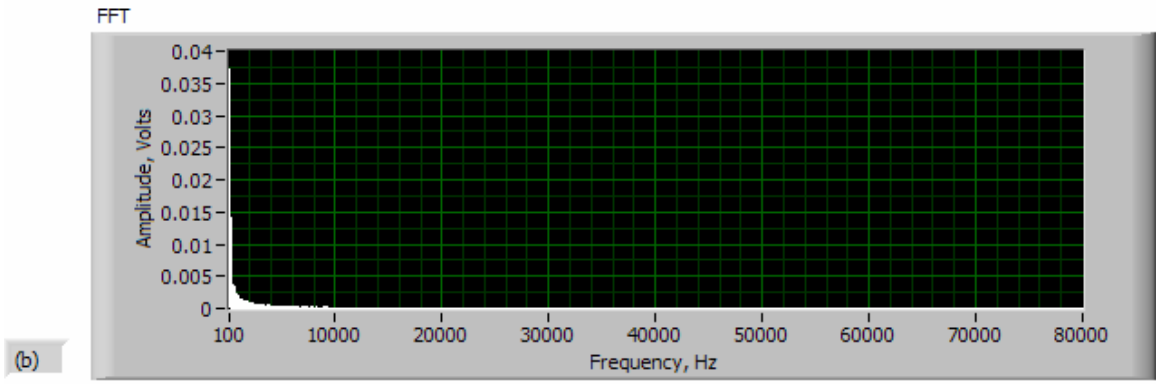
FFT
0.04
0.035
0.03
0.025
0.02
0.015
0.01
0.005
0
Amplitude, Volts
100
10000
20000
30000
40000
50000
60000
70000
80000
Frequency, Hz

(b)

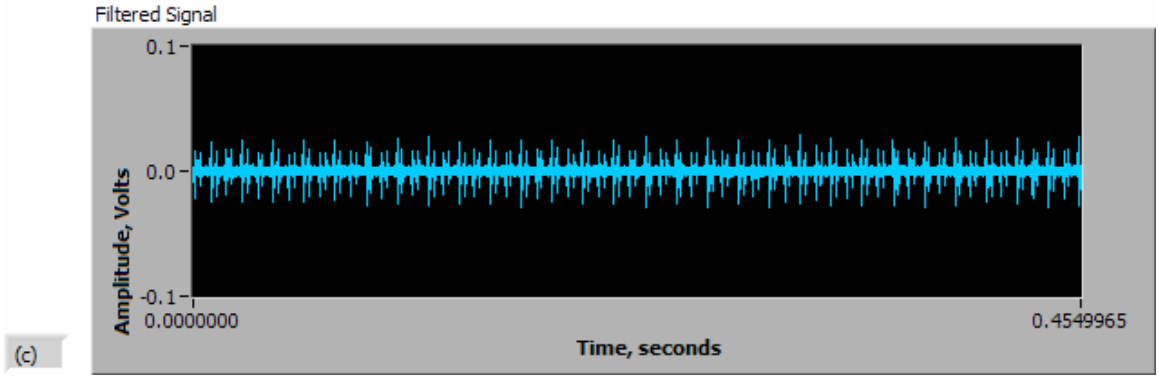
Filtered Signal
0.1
0.0
-0.1
Amplitude, Volts
0.0000000
0.4549965
Time, seconds

(c)

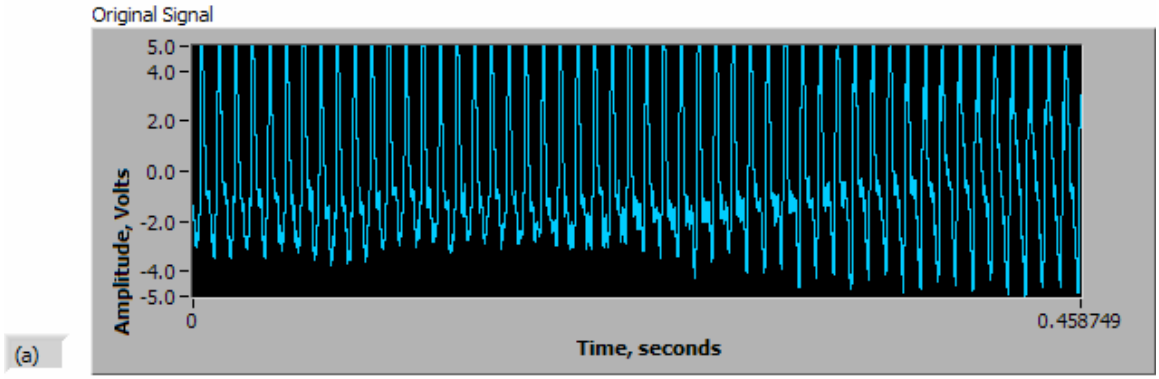
Original Signal
5.0
4.0
2.0
0.0
-2.0
-4.0
-5.0
Amplitude, Volts
0
0.458749
Time, seconds

(a)

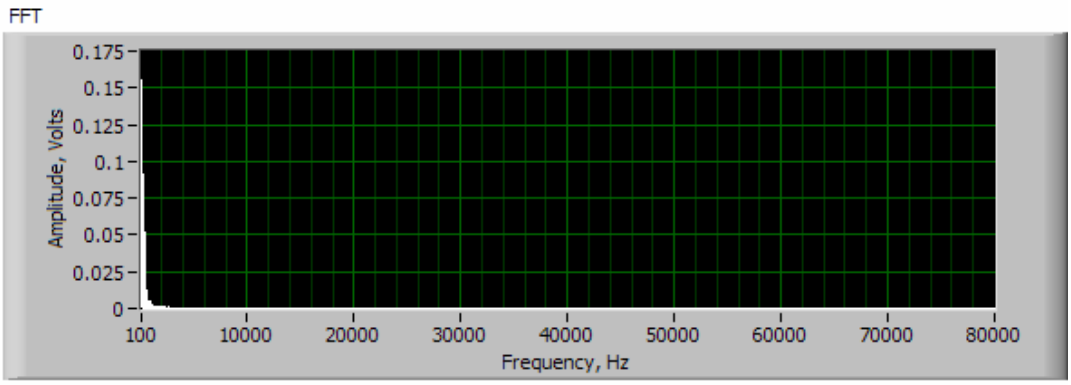
FFT
0.175
0.15
0.125
0.1
0.075
0.05
0.025
0
Amplitude, Volts
100
10000
20000
30000
40000
50000
60000
70000
80000
Frequency, Hz

(b)

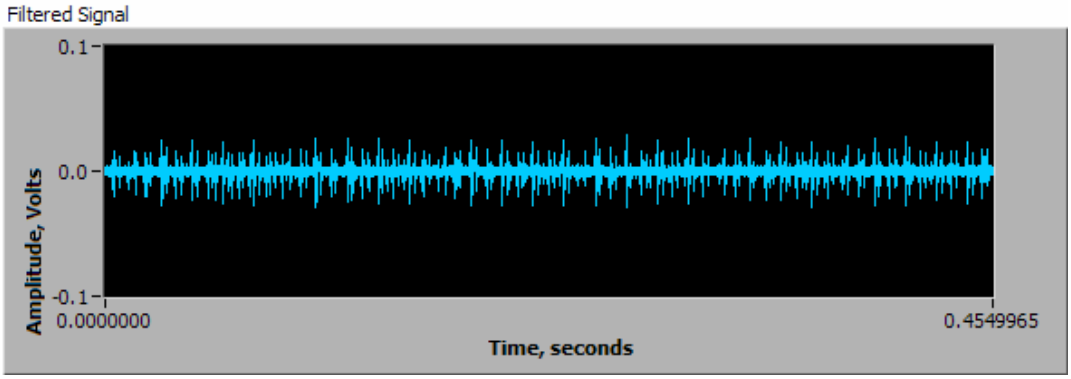
Filtered Signal
0.1
0.0
-0.1
Amplitude, Volts
0.0000000
0.4549965
Time, seconds

(c)

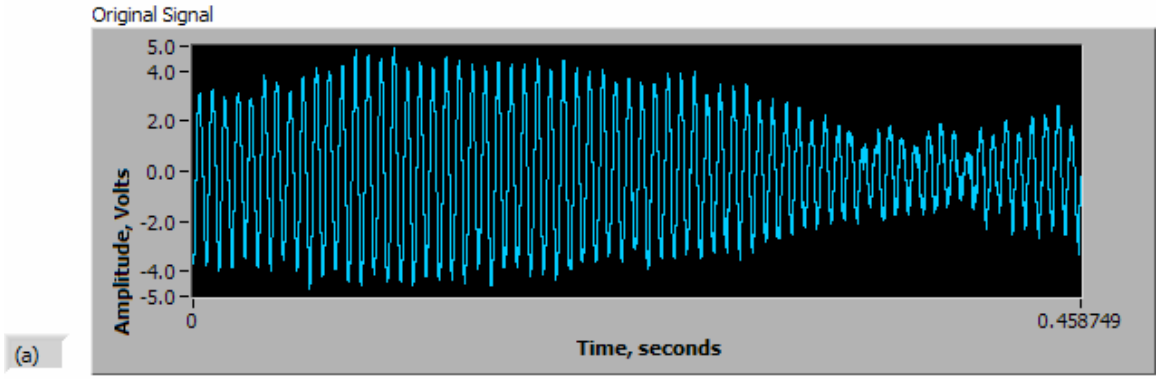
Original Signal
5.0
4.0
2.0
0.0
-2.0
-4.0
-5.0
Amplitude, Volts
0
0.458749
Time, seconds

(a)

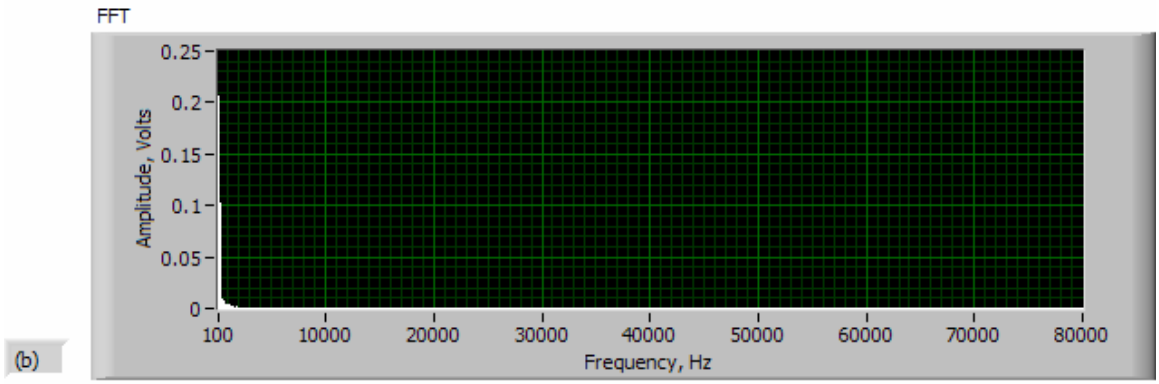
FFT
0.25
0.2
0.15
0.1
0.05
0
Amplitude, Volts
100
10000
20000
30000
40000
50000
60000
70000
80000
Frequency, Hz

(b)

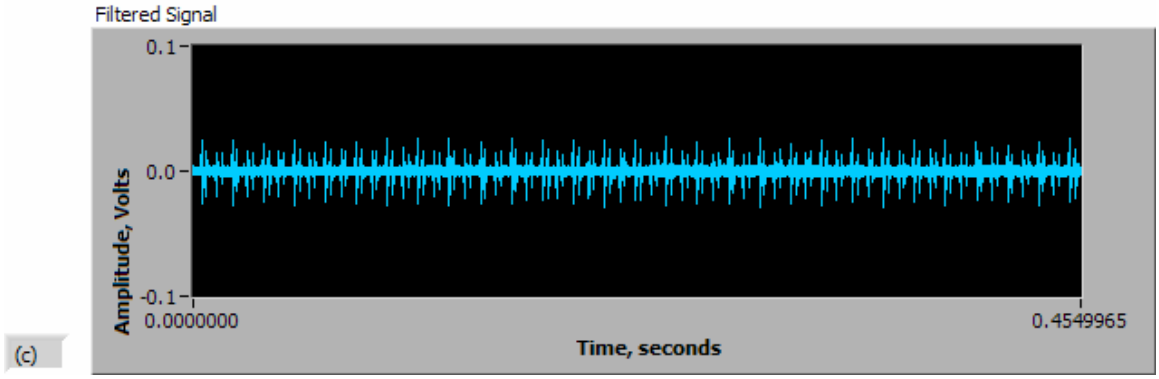
Filtered Signal
0.1
0.0
-0.1
Amplitude, Volts
0.0000000
0.4549965
Time, seconds

(c)

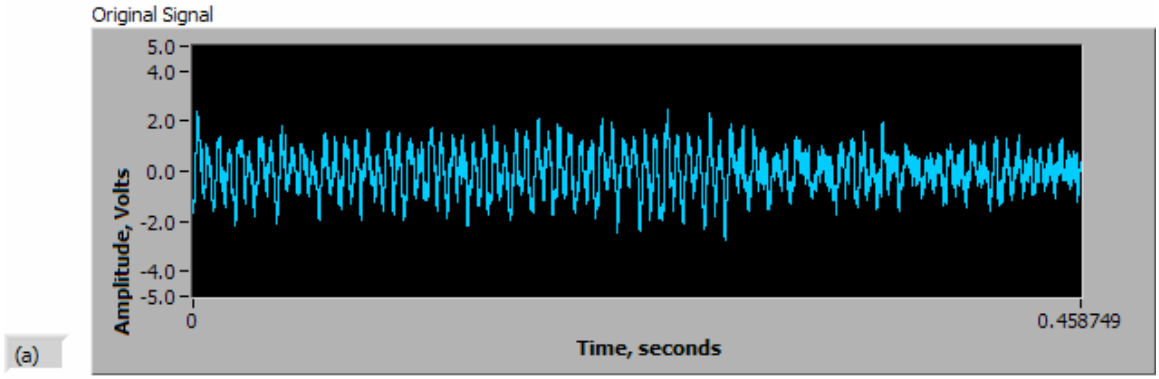
Original Signal
5.0
4.0
2.0
0.0
-2.0
-4.0
-5.0
Amplitude, Volts
0
0.458749
Time, seconds

(a)

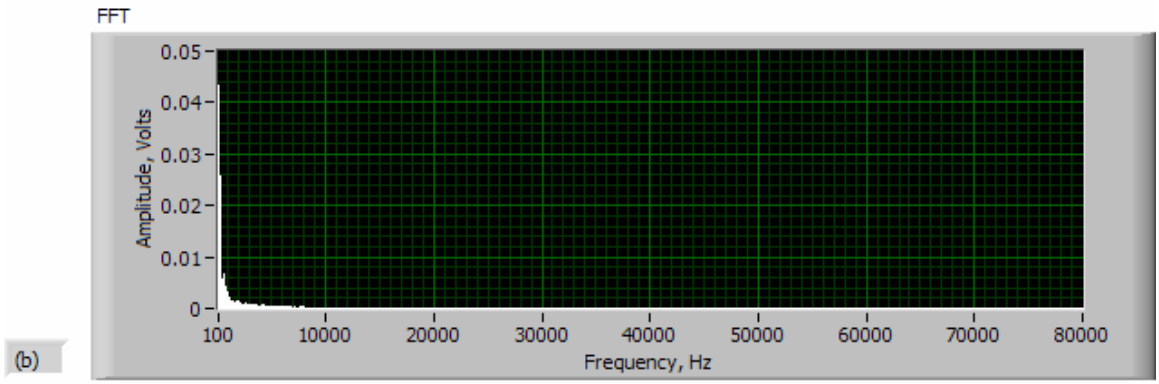
FFT
0.05
0.04
0.03
0.02
0.01
0
Amplitude, Volts
100
10000
20000
30000
40000
50000
60000
70000
80000
Frequency, Hz

(b)

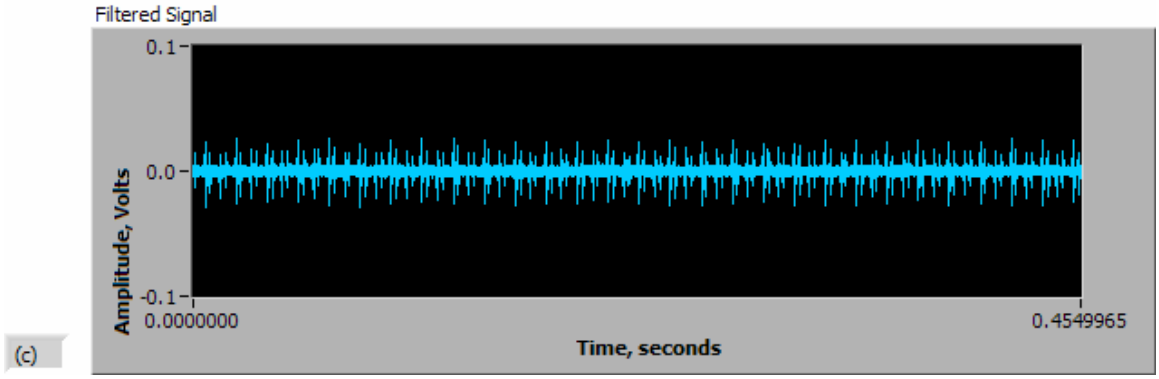
Filtered Signal
0.1
0.0
-0.1
Amplitude, Volts
0.0000000
0.4549965
Time, seconds

(c)

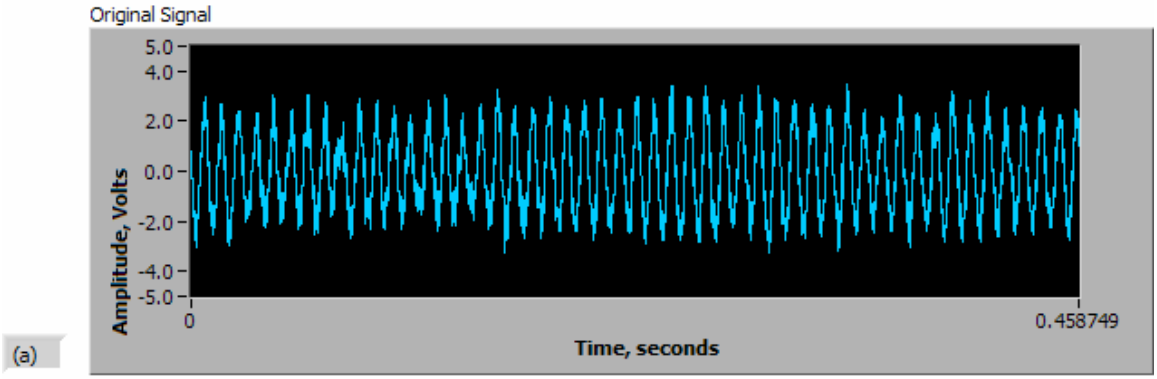
Original Signal
5.0
4.0
2.0
0.0
-2.0
-4.0
-5.0
Amplitude, Volts
0
0.458749
Time, seconds

(a)

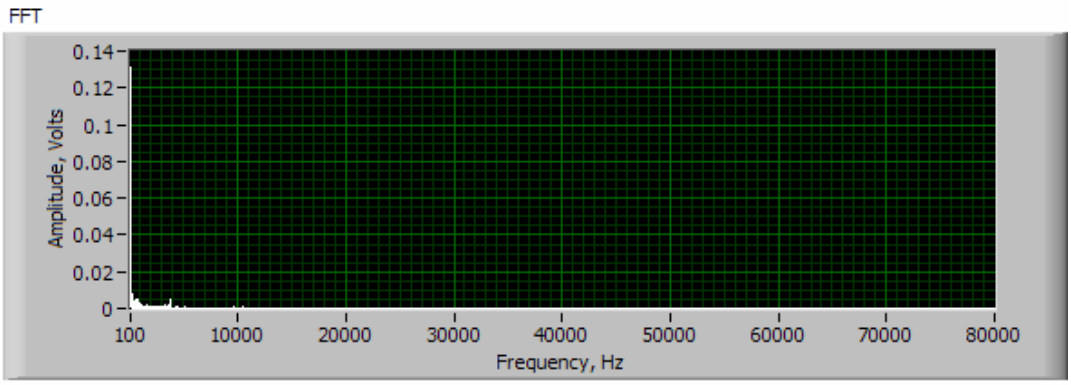
FFT
0.14
0.12
0.1
0.08
0.06
0.04
0.02
0
Amplitude, Volts
100
10000
20000
30000
40000
50000
60000
70000
80000
Frequency, Hz

(b)

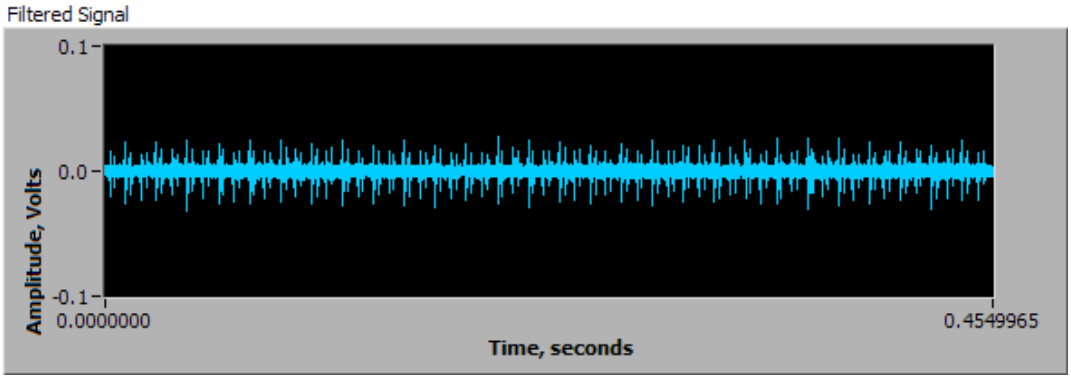
Filtered Signal
0.1
0.0
-0.1
Amplitude, Volts
0.0000000
0.4549965
Time, seconds

(c)

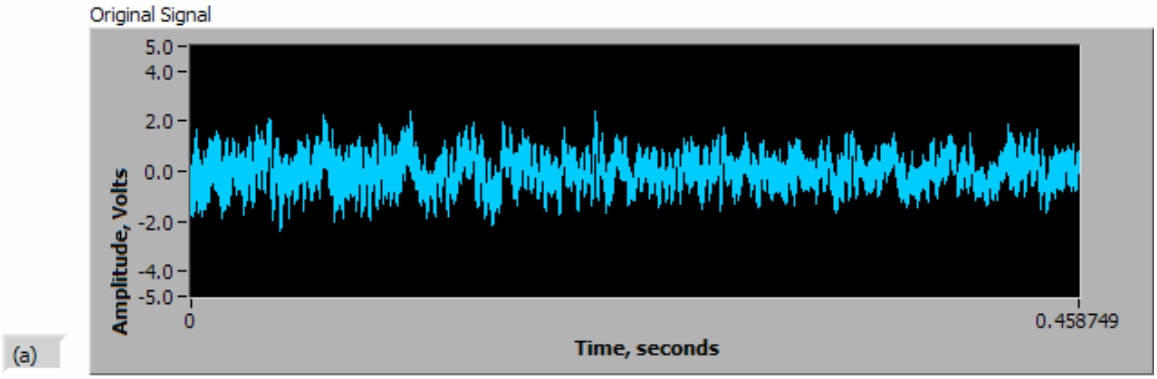
Original Signal
5.0
4.0
2.0
0.0
-2.0
-4.0
-5.0
Amplitude, Volts
0
0.458749
Time, seconds

(a)

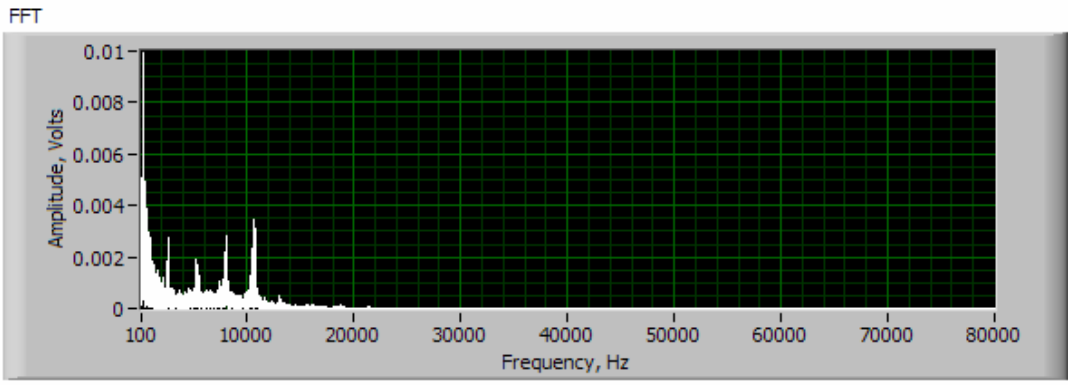
FFT
0.01
0.008
0.006
0.004
0.002
0
Amplitude, Volts
100
10000
20000
30000
40000
50000
60000
70000
80000
Frequency, Hz

(b)

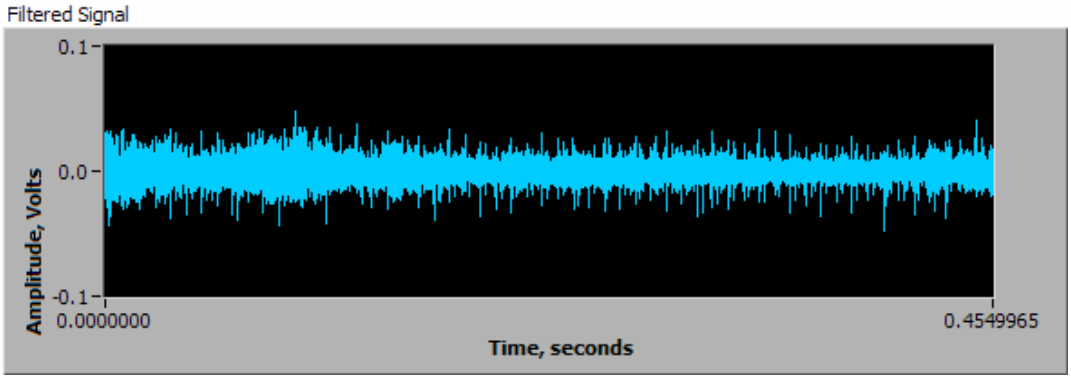
Filtered Signal
0.1
0.0
-0.1
Amplitude, Volts
0.0000000
0.4549965
Time, seconds

(c)

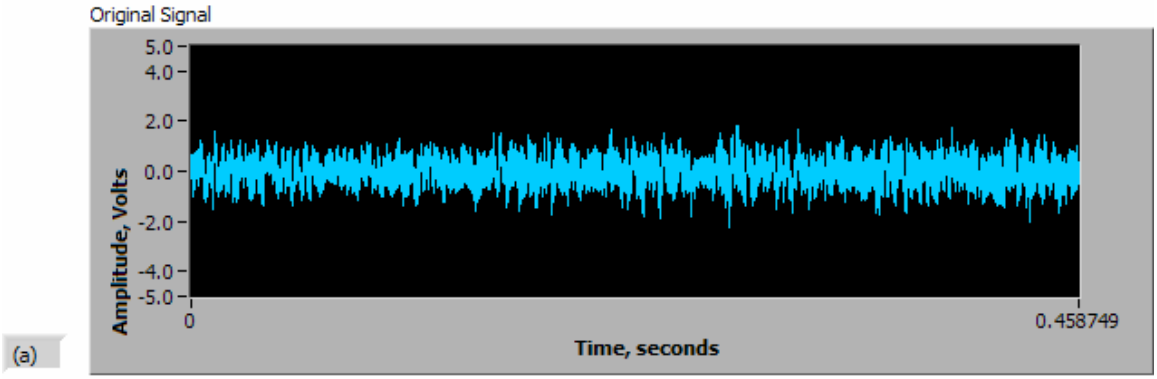
Original Signal
5.0
4.0
2.0
0.0
-2.0
-4.0
-5.0
Amplitude, Volts
0
0.458749
Time, seconds

(a)

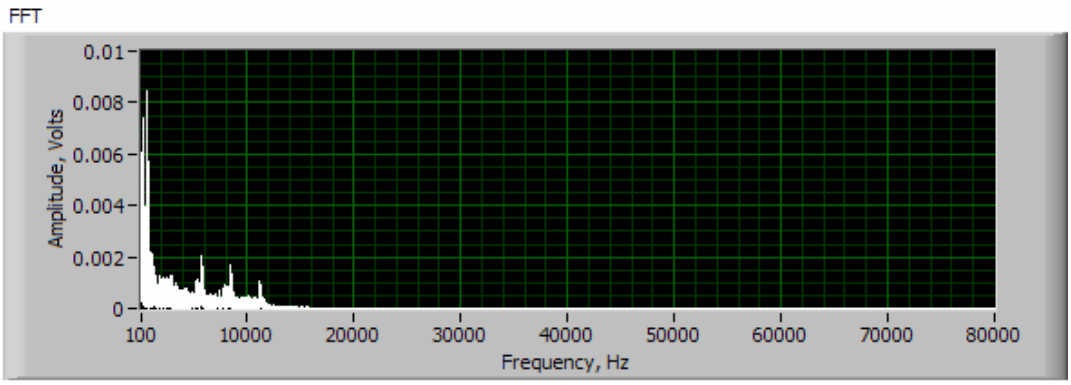
FFT
0.01
0.008
0.006
0.004
0.002
0
Amplitude, Volts
100
10000
20000
30000
40000
50000
60000
70000
80000
Frequency, Hz

(b)

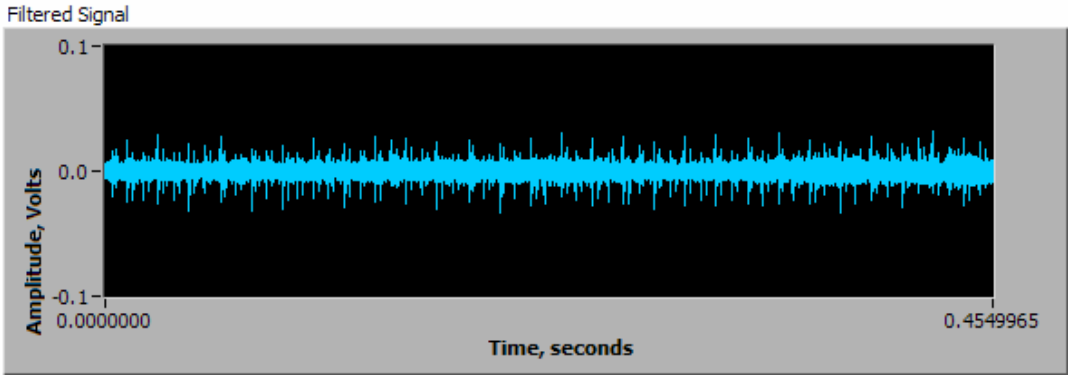
Filtered Signal
0.1
0.0
-0.1
Amplitude, Volts
0.0000000
0.4549965
Time, seconds

(c)

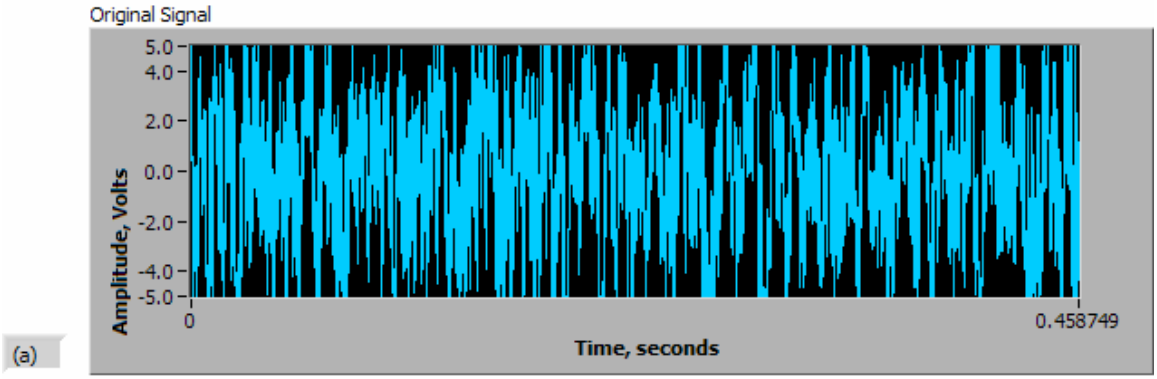
Original Signal
5.0
4.0
2.0
0.0
-2.0
-4.0
-5.0
Amplitude, Volts
0
0.458749
Time, seconds

(a)

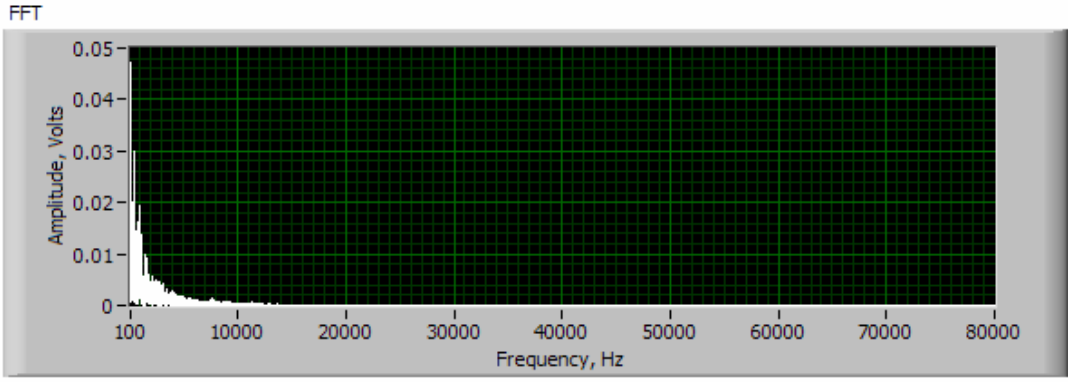
FFT
0.05
0.04
0.03
0.02
0.01
0
Amplitude, Volts
100
10000
20000
30000
40000
50000
60000
70000
80000
Frequency, Hz

(b)

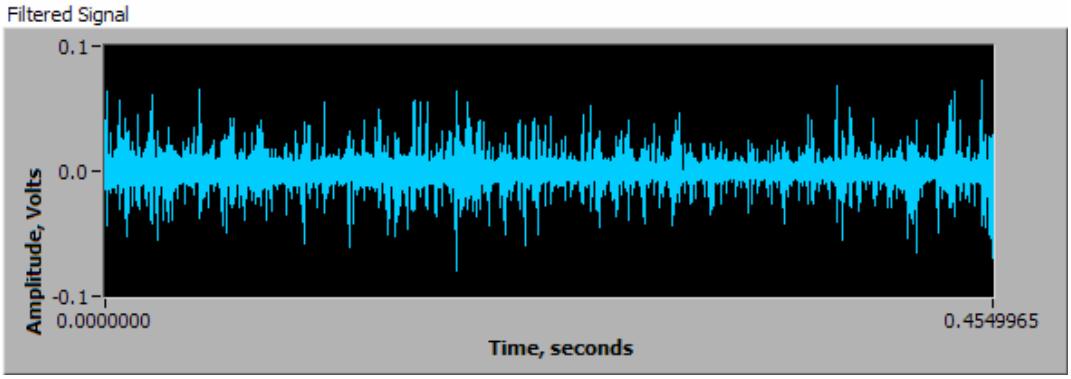
Filtered Signal
0.1
0.0
-0.1
Amplitude, Volts
0.0000000
0.4549965
Time, seconds

(c)

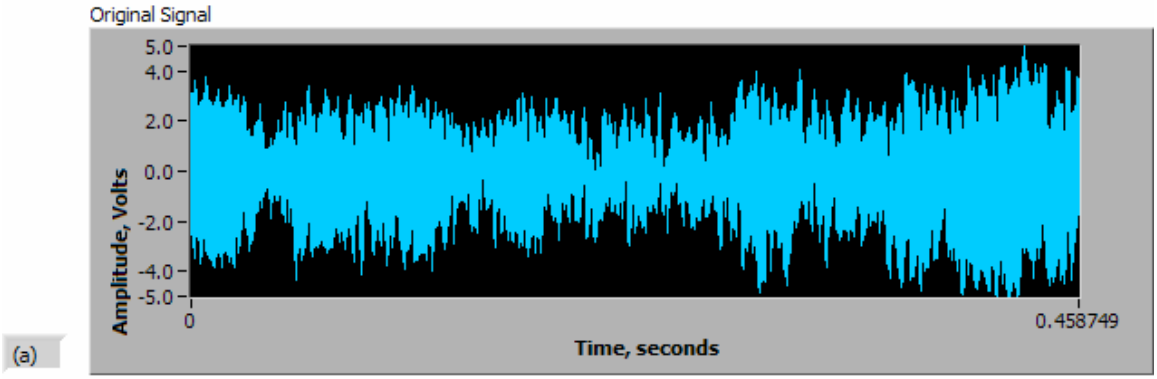
Original Signal
5.0
4.0
2.0
0.0
-2.0
-4.0
-5.0
Amplitude, Volts
0
0.458749
Time, seconds

(a)

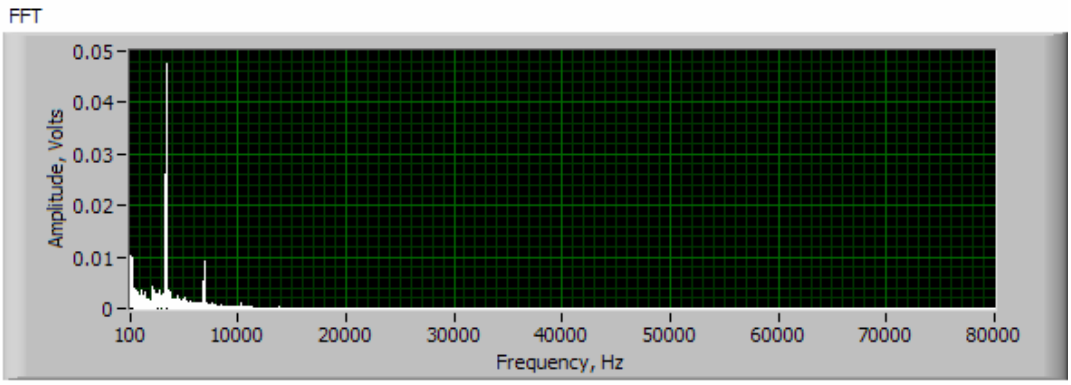
FFT
0.05
0.04
0.03
0.02
0.01
0
Amplitude, Volts
100
10000
20000
30000
40000
50000
60000
70000
80000
Frequency, Hz

(b)

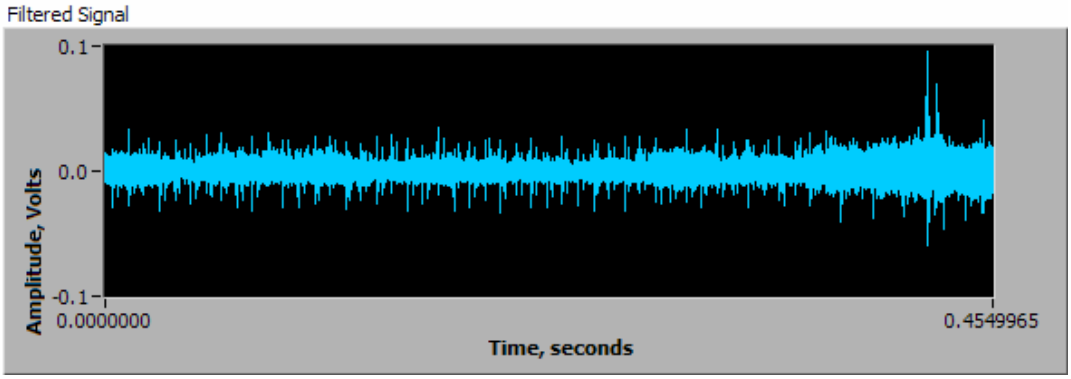
Filtered Signal
0.1
0.0
-0.1
Amplitude, Volts
0.0000000
0.4549965
Time, seconds

(c)

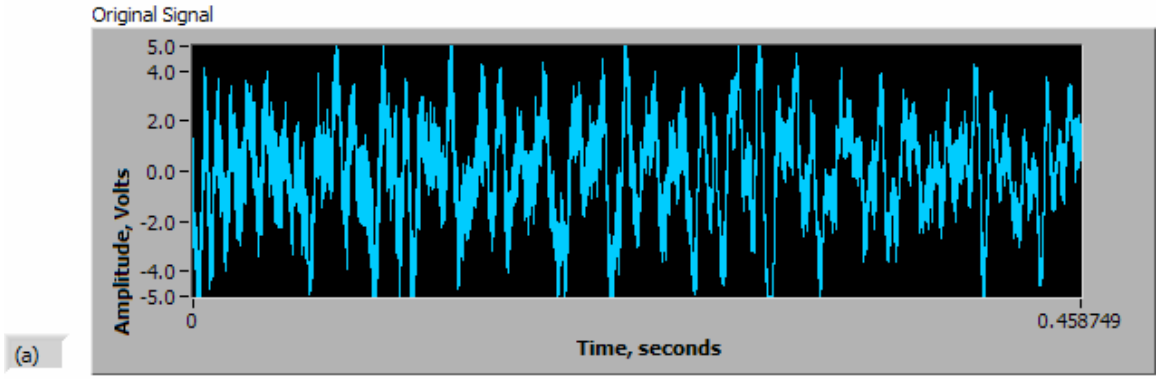
Original Signal
5.0
4.0
2.0
0.0
-2.0
-4.0
-5.0
Amplitude, Volts
0
0.458749
Time, seconds

(a)

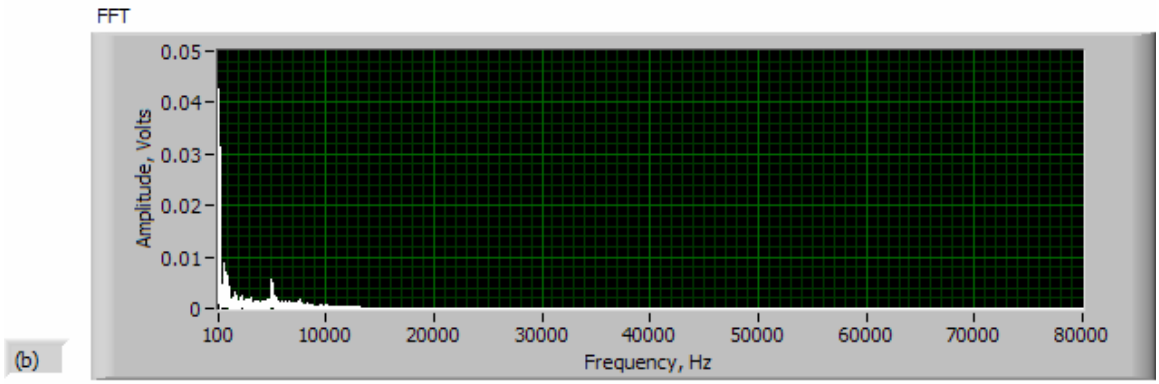
FFT
0.05
0.04
0.03
0.02
0.01
0
Amplitude, Volts
100
10000
20000
30000
40000
50000
60000
70000
80000
Frequency, Hz

(b)

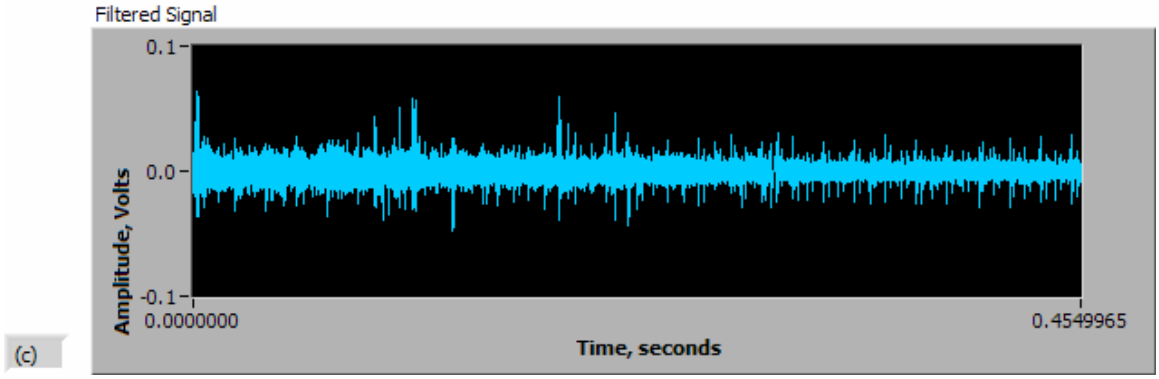
Filtered Signal
0.1
0.0
-0.1
Amplitude, Volts
0.0000000
0.4549965
Time, seconds

(c)

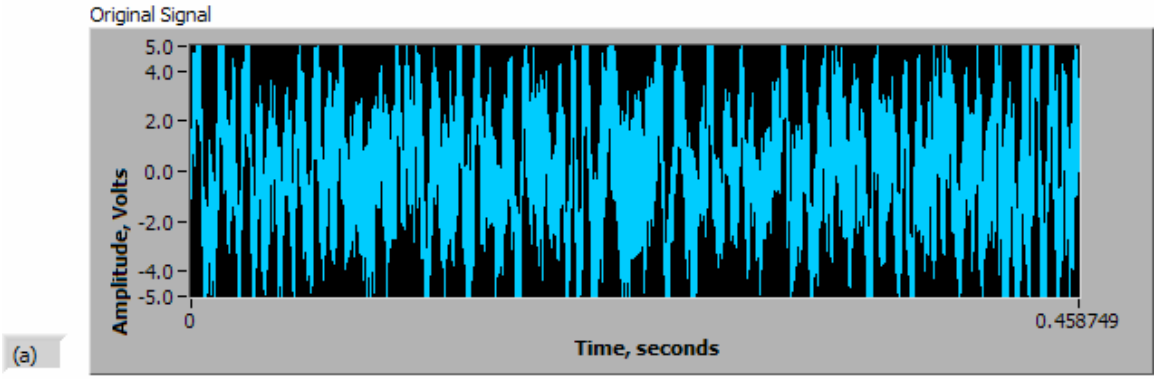
Original Signal
5.0
4.0
2.0
0.0
-2.0
-4.0
-5.0
Amplitude, Volts
0
0.458749
Time, seconds

(a)

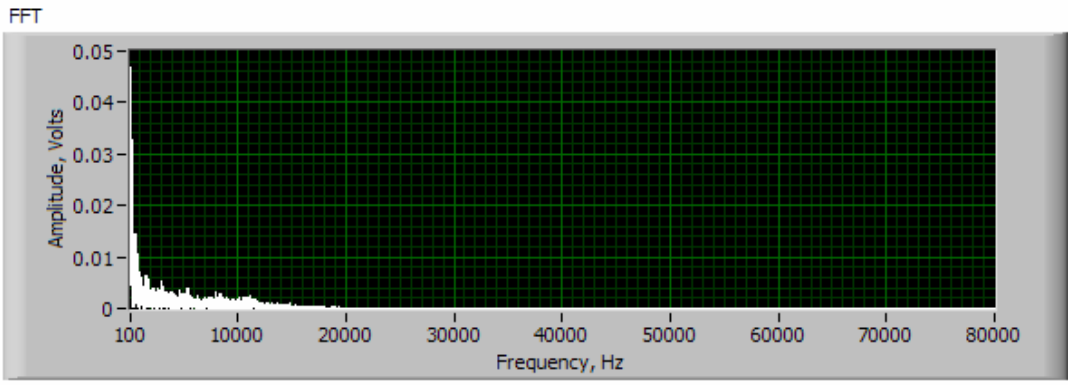
FFT
0.05
0.04
0.03
0.02
0.01
0
Amplitude, Volts
100
10000
20000
30000
40000
50000
60000
70000
80000
Frequency, Hz

(b)

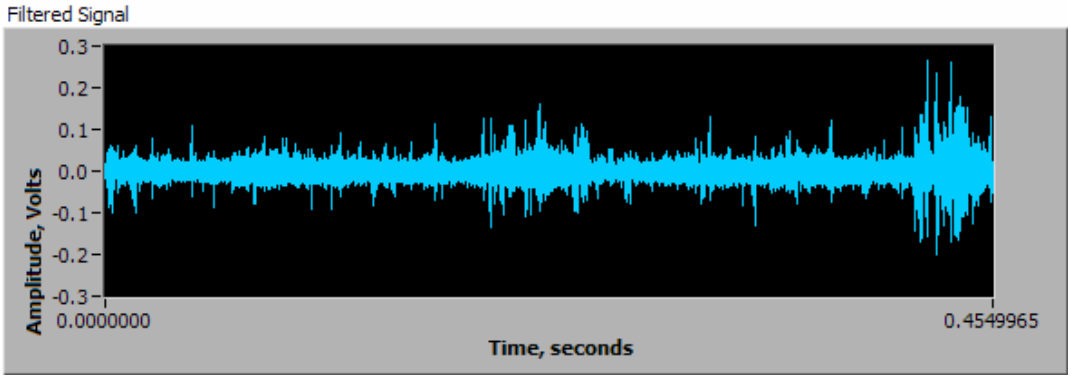
Filtered Signal
0.3
0.2
0.1
0.0
-0.1
-0.2
-0.3
Amplitude, Volts
0.0000000
0.4549965
Time, seconds

(c)

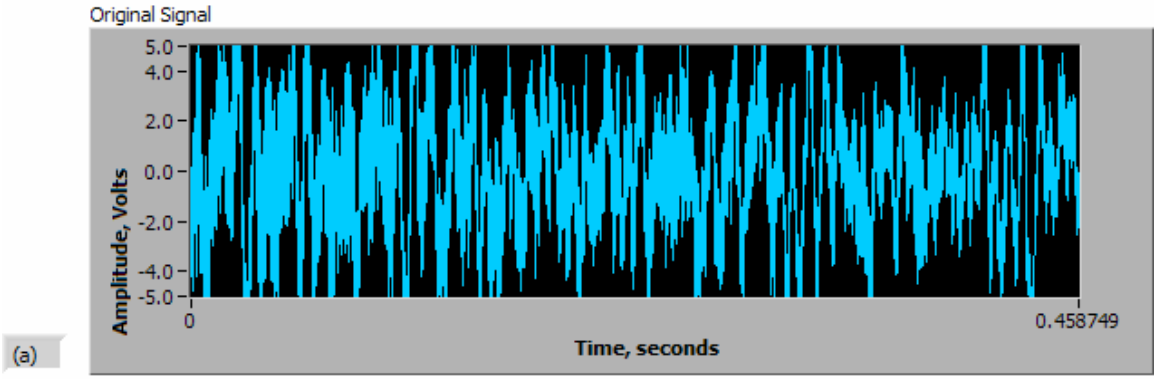
Original Signal
5.0
4.0
2.0
0.0
-2.0
-4.0
-5.0
Amplitude, Volts
0
0.458749
Time, seconds

(a)

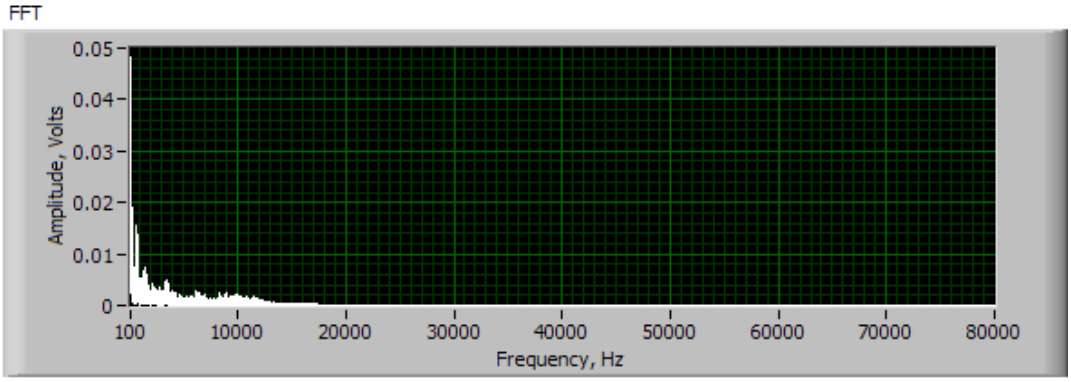
FFT
0.05
0.04
0.03
0.02
0.01
0
Amplitude, Volts
100
10000
20000
30000
40000
50000
60000
70000
80000
Frequency, Hz

(b)

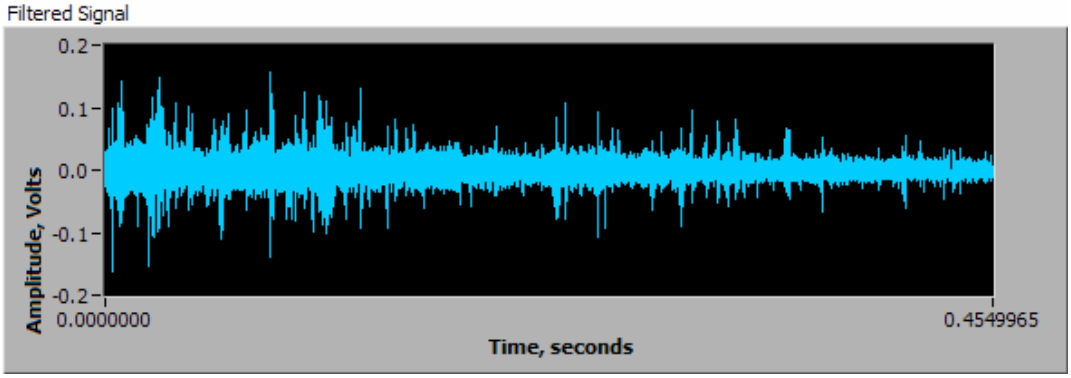
Filtered Signal
0.2
0.1
0.0
-0.1
-0.2
Amplitude, Volts
0.0000000
0.4549965
Time, seconds

(c)

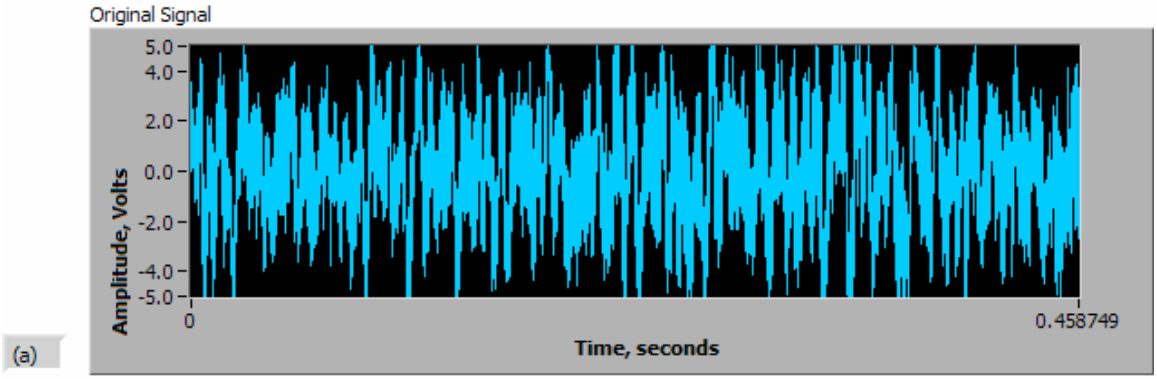
Original Signal
5.0
4.0
2.0
0.0
-2.0
-4.0
-5.0
Amplitude, Volts
0
0.458749
Time, seconds

(a)

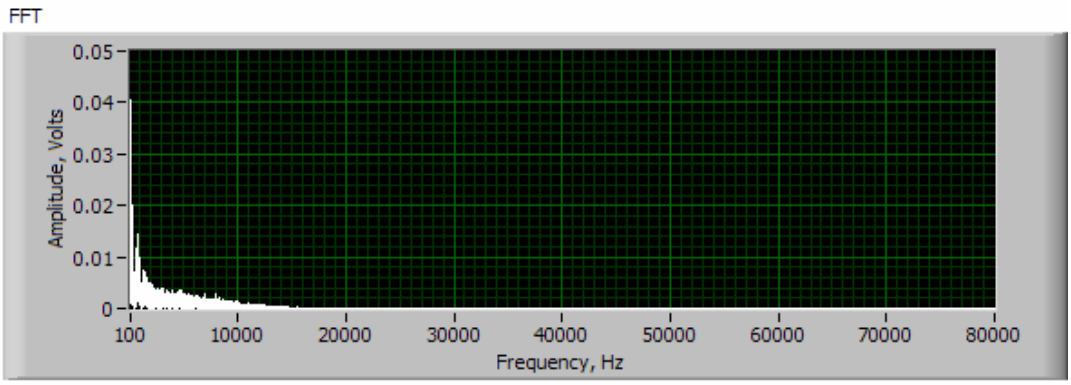
FFT
0.05
0.04
0.03
0.02
0.01
0
Amplitude, Volts
100
10000
20000
30000
40000
50000
60000
70000
80000
Frequency, Hz

(b)

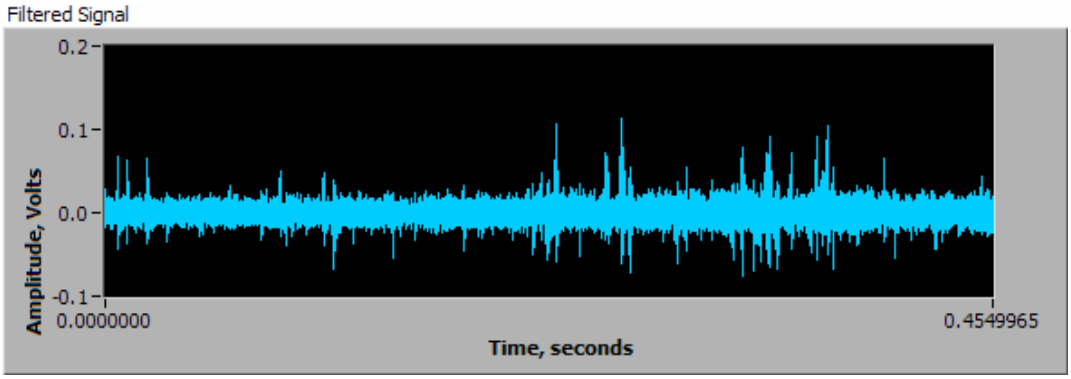
Filtered Signal
0.2
0.1
0.0
-0.1
Amplitude, Volts
0.0000000
0.4549965
Time, seconds

(c)

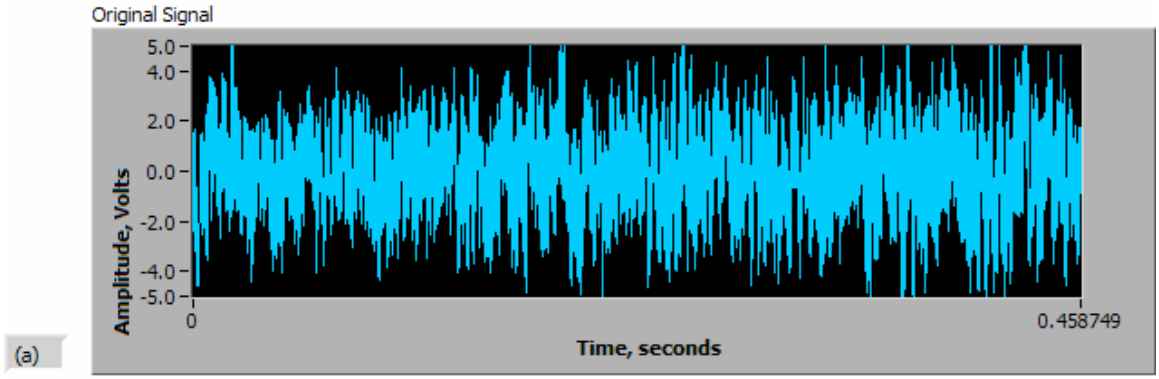
Original Signal
5.0
4.0
2.0
0.0
-2.0
-4.0
-5.0
Amplitude, Volts
0
0.458749
Time, seconds

(a)

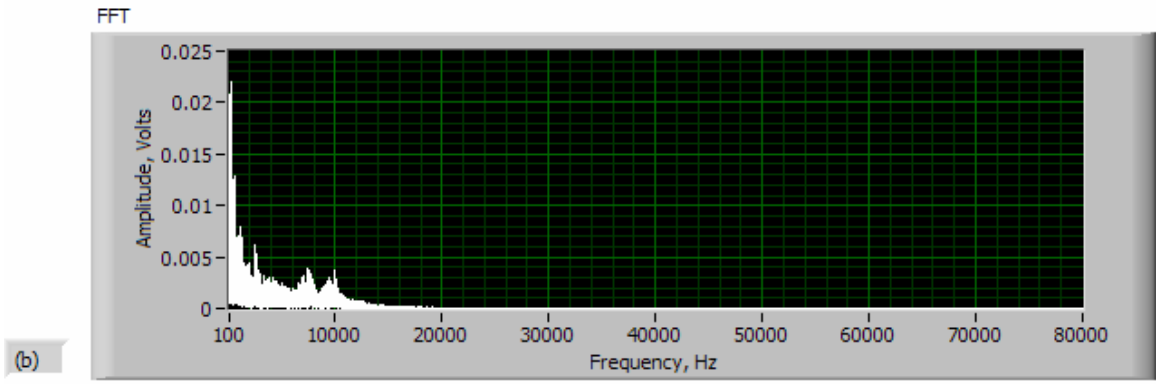
FFT
0.025
0.02
0.015
0.01
0.005
0
Amplitude, Volts
100
10000
20000
30000
40000
50000
60000
70000
80000
Frequency, Hz

(b)

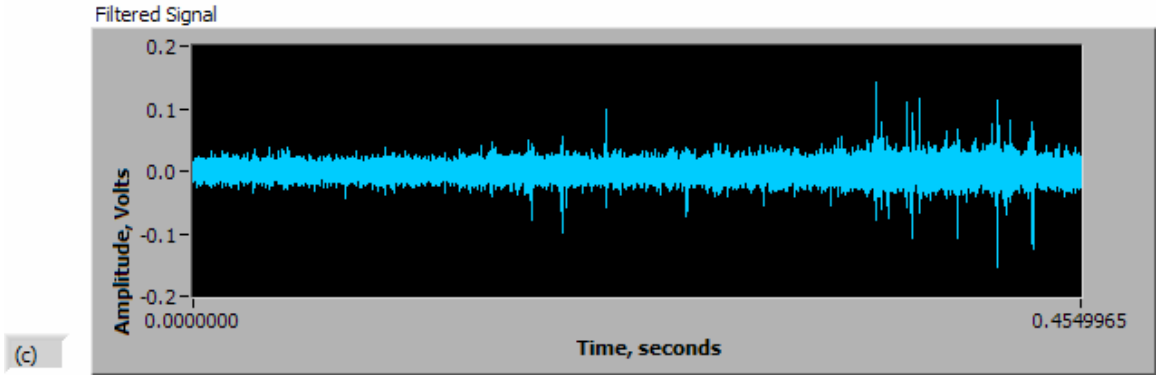
Filtered Signal
0.2
0.1
0.0
-0.1
-0.2
Amplitude, Volts
0.0000000
0.4549965
Time, seconds

(c)

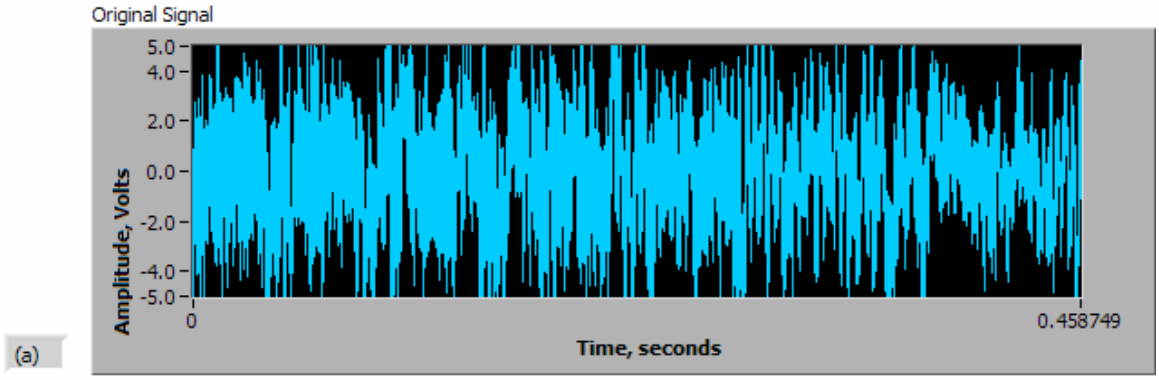
Original Signal
5.0
4.0
2.0
0.0
-2.0
-4.0
-5.0
Amplitude, Volts
0
0.458749
Time, seconds

(a)

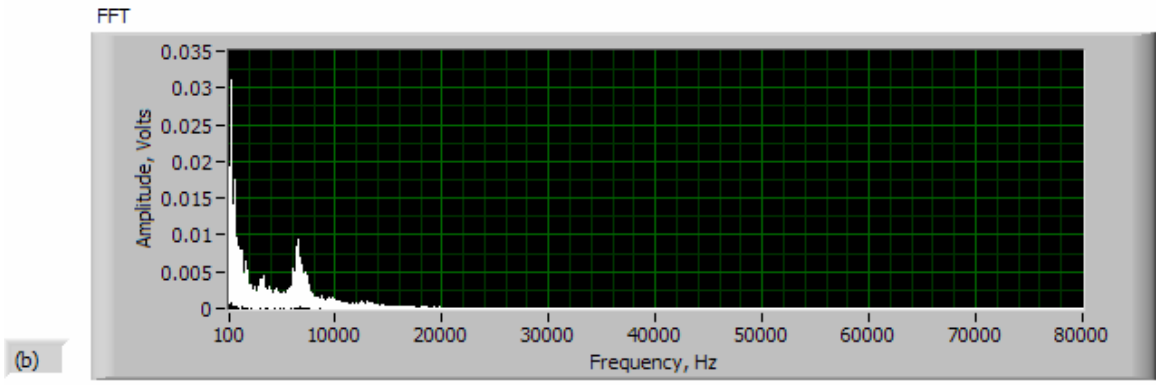
FFT
0.035
0.03
0.025
0.02
0.015
0.01
0.005
0
Amplitude, Volts
100
10000
20000
30000
40000
50000
60000
70000
80000
Frequency, Hz

(b)

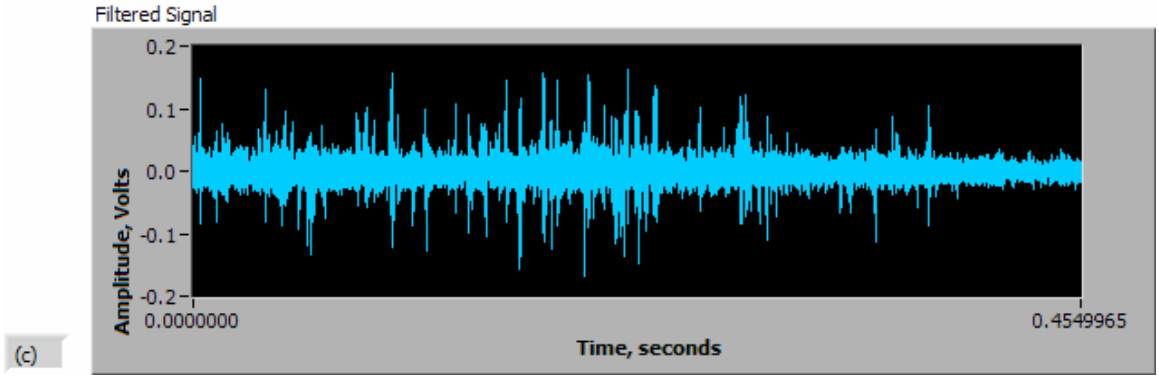
Filtered Signal
0.2
0.1
0.0
-0.1
-0.2
Amplitude, Volts
0.0000000
0.4549965
Time, seconds

(c)

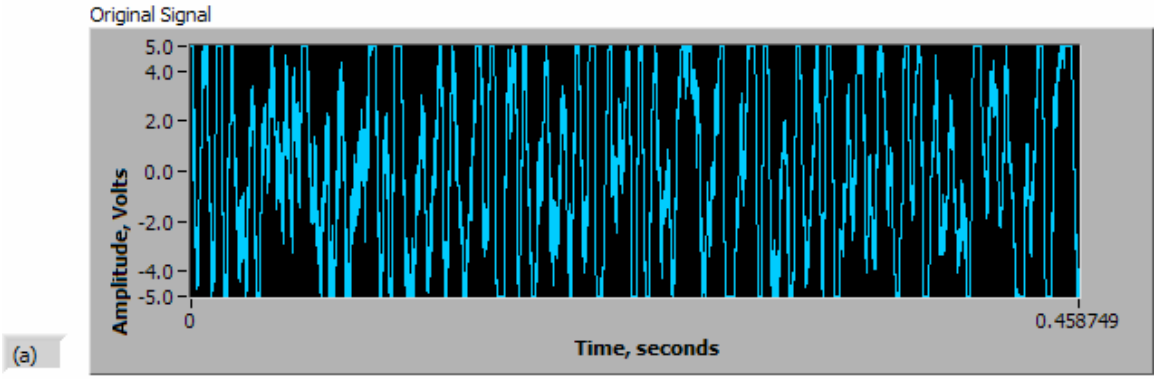
Original Signal
5.0
4.0
2.0
0.0
-2.0
-4.0
-5.0
Amplitude, Volts
0
0.458749
Time, seconds

(a)

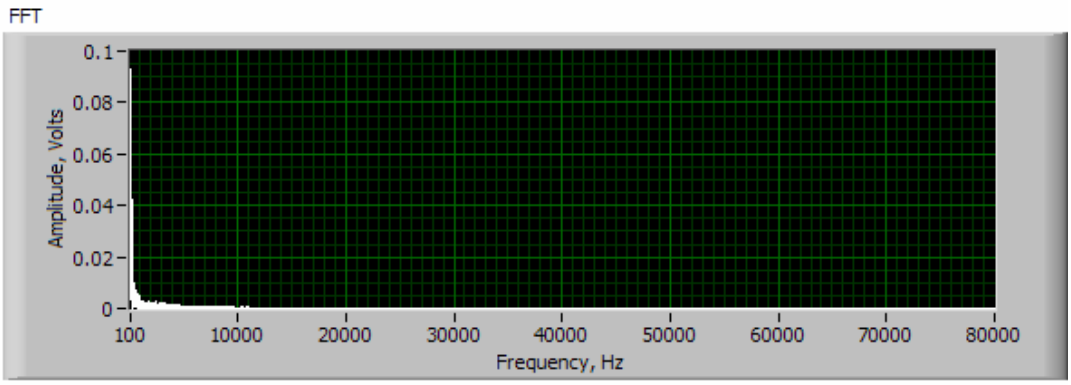
FFT
0.1
0.08
0.06
0.04
0.02
0
Amplitude, Volts
100
10000
20000
30000
40000
50000
60000
70000
80000
Frequency, Hz

(b)

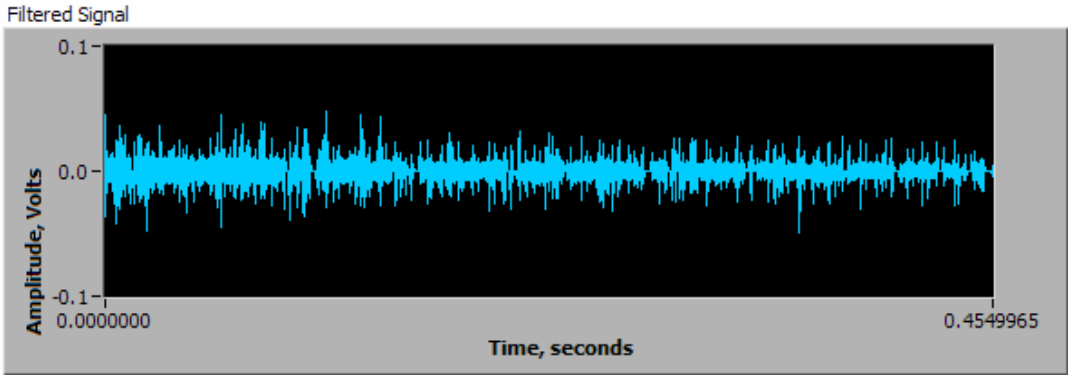
Filtered Signal
0.1
0.0
-0.1
Amplitude, Volts
0.0000000
0.4549965
Time, seconds

(c)

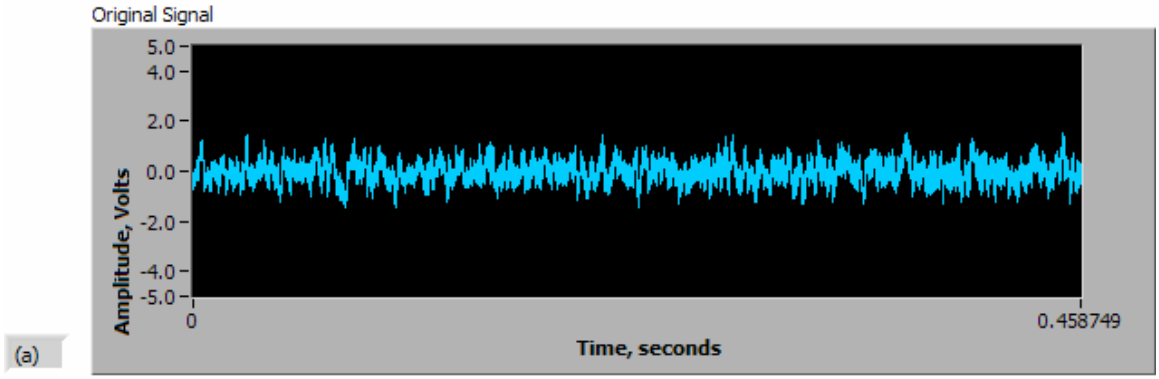
Original Signal
5.0
4.0
2.0
0.0
-2.0
-4.0
-5.0
Amplitude, Volts
0
0.458749
Time, seconds

(a)

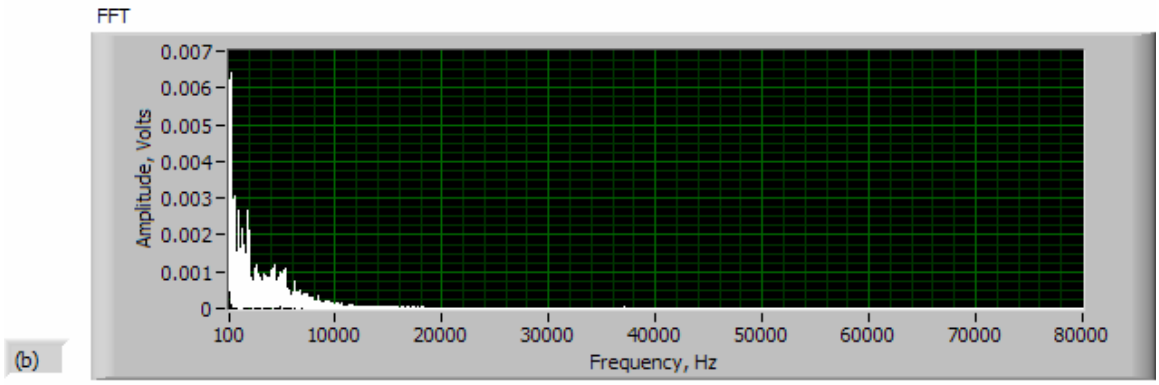
FFT
0.007
0.006
0.005
0.004
0.003
0.002
0.001
0
Amplitude, Volts
100
10000
20000
30000
40000
50000
60000
70000
80000
Frequency, Hz

(b)

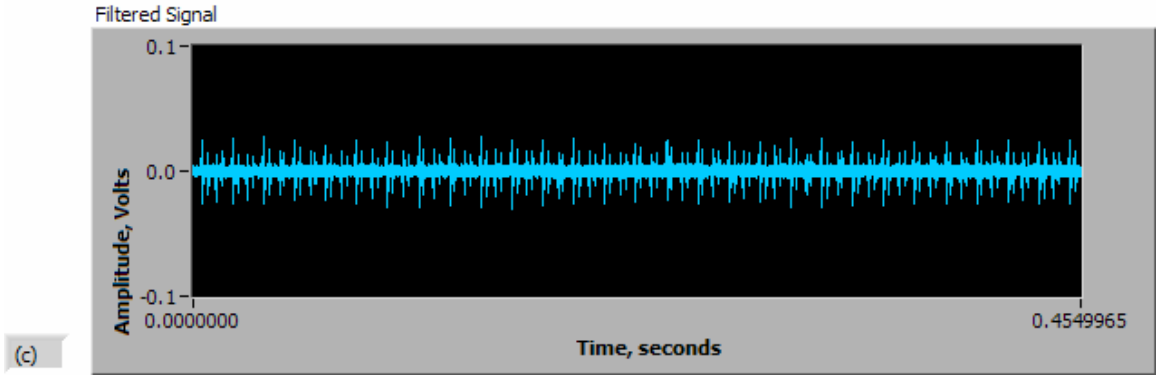
Filtered Signal
0.1
0.0
-0.1
Amplitude, Volts
0.0000000
0.4549965
Time, seconds

(c)

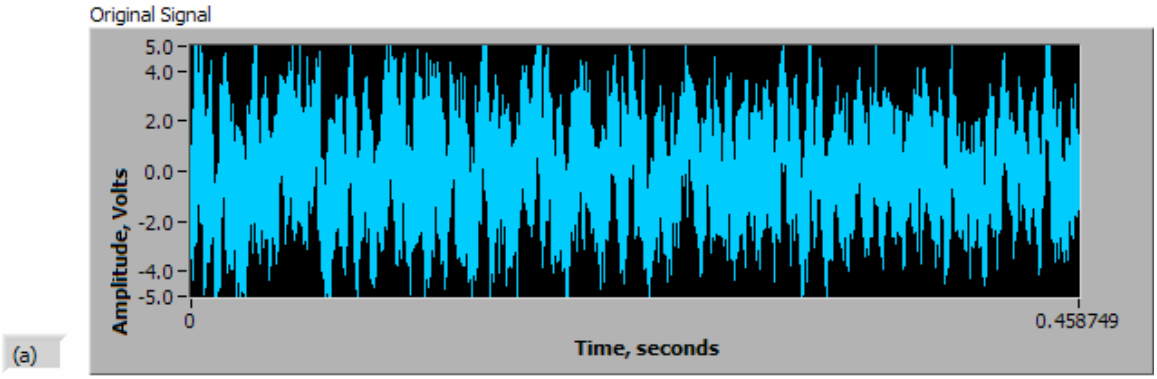
Original Signal
5.0
4.0
2.0
0.0
-2.0
-4.0
-5.0
Amplitude, Volts
0
0.458749
Time, seconds

(a)

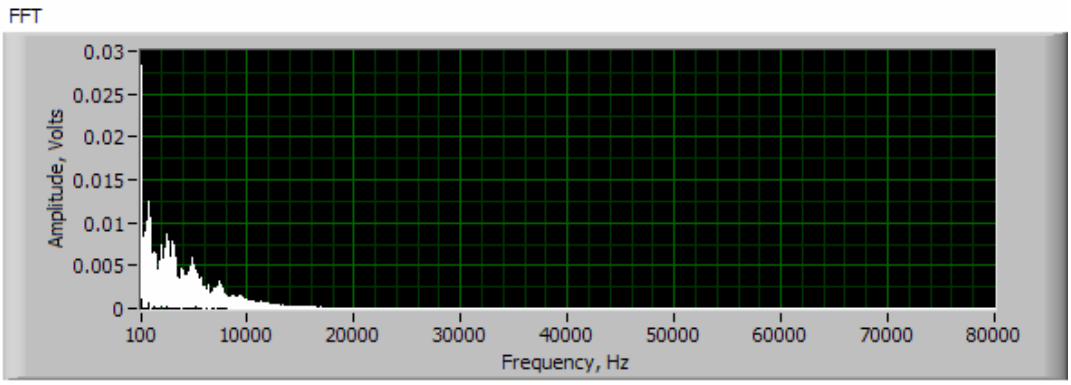
FFT
0.03
0.025
0.02
0.015
0.01
0.005
0
Amplitude, Volts
100
10000
20000
30000
40000
50000
60000
70000
80000
Frequency, Hz

(b)

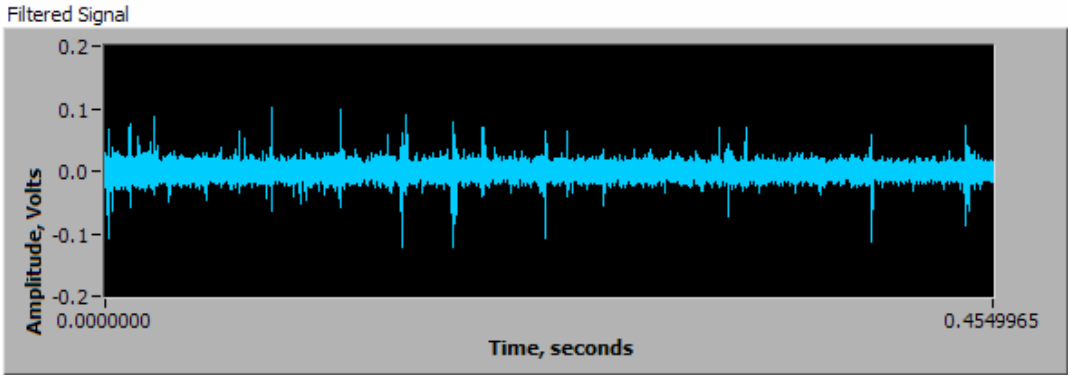
Filtered Signal
0.2
0.1
0.0
-0.1
-0.2
Amplitude, Volts
0.0000000
0.4549965
Time, seconds

(c)

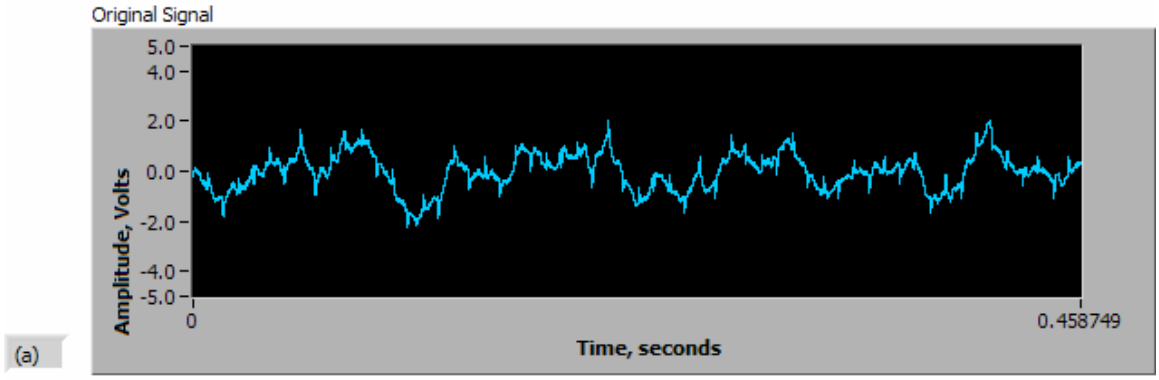
Original Signal
5.0
4.0
2.0
0.0
-2.0
-4.0
-5.0
Amplitude, Volts
0
0.458749
Time, seconds

(a)

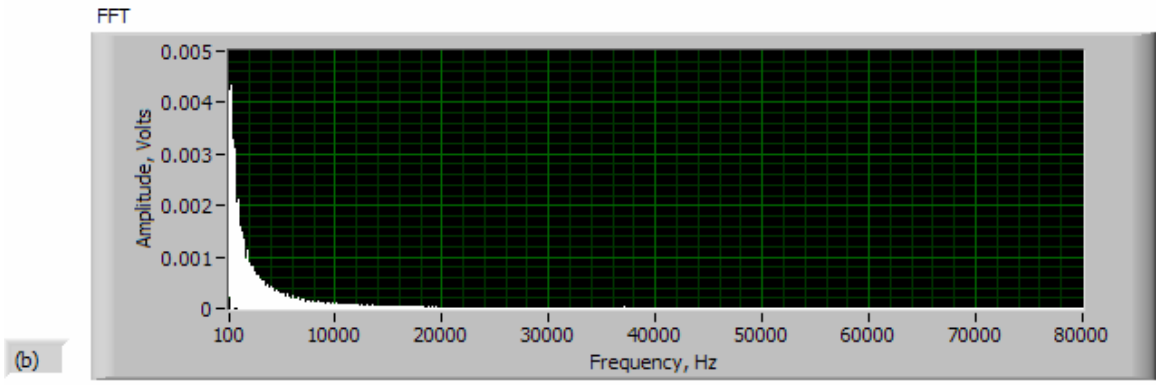
FFT
0.005
0.004
0.003
0.002
0.001
0
Amplitude, Volts
100
10000
20000
30000
40000
50000
60000
70000
80000
Frequency, Hz

(b)

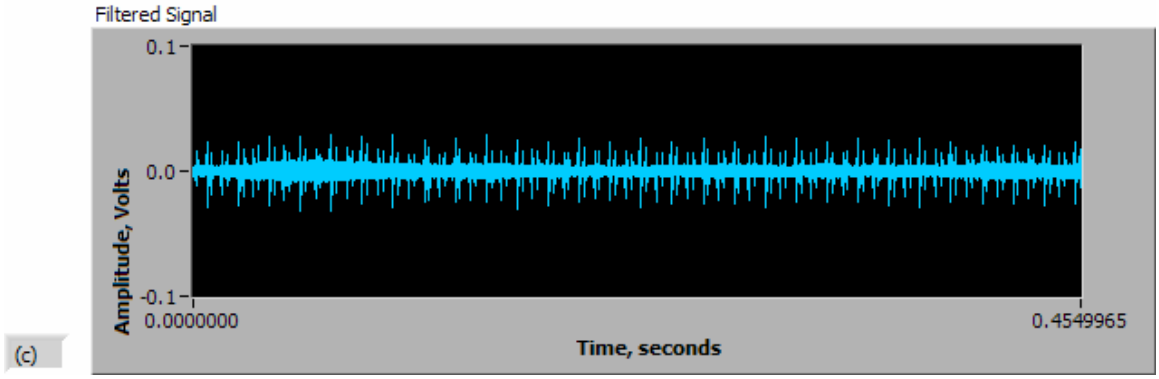
Filtered Signal
0.1
0.0
-0.1
Amplitude, Volts
0.0000000
0.4549965
Time, seconds

(c)